Humboldt-Universität zu Berlin
Mathematisch-Naturwissenschaftliche Fakultät I

Bethe-Salpeter equation formalism beyond the Tamm-Dancoff approximation and zero momentum transfer

Masterarbeit zur Erlangung des akademischen Grades Master of Science (M. Sc.) im Fach Physik

Benjamin Aurich, B.Sc.

10. September 2017

Gutachter:
Prof. Claudia Draxl
Prof. Kurt Busch

Abstract

The Bethe-Salpeter equation formalism implemented in the full-potential all-electron computer package `exciting` was extended in two ways: On the one hand, the support for non-zero momentum transfer to the exciton was introduced, allowing for a description of excitonic effects in the electron energy loss spectrum and the investigation of exciton band structures. On the other hand, the possibility to go beyond the commonly used Tamm-Dancoff approximation and to include the coupling between resonant and anti-resonant transitions was added, significantly improving spectra with plasmonic contributions.

Contents

List of Figures

List of Tables

1. Introduction

The design of application-oriented novel materials relies fundamentally on the understanding of the elementary excitations that govern the investigated property. For example, the absorption of visible light in a semiconductor is heavily influenced by the formation of so-called excitons which are collective excitations involving the creation of electron-hole (e-h) pairs. The first models for these excitations in the limit of strongly and weakly bound e-h pairs were given in the nineteen-thirties by Frenkel and Wannier [1, 2]. Since then, advances in many-body perturbation theory (MBPT) and its application to solid state physics have allowed for systematic improvements in the description of elementary excitations [3]. Now, the state-of-the-art method for describing the optical properties of a semiconductor uses the so-called Bethe-Salpeter equation (BSE). It describes excitations consisting of interacting e-h pairs and is typically solved to yield the polarizability of the material. The same polarizability can also be used to describe the results of electron energy loss spectroscopy (EELS) and inelastic x-ray scattering (IXS) experiments. The BSE is usually solved by reformulating it as an eigenvalue problem (EVP) of an associated BSE Hamiltonian in a basis of transition states which describe the considered independent e-h pairs [4].

For visible light it is argued that the momentum transfer Q from photon to electron is negligible, and consequently only direct transition states are used in the BSE Hamiltonian. Additionally, the coupling between resonant and anti-resonant transitions, i.e. excitations and de-excitations, is often neglected with the use of the so-called Tamm-Dancoff approximation (TDA). Using the TDA halves the Hamiltonian matrix size and makes it hermitian which significantly simplifies the numerical computation. In the case of optical absorption, this approach has yielded excellent agreement with experiments [5]. However, the TDA fails to predict the EEL spectrum of silicon at vanishing momentum transfer [6] and was reported to break down even for the optical absorption spectrum of confined organic molecular systems [7].

The BSE formalism can be used equally well for a non-vanishing momentum transfer by considering only transition states of the same Q [8]. The solutions of the q-dependent BSE can then be used to interpret IXS or EELS experiments with the inclusion of excitonic effects or to study the dynamics of excitons which are important, for example, in the description of the energy transport in photovoltaics. In the q-dependent calculations the use of the TDA has been reported to yield differing results even for the imaginary part of the dielectric function of silicon [9].

From the considerations above, it is clear that for a thorough investigation of complex novel materials within the framework of the BSE it needs to be possible to go beyond the TDA and to use finite momentum transfers. The addition of these two functionalities to the `exciting` code [10] and their application to prototypical systems is the concern of the present work.

The work is structured as follows: First, in chapter 2 the connection between the classical dielectric theory and the ground state expectation value of the quantum mechanical density fluctuation operator is made. In chapter 3 the main ideas of density-functional theory (DFT) and MBPT are outlined and the connection between the density fluctuation and the BSE is highlighted. Subsequently, in chapter 4 the mapping of the BSE to a EVP and its solution following [9] are described. The implementation in `exciting` is outlined in chapter 5. The results of the exemplary calculations for silicon, lithium fluoride as well as for the three crystalline organic semiconductors formed from naphthalene (2A), biphenyl (2P) and bithiophene (2T) are discussed in chapter 6.

2. Microscopic dielectric theory

In this chapter we revisit the classical dielectric response of a material and outline it's connection to a quantum mechanical expectation value of the so-called density-fluctuation operator. The evaluation of this expectation value is the main goal of the Bethe-Salpeter equation formalism discussed in section 3.3.4 and chapter 4.

In section 2.1 we first recapitulate Maxwell's equations within a medium and discuss the so-called material equations. The material equations constitute linear response functions which link external and induced quantities of Maxwell's theory. The microscopic dielectric tensor ε is introduced in section 2.2 as the main material equation of interest, and the longitudinal and transversal response formalism is discussed. In section 2.3 we then demonstrate how ε can be computed quantum mechanically using first-order time-dependent perturbation theory. In section 2.4 the connection to the dynamical structure factor and to the optical absorption spectrum is given. Lastly, in section 2.5 the case of a crystalline system is discussed. In this chapter we mainly follow the notation of [11] and keep the notation in SI-units.

2.1. Microscopic Maxwell equations

When considering the interaction of a solid with an external electromagnetic field, the Maxwell equations are commonly written in terms of external and induced quantities. For example, the total charge density in the material can be split into the charge density of the unperturbed system ρ^0, an externally introduced charge density ρ^{ext}, and an induced charge density ρ^{ind} that describes the change of ρ^0 due to ρ^{ext}:

$$\rho^{\text{total}} = \rho^{\text{ext}} + \rho^{\text{ind}} + \rho^0. \tag{2.1}$$

By doing the same for the current and the fields, the Maxwell equations can be solved excluding the unperturbed quantities. Then,

$$\rho = \rho^{\text{ext}} + \rho^{\text{ind}} \tag{2.2}$$

denotes the charge density difference with respect to the unperturbed system. In the following we use the same notation for the current and fields. The induced charge density ρ^{ind} and the induced current $\boldsymbol{j}^{\text{ind}}$ are usually described in terms of the *polarization field* $\boldsymbol{P}$ and the *magnetization field* $\boldsymbol{M}$, according to

$$\rho^{\text{ind}} = \nabla \cdot \boldsymbol{P} \quad \text{and} \quad \boldsymbol{j}^{\text{ind}} = \frac{\partial \boldsymbol{P}}{\partial t} + \nabla \times \boldsymbol{M}. \tag{2.3}$$

The fields $\boldsymbol{P}$ and $\boldsymbol{M}$ are not uniquely defined, since $\tilde{\boldsymbol{P}} = \boldsymbol{P} - \nabla \times L$ and $\tilde{\boldsymbol{M}} = \boldsymbol{M} + \frac{\partial L}{\partial t}$ yield the same density and current for any function L. By setting $\boldsymbol{M} = \frac{1}{\mu_0}\boldsymbol{B}^{\text{ind}}$ and $\boldsymbol{P} = -\varepsilon_0 \boldsymbol{E}^{\text{ind}}$ Maxwell's equations neatly separate into induced and external fields:

$$\nabla \cdot \boldsymbol{B} = 0 \qquad \nabla \times \boldsymbol{E} + \partial_t \boldsymbol{B} = 0 \tag{2.4a}$$

$$\nabla \times \boldsymbol{B}^{\text{ext}} - c_0^{-2}\partial_t \boldsymbol{E}^{\text{ext}} = \mu_0 \boldsymbol{j}^{\text{ext}} \qquad \nabla \cdot \boldsymbol{E}^{\text{ext}} = \varepsilon_0^{-1}\rho^{\text{ext}} \tag{2.4b}$$

$$\nabla \times \boldsymbol{B}^{\text{ind}} - c_0^{-2}\partial_t \boldsymbol{E}^{\text{ind}} = \mu_0 \boldsymbol{j}^{\text{ind}} \qquad \nabla \cdot \boldsymbol{E}^{\text{ind}} = -\varepsilon_0^{-1}\rho^{\text{ind}}. \tag{2.4c}$$

The fields can also be expressed in terms of the electrostatic scalar potential φ and the magnetic vector potential $\boldsymbol{A}$ as

$$\boldsymbol{E}(\boldsymbol{r}, t) = -\nabla \cdot \varphi(\boldsymbol{r}, t) - \partial_t \boldsymbol{A}(\boldsymbol{r}, t) \quad \text{and} \quad \boldsymbol{B}(\boldsymbol{r}, t) = \nabla \times \boldsymbol{A}(\boldsymbol{r}, t). \tag{2.5}$$

Additionally to the set of equations (2.4), a *material equation* is needed to connect the induced quantities to the external ones. For a sufficiently small perturbation they are given by *linear response functions* of the form

$$F_\alpha^{\text{ind}}(\boldsymbol{r}, t) = \sum_\beta \iint R^{\alpha\beta}(\boldsymbol{r}, \boldsymbol{r}', t - t') F_\beta^{\text{ext}}(\boldsymbol{r}', t')\, \mathrm{d}^3 r'\, \mathrm{d}t', \quad \text{symbolically} \quad \boldsymbol{F}^{\text{ind}} = R\boldsymbol{F}^{\text{ext}}, \tag{2.6}$$

where R is non-zero only for $t > t'$ to ensure causality [12]. One example of such a response function is the electrical *susceptibility* χ that relates the induced current to the external electric field

$$\partial_t \boldsymbol{j}^{\text{ind}} = \chi \boldsymbol{E}^{\text{ext}}. \tag{2.7}$$

2.2. Microscopic dielectric tensor

The concept of the response functions can be generalized to also include relations between the total fields to the external ones. In particular, we are interested in the *microscopic dielectric tensor* ε^{-1} that relates the external electric field $\boldsymbol{E}^{\text{ext}}$ to the total perturbing electric field $\boldsymbol{E}$. It is the key quantity in describing the response of a system to incoming light or penetrating electrons and it is defined as

$$E_i^{\text{ext}}(\boldsymbol{r}, t) = \iint \sum_j \varepsilon^{-1}{}^{ij}(\boldsymbol{r}, \boldsymbol{r}', t - t') E_j(\boldsymbol{r}', t')\, \mathrm{d}^3 r\, \mathrm{d}t', \quad \text{symbolically} \quad \boldsymbol{E}^{\text{ext}} = \varepsilon \boldsymbol{E}. \tag{2.8}$$

Decomposing the electric fields into a curl-free (longitudinal) E_{L} and a divergence-free (transversal) E_{T} component

$$\boldsymbol{E} = \boldsymbol{E}_{\text{L}} + \boldsymbol{E}_{\text{T}} \quad \text{where} \quad \nabla \cdot \boldsymbol{E}_{\text{T}} = \nabla \times \boldsymbol{E}_{\text{L}} = 0, \tag{2.9}$$

eq. (2.8) can be split into longitudinal (L) and transversal (T) subspaces as

$$\begin{pmatrix} \boldsymbol{E}_{\text{L}}^{\text{ext}} \\ \boldsymbol{E}_{\text{T}}^{\text{ext}} \end{pmatrix} = \begin{pmatrix} \varepsilon_{\text{LL}} & \varepsilon_{\text{LT}} \\ \varepsilon_{\text{TL}} & \varepsilon_{\text{TT}} \end{pmatrix} \begin{pmatrix} \boldsymbol{E}_{\text{L}} \\ \boldsymbol{E}_{\text{T}} \end{pmatrix}. \tag{2.10}$$

In the following, we assume that the external perturbation is purely longitudinal and that the resulting induced current is also purely longitudinal. Then, only the longitudinal-longitudinal response is needed to describe the dielectric properties of the system:

$$\boldsymbol{E}^{\text{ext}} = \boldsymbol{E}^{\text{ext}}_{\text{L}} \approx \varepsilon_{\text{LL}} \boldsymbol{E}_{\text{L}}. \tag{2.11}$$

Using the Coulomb-gauge ($\nabla \cdot \boldsymbol{A} = 0$), this can be equivalently formulated in terms of the *longitudinal microscopic dielectric function* that relates the external and the total perturbing scalar potential

$$\varphi_{\text{ext}}(\boldsymbol{r}, t) = \iint \varepsilon(\boldsymbol{r}, \boldsymbol{r}', t - t')\varphi(\boldsymbol{r}', t') \, \mathrm{d}^3 r' \, \mathrm{d}t' \, . \tag{2.12}$$

Under these conditions the Fourier coefficients of the tensor ε_{LL} and the function ε are related by

$$\varepsilon^{\alpha\beta}_{\text{LL}}(\boldsymbol{q}, \boldsymbol{q}', \omega) = \frac{q_\alpha \varepsilon(\boldsymbol{q}, \boldsymbol{q}', \omega) q'_\beta}{|\boldsymbol{q}'|^2}. \tag{2.13}$$

In analogy to eq. (2.12) one can introduce the *(longitudinal) susceptibility* χ

$$\rho_{\text{ind}}(\boldsymbol{r}, t) = \iint e^2 \chi(\boldsymbol{r}, \boldsymbol{r}', t - t')\varphi_{\text{ext}}(\boldsymbol{r}', t') \, \mathrm{d}^3 r' \, \mathrm{d}t' \tag{2.14}$$

and the *(longitudinal) polarizability* P

$$\rho_{\text{ind}}(\boldsymbol{r}, t) = \iint e^2 P(\boldsymbol{r}, \boldsymbol{r}', t - t')\varphi(\boldsymbol{r}', t') \, \mathrm{d}^3 r' \, \mathrm{d}t' \, . \tag{2.15}$$

The dielectric function and its inverse can be expressed in terms of χ and P as

$$\varepsilon^{-1} = 1 + v\chi \quad \text{and} \quad \varepsilon = 1 - vP, \tag{2.16}$$

where v denotes the Coulomb potential. The response functions P and χ are in turn related to each other by the Dyson equation

$$\chi = P + Pv\chi. \tag{2.17}$$

Remark. The approximation of a purely longitudinal external electric field made in eq. (2.11) is reasonable for the description of the response to an electron passing through the system. The electric field of light, on the other hand, is purely transversal and would require a response function relating the external and total vector potential $\boldsymbol{A}$ (in the Coulomb gauge). Fortunately, in the limit of long wave-lengths or vanishing $\boldsymbol{q}$, it was shown that the purely longitudinal and purely transversal response become equal in crystalline systems of cubic [13] and lower [14] symmetry.

2.3. Susceptibility from time-dependent perturbation theory

The variation of an observable $f(t)$ due to a perturbation $\hat{\mathrm{H}}'(t)$, which was switched on at time t_0, can be computed by first-order time-dependent perturbation theory according to [15]

$$\tilde{f}(t) = \langle \Psi_{\mathrm{S}}(t) | \hat{\mathrm{f}}_{\mathrm{S}}(t) | \Psi_{\mathrm{S}}(t) \rangle - \left\langle \Psi^0_{\mathrm{H}} \middle| \hat{\mathrm{f}}_{\mathrm{H}}(t) \middle| \Psi^0_{\mathrm{H}} \right\rangle = \frac{\mathrm{i}}{\hbar} \int_{t_0}^{t} \left\langle \Psi^0_{\mathrm{H}} \middle| \left[\hat{\mathrm{H}}'_{\mathrm{H}}(t'), \hat{\mathrm{f}}_{\mathrm{H}}(\boldsymbol{r}, t) \right]_- \middle| \Psi^0_{\mathrm{H}} \right\rangle \mathrm{d}t' \,, \tag{2.18}$$

where the subscript H (S) denotes the Heisenberg (Schrödinger) picture and Ψ^0_{H} is the normalized ground state of the unperturbed system, while $\Psi_{\mathrm{S}}(t)$ is the exact state of the perturbed system which evolves from $\Psi^0_{\mathrm{S}}(t_0)$. If we consider a perturbation due to an external scalar potential, $\hat{\mathrm{H}}'$ takes on the form

$$\hat{\mathrm{H}}'_{\mathrm{H}}(t) = \int \hat{\rho}_{\mathrm{H}}(\boldsymbol{r}, t) \varphi^{\mathrm{ext}}(\boldsymbol{r}, t) \, \mathrm{d}^3 r = \int \hat{\mathrm{n}}_{\mathrm{H}}(\boldsymbol{r}, t) e \varphi^{\mathrm{ext}}(\boldsymbol{r}, t) \, \mathrm{d}^3 r \,, \tag{2.19}$$

and the variation of the density $n(\boldsymbol{r})$ follows as

$$\tilde{n}(\boldsymbol{r}, t) = \frac{\mathrm{i}}{\hbar} \int_{t_0}^{t} \mathrm{d}t' \int \mathrm{d}^3 r' \; e \varphi^{\mathrm{ext}}(\boldsymbol{r}', t') \left\langle \Psi^0_{\mathrm{H}} \middle| \left[\hat{\mathrm{n}}_{\mathrm{H}}(\boldsymbol{r}', t'), \hat{\mathrm{n}}_{\mathrm{H}}(\boldsymbol{r}, t) \right]_- \middle| \Psi^0_{\mathrm{H}} \right\rangle . \tag{2.20}$$

This can be rewritten in terms of the *density deviation operator* $\hat{\tilde{\mathrm{n}}}_H$

$$\hat{\tilde{\mathrm{n}}}_{\mathrm{H}} = \hat{\mathrm{n}}_{\mathrm{H}} - \left\langle \Psi^0_{\mathrm{H}} \middle| \hat{\mathrm{n}}_{\mathrm{H}} \middle| \Psi^0_{\mathrm{H}} \right\rangle \tag{2.21}$$

by simply replacing $\hat{\mathrm{n}}_{\mathrm{H}}$ with $\hat{\tilde{\mathrm{n}}}_{\mathrm{H}}$ in eq. (2.20). Then, the susceptibility defined in eq. (2.14) can be identified with the *retarded density correlation function*

$$\chi^{\mathrm{R}}(\boldsymbol{r}, \boldsymbol{r}', t - t') = \frac{\delta n_{\mathrm{ind}}(\boldsymbol{r}, t)}{\delta e \varphi_{\mathrm{ext}}(\boldsymbol{r}', t')} = \frac{-i}{\hbar} \theta(t - t') \left\langle \Psi^0_{\mathrm{H}} \middle| \left[\hat{\tilde{\mathrm{n}}}_{\mathrm{H}}(\boldsymbol{r}, t), \hat{\tilde{\mathrm{n}}}_{\mathrm{H}}(\boldsymbol{r}', t') \right]_- \middle| \Psi^0_{\mathrm{H}} \right\rangle . \tag{2.22}$$

Equation (2.22) thus connects the classical dielectric response to a quantum mechanical expectation value in the unperturbed system. In order to apply many-body perturbation methods, it is necessary to introduce the related *time-ordered density correlation function*

$$\chi^{\mathrm{T}}(\boldsymbol{r}, \boldsymbol{r}', t - t') = \frac{-i}{\hbar} \left\langle \Psi^0_{\mathrm{H}} \middle| \hat{\mathscr{T}} \left[\hat{\tilde{\mathrm{n}}}_{\mathrm{H}}(\boldsymbol{r}, t) \hat{\tilde{\mathrm{n}}}_{\mathrm{H}}(\boldsymbol{r}', t') \right] \middle| \Psi^0_{\mathrm{H}} \right\rangle , \tag{2.23}$$

where $\hat{\mathscr{T}}$ is the Wick's time-ordering operator. There is a straightforward relation between the retarded and time-ordered correlation functions [15]:

$$\chi^{\mathrm{T}}(\boldsymbol{r}, \boldsymbol{r}', \omega) = \chi^{\mathrm{R}}(\boldsymbol{r}, \boldsymbol{r}', \omega) \quad \text{and} \quad \chi^{\mathrm{R}}(\boldsymbol{r}, \boldsymbol{r}', -\omega) = \left(\chi^{\mathrm{R}}(\boldsymbol{r}, \boldsymbol{r}', \omega) \right)^* , \omega > 0. \tag{2.24}$$

The methods needed to evaluate eqs. (2.22) and (2.23) in a solid will be discussed in chapter 3.

2.4. Connection to measurable quantities

2.4.1. Dynamical structure factor

In both *angular resolved electron energy loss spectroscopy (AR-EELS)* and *inelastic X-ray scattering (IXS)* the *double differential cross section* $\frac{\partial^2\sigma}{\partial\Omega\partial E}$ is measured. It quantifies the probability that an incoming particle (electron or photon, respectively) is scattered into the solid angle Ω and looses the energy E. If the incoming particle can be described with a single plane wave, the double differential cross section can be written in terms of the *dynamic structure factor S (DSF)* and the so-called *probe factor C*

$$\frac{\partial^2\sigma}{\partial\Omega\partial E} = C(\boldsymbol{q})S(\boldsymbol{q}, E), \tag{2.25}$$

where $\boldsymbol{q} = \boldsymbol{k}_\mathrm{i} - \boldsymbol{k}_\mathrm{f}$ is the difference in wave vector between the incoming and the scattered particle. The DSF is purely a property of the target material and thus it is independent of the scattering particle. Hence, both AR-EELS and IXS allow for the determination of the structure factor and only differ in the probe factors. When the incoming particle is instead described by a coherent sum of plane waves, eq. (2.25) can be generalized and the target properties are then described by the *mixed dynamic form factor* $S(\boldsymbol{q}, \boldsymbol{q}', E)$ (MDFF). The *(generalized) fluctuation-dissipation theorem* now relates the (MDFF) DSF with the retarded density correlation function [11]:

$$S(\boldsymbol{q}, \boldsymbol{q}', E) = \frac{\mathrm{i}}{2\pi}\left[\chi^\mathrm{R}(\boldsymbol{q}, \boldsymbol{q}', E) - \left(\chi^\mathrm{R}(\boldsymbol{q}', \boldsymbol{q}, E)\right)^*\right], E > 0 \tag{2.26a}$$

$$S(\boldsymbol{q}, E) = S(\boldsymbol{q}, \boldsymbol{q}, E) = -\frac{1}{\pi}\Im\left[\chi^\mathrm{R}(\boldsymbol{q}, \boldsymbol{q}, E)\right], E > 0. \tag{2.26b}$$

The DSF can thus be connected to the microscopic dielectric function using eq. (2.16)

$$S(\boldsymbol{q}, \omega) = -\frac{1}{\pi}v^{-1}(\boldsymbol{q})\Im\left[\varepsilon^{-1}(\boldsymbol{q}, \boldsymbol{q}, \omega)\right]. \tag{2.27}$$

Another related quantity is the *electron energy loss function* $L(\boldsymbol{q}, \omega)$ which is defined as

$$L(\boldsymbol{q}, \omega) = -\Im\left[\varepsilon^{-1}(\boldsymbol{q}, \boldsymbol{q}, \omega)\right]. \tag{2.28}$$

2.4.2. Optical absorption spectrum

In the case of vanishing $\boldsymbol{q}$ the longitudinal dielectric function can also be used to describe the transversal response [16, 17]. We write (see eqs. (2.10), (2.11) and (2.13))

$$\varepsilon^{\alpha\beta}_\mathrm{TT}(\omega) \coloneqq \lim_{q\to 0}\varepsilon^{\alpha\beta}_\mathrm{TT}(\boldsymbol{q}, \boldsymbol{q}, \omega) = \lim_{q\to 0}\varepsilon^{\alpha\beta}_\mathrm{LL}(\boldsymbol{q}, \boldsymbol{q}, \omega) = \lim_{q\to 0}\frac{q_\alpha\varepsilon(\boldsymbol{q}, \boldsymbol{q}, \omega)q_\beta}{|\boldsymbol{q}|^2}. \tag{2.29}$$

In experiments one generally measures an averaged response instead of the microscopic one. In order to account for this, we average the microscopic dielectric function over some mesoscopic volume and define the *macroscopic dielectric function* ε_M as

$$\left\langle\varepsilon^{\alpha\beta}_\mathrm{TT}\right\rangle(\omega) = \lim_{q\to 0}\frac{q_\alpha\langle\varepsilon\rangle(\boldsymbol{q}, \boldsymbol{q}, \omega)q_\beta}{|\boldsymbol{q}|^2} =: \lim_{q\to 0}\frac{q_\alpha\varepsilon_\mathrm{M}(\boldsymbol{q}, \omega)q_\beta}{|\boldsymbol{q}|^2}. \tag{2.30}$$

The imaginary part the macroscopic dielectric function $\Im\left[\varepsilon_{\mathrm{M}}(\omega)\right]$ is often equated with the *optical absorption spectrum* [5]. Following [18], this can be motivated when we consider the energy per unit time dissipated in the medium expressed via the induced current and the field within the medium

$$P(t) = \int \boldsymbol{j}^{\mathrm{ind}}(\boldsymbol{r}, t)\boldsymbol{E}(\boldsymbol{r}, t)\,\mathrm{d}^3 r\,. \tag{2.31}$$

We now make the assumption that the electric field in the medium is purely transversal and of a defined wave vector $\boldsymbol{q}$ and frequency ω, i.e.

$$\boldsymbol{E}(\boldsymbol{r}, t) = \hat{\boldsymbol{e}} E_0 \mathrm{e}^{\mathrm{i}(\boldsymbol{q}\boldsymbol{r}-\omega t)} + \text{c.c.}. \tag{2.32}$$

Additionally, we assume that the induced current has the same time and space dependence as the electric field and is linearly related to it:

$$\boldsymbol{j}^{\mathrm{ind}}(\boldsymbol{r}, t) = \sigma(\boldsymbol{q}, \omega)\hat{\boldsymbol{e}} E_0 \mathrm{e}^{\mathrm{i}(\boldsymbol{q}\boldsymbol{r}-\omega t)} + \text{c.c.}, \tag{2.33}$$

where σ defines the *transverse conductivity*. Under these assumptions, P is constant in time and proportional to the real part of σ

$$P \propto \left|E_0\right|^2 \sigma_1(\boldsymbol{q}, \omega). \tag{2.34}$$

Then using the Maxwell equations, σ and ε can be related, in particular the real part of σ is given in terms of the imaginary part of ε:

$$\sigma_1(\boldsymbol{q}, \omega) \propto \omega\varepsilon_2(\boldsymbol{q}, \omega). \tag{2.35}$$

Consequently, the features of the absorption spectrum are defined by those of the imaginary part of the dielectric function. For anisotropic materials, however, this connection cannot be drawn as directly.

2.5. Response of a crystalline system

In a periodic crystal with Born-von-Karman boundary condition, we can write the Fourier transform of eq. (2.12) in terms of the reciprocal lattice vectors $\boldsymbol{G}$ and the reciprocal unit cell vectors $\boldsymbol{q}$ as (see Appendix B)

$$\varphi^{\mathrm{ext}}_{\boldsymbol{G}}(\boldsymbol{q}, \omega) = \sum_{\boldsymbol{G}'} \varepsilon_{\boldsymbol{G}\boldsymbol{G}'}(\boldsymbol{q}, \boldsymbol{q}, \omega)\varphi_{\boldsymbol{G}'}(\boldsymbol{q}, \omega), \tag{2.36}$$

where we assume the response function to be lattice periodic $\varepsilon(\boldsymbol{r} + \boldsymbol{R}, \boldsymbol{r}' + \boldsymbol{R}) = \varepsilon(\boldsymbol{r}, \boldsymbol{r})$. Equation (2.36) highlights that even if the external potential is varying slowly, i.e. only Fourier coefficients with $\boldsymbol{G} = 0$ are non-zero, the resulting total potential varies on a small scale (it contains large $\boldsymbol{G}$ components). These deviations from the external potential are commonly referred to as *local field effects*, and the sum eq. (2.36) must be used to account for them.

Analogously, we can write for the inverse microscopic dielectric function

$$\varepsilon^{-1}_{\boldsymbol{G}\boldsymbol{G}'}(\boldsymbol{q},\omega) = 1 + v_{\boldsymbol{G}}(\boldsymbol{q})\chi^{\mathrm{R}}_{\boldsymbol{G}\boldsymbol{G}'}(\boldsymbol{q},\omega). \tag{2.37}$$

The dynamical structure factor for the momentum transfer $\boldsymbol{Q}_{\mathrm{mt}} = \boldsymbol{G}_{\mathrm{mt}} + \boldsymbol{q}_{\mathrm{mt}}$ takes on the form

$$S_{\boldsymbol{G}_{\mathrm{mt}}}(\boldsymbol{q}_{\mathrm{mt}},\omega) = -\frac{1}{\pi} v^{-1}_{\boldsymbol{G}_{\mathrm{mt}}}(\boldsymbol{q}_{\mathrm{mt}}) \Im\left[\varepsilon^{-1}_{\boldsymbol{G}_{\mathrm{mt}}\boldsymbol{G}_{\mathrm{mt}}}(\boldsymbol{q}_{\mathrm{mt}},\boldsymbol{q}_{\mathrm{mt}},\omega)\right]. \tag{2.38}$$

2.5.1. Macroscopic dielectric response

For a crystalline system the mesocopic averaging mentioned in section 2.4.2 is usually done over the volume of a unit cell which is equivalent to taking only the $\boldsymbol{G} = 0$ component of the Fourier transform unequal to zero [19, 20]. Consequently, a macroscopic response function relates the $\boldsymbol{G} = 0$ components of two quantities. When we assume that the external potential is also macroscopic, i.e. $\varphi^{\mathrm{ext}}_{\boldsymbol{G}}(\boldsymbol{q}) = \delta_{\boldsymbol{G},0}\varphi^{\mathrm{ext}}(\boldsymbol{q})$, we find for the *macroscopic inverse longitudinal dielectric function* ε_M:

$$\varphi_0(\boldsymbol{q},\omega) = \varepsilon^{-1}_{00}(\boldsymbol{q},\boldsymbol{q},\omega)\varphi^{\mathrm{ext}}_0(\boldsymbol{q},\omega) =: \varepsilon^{-1}_{\mathrm{M}}(\boldsymbol{q},\omega)\varphi^{\mathrm{ext}}_0(\boldsymbol{q},\omega). \tag{2.39}$$

The equation above also allows for the definition of the *macroscopic longitudinal dielectric function* as

$$\varphi^{\mathrm{ext}}_0(\boldsymbol{q},\omega) = \frac{1}{\varepsilon^{-1}_{\mathrm{M}}(\boldsymbol{q},\omega)}\varphi_0(\boldsymbol{q},\omega) =: \varepsilon_{\mathrm{M}}(\boldsymbol{q},\omega)\varphi_0(\boldsymbol{q},\omega). \tag{2.40}$$

In view of eq. (2.27), we formally extend the definition of ε_{M} to also include the case of $\boldsymbol{G} \neq 0$

$$\varepsilon_{\mathrm{M}}(\boldsymbol{Q},\omega) = \frac{1}{\varepsilon^{-1}_{\boldsymbol{G}\boldsymbol{G}}(\boldsymbol{q},\omega)}. \tag{2.41}$$

Then we can write for the dynamical structure factor

$$S(\boldsymbol{Q},\omega) = -\frac{1}{\pi} v^{-1}_{\boldsymbol{G}}(\boldsymbol{q}) \Im\left[\frac{1}{\varepsilon_{\mathrm{M}}(\boldsymbol{Q},\omega)}\right]. \tag{2.42}$$

For the limit of vanishing momentum transfer the macroscopic dielectric function can be most conveniently computed by introducing a modified polarizability $\bar{P}$ [5]

$$\bar{P} = P + P\bar{v}\bar{P}, \tag{2.43}$$

which is related to the polarizability P through the long-range-truncated Coulomb potential

$$\bar{v}_{\boldsymbol{G}}(\boldsymbol{q}) = \begin{cases} v_{\boldsymbol{G}}(\boldsymbol{q}) & \text{for} \quad \boldsymbol{G} \neq 0 \\ 0 & \text{otherwise} \end{cases}. \tag{2.44}$$

Using this approach we can take the limit $\boldsymbol{q} \to 0$ in eq. (2.16) and write

$$\varepsilon_M(\omega) = 1 - \lim_{q\to 0} v_0(\boldsymbol{q})\bar{P}_{00}(\boldsymbol{q},\omega). \tag{2.45}$$

3. The many-body problem in solid-state physics

In this chapter, we summarize some key concepts used in the *ab initio* quantum mechanical description of a solid as an electronic many-body system. First, the Hamiltonian for a general N-electron system is presented in section 3.1, as a starting point for the following discussions. Then, as an alternative approach to the problem, the main ideas and results of *density-functional theory* are presented in section 3.2. In section 3.3 the formalism of *Green's function theory* as a means to describe elementary excitations of the system and the *quasi-particle*-picture are introduced. In section 3.3.3 the one-particle Green's function, or propagator, and Hedin's equations are discussed. Subsequently, in section 3.3.4, the derivation of the *Bethe-Salpeter equation* (BSE) in the so-called *GW*-approximation for static screening is outlined starting from the two-particle propagator. Lastly, the diagrammatic representations of the BSE and the *Tamm-Dancoff-approximation* are discussed in section 3.3.5.

3.1. The electronic many-body system

The many electron system we are interested in is described by a Hamiltonian of the form

$$\hat{\mathrm{H}} = \hat{\mathrm{T}} + \hat{\mathrm{V}} + \hat{\mathrm{U}}, \tag{3.1}$$

where $\hat{\mathrm{T}}$ and $\hat{\mathrm{V}}$ are the summed one-particle operators describing the kinetic and potential energy of N electrons in an external potential, while $\hat{\mathrm{U}}$ contains the two-electron Coulomb repulsion terms. In atomic units the operators are given by

$$\hat{\mathrm{T}} = \sum_{i=1} \hat{\mathrm{t}}_i = -\frac{1}{2} \sum_{i=1} \nabla_i^2 \qquad \hat{\mathrm{V}} = \sum_{i=1} v_{\mathrm{ext}}(\boldsymbol{r}_i), \tag{3.2a}$$

$$\hat{\mathrm{U}} = \frac{1}{2} \sum_{i \neq j} v(\boldsymbol{r}_i, \boldsymbol{r}_j) = \sum_{i,j} \frac{1}{\left|\boldsymbol{r}_i - \boldsymbol{r}_j\right|} \qquad v_{\mathrm{ext}}(\boldsymbol{r}; \{\boldsymbol{R}_n\}) = -\sum_{i=1}^{N_{\mathrm{nuc}}} \frac{Z_i}{\left|\boldsymbol{r} - \boldsymbol{R}_i\right|}. \tag{3.2b}$$

The external potential v_{ext} is generated by the positively charged atomic nuclei which are assumed to be in a fixed arrangement. A direct solution of the full N-electron Schrödinger equation

$$\hat{\mathrm{H}} \Phi\left(\{\boldsymbol{r}_i\}; \{\boldsymbol{R}_i\}\right) = \mathrm{i} \frac{\partial}{\partial t} \Phi\left(\{\boldsymbol{r}_i\}; \{\boldsymbol{R}_i\}\right) \tag{3.3}$$

for any realistic system is not feasible due to its high dimensionality[1]. This problem is lifted in the framework of density-functional theory.

[1] A 1 cm^3 cube of silicon contains about 10^{23} electrons

3.2. Density-functional theory

In the context of density-functional theory, pioneered by the works of Thomas [21] and Fermi [22] and formalized by Hohenberg and Kohn [23], the focus is shifted away from the many-electron wave-function onto the electron density as the quantity describing the system.

3.2.1. Hohenberg-Kohn theorems

The theory is founded on the so called *Hohenberg-Kohn theorem* that states [23]:

Theorem 1. *There is a one-to-one correspondence between the ground state electron density of a bound system of interacting electrons and the external potential.*

Corollary 1.1. *Every observable and the wave-function of the system can be expressed as a functional of the ground state density.*

In particular, the sum of the electron-electron Coulomb interaction $\hat{\mathrm{U}}$ and the kinetic energy of the electrons $\hat{\mathrm{T}}$

$$F[n] = \langle \Phi | \hat{\mathrm{T}} + \hat{\mathrm{U}} | \Phi \rangle \tag{3.4}$$

is uniquely defined by the ground state density and has the *same form for all many-electron systems* of the considered form.

The second theorem of Hohenberg and Kohn, also known as *Hohenberg-Kohn minimum principle*, states:

Theorem 2. *The total energy is a functional of the electron density with its minimal value, the ground state energy, at the ground state density*

$$E_{gs} = E[n_{gs}] = \min_{n(\boldsymbol{r})} E[n(\boldsymbol{r})] = \min_{n(\boldsymbol{r})} \left\{ \int n(\boldsymbol{r}) v_{ext}(\boldsymbol{r}) \, \mathrm{d}^3 r + F[n] \right\}. \tag{3.5}$$

3.2.2. The Kohn-Sham equations

While in theory every observable of the N-electron system is a functional of the density, the explicit form of $F[n]$ is not known. In an effort to make the problem more tractable, Kohn and Sham [24] expressed the universal functional as

$$F[n(\boldsymbol{r})] = T_0[n(\boldsymbol{r})] + \frac{1}{2} \iint \frac{n(\boldsymbol{r}_1) n(\boldsymbol{r}_2)}{|\boldsymbol{r}_1 - \boldsymbol{r}_2|} \, \mathrm{d}^3 r_1 \, \mathrm{d}^3 r_2 + E_{\mathrm{xc}}[n(\boldsymbol{r})], \tag{3.6}$$

where $T_0[n]$ is the kinetic energy functional of *non-interacting* electrons, the second summand is the electrostatic Hartee-energy and $E_{\mathrm{xc}}[n]$ is the *exchange-correlation energy functional*. The latter encapsulates all quantum-mechanical many-body effects and needs to be approximated.

By applying the Hohenberg-Kohn minimum principle Kohn and Sham were able to define an *auxiliary system of non-interacting electrons that leads to the exact same ground-state density as the fully interacting system*, given the exact form of the exchange-correlation energy functional:

$$\left[-\frac{1}{2}\nabla^2 + v_{\text{eff}}(\boldsymbol{r}) - \epsilon_i\right]\phi_i(\boldsymbol{r}) =: \hat{\text{h}}_{\text{KS}}(\boldsymbol{r})\phi_i(\boldsymbol{r}) = 0, \tag{3.7a}$$

where

$$v_{\text{eff}}(\boldsymbol{r}) = v_{\text{ext}}(\boldsymbol{r}) + \int \frac{n(\boldsymbol{r}_2)}{\left|\boldsymbol{r} - \boldsymbol{r}_2\right|}\,\mathrm{d}^3 r_2 + v_{\text{xc}}(\boldsymbol{r}) \tag{3.7b}$$

and

$$v_{\text{xc}}(\boldsymbol{r}) = \left.\frac{\delta E_{\text{xc}}[n(\boldsymbol{r})]}{\delta n(\boldsymbol{r})}\right|_{n=n_{\text{gs}}}. \tag{3.7c}$$

Equation (3.7c) defines the *exchange-correlation potential*. The electron density can be directly calculated using the single-particle orbitals

$$n(\boldsymbol{r}) = \sum_{i=1}^{N} \left|\phi_i(\boldsymbol{r})\right|, \tag{3.8}$$

and the total energy reads in terms of the density and the Kohn-Sham eigenvalues

$$E = \sum_{i=1}^{N} \epsilon_i + E_{\text{xc}}[n(\boldsymbol{r})] - \int v_{\text{xc}}(\boldsymbol{r}) n(\boldsymbol{r})\,\mathrm{d}^3 r - \frac{1}{2}\int \frac{n(\boldsymbol{r}_1)n(\boldsymbol{r}_2)}{\left|\boldsymbol{r}_1 - \boldsymbol{r}_2\right|}\,\mathrm{d}^3 r_1\,\mathrm{d}^3 r_2\,. \tag{3.9}$$

Starting from an assumed form of $E_{\text{xc}}[n]$, equations (3.7), (3.8) and (3.9) need to be solved self-consistently for the ground-state density.

Remark. The Kohn-Sham eigenvalues and Kohn-Sham orbitals contain *a priori* no physical meaning, as they are auxiliary quantities designed to reproduce the ground state electron density of the real system. In practice, however, they are still used to approximate band structures and wave functions and often yield reasonable results when compared with experiments and higher order theories.

In principle, all many-body effects of the interacting system are described in the exchange-correlation energy functional, and consequently the Kohn-Sham system with the corresponding exchange-correlation potential can reproduce the exact ground state density and energy. Unfortunately, the exact form of the functional is not known and approximations need to be made. In this work we will exclusively use the *local density approximation* (LDA) [24] which assumes the system to locally resemble the homogeneous electron gas.

3.3. Many-body perturbation theory

If one is interested in the excitation properties of a system of interacting electrons it does not suffice to look at the Kohn-Sham eigenvalues, as they are purely auxiliary quantities. Instead one has to venture into the realm of many-body perturbation theory (MBPT) within the (non-relativistic) second quantization formulation of the many-electron system (for a review see [3, 5]). In this section, the basic concepts will be outlined following mainly Refs. [3, 12, 19, 20].

3.3.1. Hamiltonian in second quantization

In MBPT it is necessary to switch to the occupation number representation of the second quantization formalism. The system described by eq. (3.1) now reads

$$\hat{\mathrm{H}} = \int \hat{\Psi}^\dagger(\boldsymbol{r}) h(\boldsymbol{r}) \hat{\Psi}(\boldsymbol{r}) \,\mathrm{d}^3 r + \frac{1}{2} \iint \hat{\Psi}^\dagger(\boldsymbol{r}) \hat{\Psi}^\dagger(\boldsymbol{r}') v(\boldsymbol{r}, \boldsymbol{r}') \hat{\Psi}(\boldsymbol{r}') \hat{\Psi}(\boldsymbol{r}) \,\mathrm{d}^3 r \,\mathrm{d}^3 r' \,. \tag{3.10}$$

The fermionic field operators $\hat{\Psi}^\dagger(\boldsymbol{r})$ and $\hat{\Psi}(\boldsymbol{r})$ create and destroy an electron at position $\boldsymbol{r}$, respectively, and fulfill the equal-time anti-commutation relations

$$\left[\hat{\Psi}(\boldsymbol{r}), \hat{\Psi}(\boldsymbol{r}')\right]_+ = \left[\hat{\Psi}^\dagger(\boldsymbol{r}), \hat{\Psi}^\dagger(\boldsymbol{r}')\right]_+ = 0 \quad \text{and} \quad \left[\hat{\Psi}(\boldsymbol{r}), \hat{\Psi}^\dagger(\boldsymbol{r}')\right]_+ = \delta(\boldsymbol{r} - \boldsymbol{r}'). \tag{3.11}$$

Instead of the Schrödinger equation (3.3), the equation of motion of the field operators in the Heisenberg picture is considered to describe the evolution of the system

$$\mathrm{i} \frac{\partial}{\partial t} \hat{\Psi}_\mathrm{H}(\boldsymbol{r}, t) = \left[\hat{\Psi}_\mathrm{H}(\boldsymbol{r}, t), \hat{\mathrm{H}}\right] = \left[\hat{\mathrm{h}}(\boldsymbol{r}) + \int v(\boldsymbol{r}, \boldsymbol{r}') \hat{\Psi}^\dagger_\mathrm{H}(\boldsymbol{r}', t) \hat{\Psi}_\mathrm{H}(\boldsymbol{r}', t) \,\mathrm{d}^3 r'\right] \hat{\Psi}_\mathrm{H}(\boldsymbol{r}, t). \tag{3.12}$$

The direct solution of eq. (3.12) is in general not possible so that perturbative methods need to be employed.

3.3.2. Quasi-particles

The key concept of MBPT is to replace the system of N strongly interacting particles with a system of N non- or weakly interacting *quasi-particles* that describe elementary excitations of the system with respect to some perturbation. When considering (inverse) photoemission experiments where electrons are (added) removed from the system, an appropriate quasi-particle picture would be that of *quasi-electrons* (*quasi-holes*). These quasi-particles closely resemble the real particles, but with properties such as charge, mass or momentum renormalized by the influence of all the other electrons in the system. On the other hand, in optical absorption measurements excitations remain charge neutral and can be described by the creation of electron-hole pairs. These pairs of correlated electrons and holes can be characterized as a new quasi-particle called *exciton*. The theoretical description of these quasi-particle is bases on the *n-particle Green's functions* (or propagators). They give a systematical approach to the interaction of a few particles with the rest of the fully interacting system.

3.3.3. One-particle Green's function and Hedin's equations

The *one-particle Green's function* [15]

$$G_1(\boldsymbol{r}_1, t_1; \boldsymbol{r}_2, t_2) = -\mathrm{i} \left\langle N \middle| \hat{\mathscr{T}} \left[\hat{\Psi}(\boldsymbol{r}_1, t_1) \hat{\Psi}^\dagger(\boldsymbol{r}_2, t_2)\right] \middle| N \right\rangle \tag{3.13}$$

can be interpreted as a measure for the probability of finding a particle at position $\boldsymbol{r}$ at time t, if a particle is introduced into the system at position $\boldsymbol{r}'$ at time t'. Here, $|N\rangle$ is the Heisenberg ground state of the many-body system and $\hat{\mathscr{T}}$ is Wick's time-ordering operator. This

Green's function contains all information about single-particle excitations of the system, and the expectation values of any single-particle observables can be computed with its help [15, 25]. Using functional-derivative methods [26–28], the interacting Green's function G_1 can be formulated in terms of the *non-interacting* Green's function G_0 and the *self-energy* Σ

$$G_0^{-1}(1,2) = G_1^{-1}(1,2) + \Sigma(1,2), \tag{3.14a}$$

$$G_1(1,2) = G_0(1,2) + \int G_0(1,3)\Sigma(3,4)G_1(4,2)\,\mathrm{d}(3,4)\,, \tag{3.14b}$$

where $1 \equiv (\boldsymbol{r}_1, t_1)$. G_0 describes the free propagation of a particle in the average electrostatic potential of the system, while exchange and correlation effects are packed into Σ. In order to get access to the self-energy, Hedin and Lundquist [12, 29] investigated the equation of motion of $G_1(1,2)$ for a Hamiltonian that is perturbed by a small local external scalar potential ϕ ($h(r) \to h(r) + \phi(r,t)$ in eq. (3.10)) and derived the following set of self-consistent integral equations, commonly referred to as *Hedin's equations*:

$$\Sigma(1,2) = \mathrm{i}\int W(1^+,3)G_1(1,4)\Gamma(4,2;3)\,\mathrm{d}(3,4) \tag{3.15a}$$

$$W(1,2) = v(1,2) + \int W(1,3)P(3,4)v(4,2)\,\mathrm{d}(3,4) \tag{3.15b}$$

$$P(1,2) = -\mathrm{i}\int G_1(2,3)G_1(4,2)\Gamma(3,4;1)\,\mathrm{d}(3,4) \tag{3.15c}$$

$$\Gamma(1,2;3) = \delta(1,2)\delta(1,3) + \frac{\delta\Sigma(1,2)}{\delta V(3)}. \tag{3.15d}$$

W denotes the *dynamically screened Coulomb interaction*, which is related to the *bare Coulomb interaction* v by the inverse (longitudinal) dielectric function ε^{-1}, according to:

$$W(1,2) = \int v(1,3)\varepsilon^{-1}(3,2)\,\mathrm{d}(3)\,. \tag{3.16}$$

The inverse of the dielectric function in eq. (3.16) is defined as the variation of the total average potential V of the system with respect to a scalar potential Φ (see section 2.2),

$$\varepsilon^{-1}(1,2) = \frac{\delta V(1)}{\delta\Phi(2)}. \tag{3.17}$$

Dyson's equation for G_1 (3.14) together with Hedin's equations (3.15) could be solved self-consistently starting with $\Sigma = 0$. In practice, however, this is computationally not feasible for realistic systems.

In order to make the system (3.15) tractable, the *vertex function* Γ is approximated by neglecting the variation of the self-energy with respect to the average potential V. The resulting system

$$\Sigma(1,2) = \mathrm{i}W(1^+,2)G_1(1,2) \tag{3.18a}$$

$$W(1,2) = v(1,2) + \int W(1,3)P(3,4)v(4,2)\,\mathrm{d}(3,4) \tag{3.18b}$$

$$P(1,2) = -\mathrm{i}G_1(1,2)G_1(2,1) \tag{3.18c}$$

is named the *GW approximation* due to the form of the self-energy. To further simplify the problem, the G_0W_0 approximation is often used, where the self-energy is approximated by one iteration of eq. (3.18) starting from G_0.

The Dyson equation eq. (3.14) can be reformulated in terms of the *quasi-particle wave functions* ψ as a Schrödinger-like equation

$$\hat{\mathrm{h}}(\boldsymbol{r})\psi_m(\boldsymbol{r}) + \int \Sigma(\boldsymbol{r},\boldsymbol{r}',E_m)\psi_m(\boldsymbol{r}')\,\mathrm{d}^3r' = E_m\psi_m(\boldsymbol{r}) \tag{3.19}$$

with the self energy considered as a non-local, energy-dependent potential [12, 30, 31]. The Green's function ($T = 0\,\mathrm{K}$) can be expressed in analogy to the independent-particle propagator using the solutions of eq. (3.19) as

$$G_1(\boldsymbol{r},\boldsymbol{r}',\omega) = \sum_m \frac{\psi_m(\boldsymbol{r})\psi_m^*(\boldsymbol{r}')}{\omega - E_m + \mathrm{i}\delta\,\mathrm{sgn}(E_m - E_\mathrm{f})}. \tag{3.20}$$

3.3.4. Two-particle Green's function and the Bethe-Salpether equation

To describe the perturbation discussed in chapter 2 in terms of Green's functions we also need to introduce the *two-particle Green's function*

$$\begin{aligned} &G_2(\boldsymbol{r}_1,t_1,\boldsymbol{r}_2,t_2;\boldsymbol{r}_1',t_1',\boldsymbol{r}_2',t_2') \\ &\qquad = (-\mathrm{i})^2\,\langle N|\hat{\mathscr{T}}\left[\hat{\Psi}_\mathrm{H}(\boldsymbol{r}_1,t_1)\hat{\Psi}_\mathrm{H}(\boldsymbol{r}_2,t_2)\hat{\Psi}_\mathrm{H}^\dagger(\boldsymbol{r}_2',t_2')\hat{\Psi}_\mathrm{H}^\dagger(\boldsymbol{r}_1',t_1')\right]|N\rangle\,, \end{aligned} \tag{3.21}$$

which describes the propagation of two particles through the system. Now, the time-ordered density correlation function (2.23) can be expressed with G_1 and G_2 by using $\hat{\mathrm{n}}_\mathrm{H}(r,t) = \hat{\Psi}_\mathrm{H}^\dagger(r,t)\,\hat{\Psi}_\mathrm{H}(r,t)$ as

$$\chi^\mathrm{T}(1,2) = \mathrm{i}\left[G_2(1,2,1^+,2^+) - G_1(1,1^+)G_1(2,2^+)\right] = -\mathrm{i}L(1,2,1^+,2^+), \tag{3.22}$$

where L denotes the *two-particle correlation function* [32] which is defined by

$$L(1,2,1',2') = G_2(1,2,1',2') - G_1(1,1')G_1(2,2'). \tag{3.23}$$

The equation of motion of L is described by the *Bethe-Salpeter equation for L* in the form of a Dyson's equation

$$\begin{aligned} L(1,2,1',2') &= L_0(1,2;1',2') \\ &\quad + \int L_0(1,4;1',3)\Xi(3,5;4,6)L(6,2;5,2')\,\mathrm{d}(3,4,5,6)\,. \end{aligned} \tag{3.24}$$

Here, L_0 describes the independent propagation of two particles

$$L_0(1,2;1',2') = G_1(1,2')G_1(2,1'), \tag{3.25}$$

and the effective two-particle interaction kernel Ξ is given in terms of the variation of the irreducible self-energy Σ (see 3.3.3) and the Hartree part of the self energy Σ_{H},

$$\Sigma_{\mathrm{H}}(3,4) = -\mathrm{i}\delta(3,4)\int \mathrm{d}(5)\, v(1,5)G_1(3,3^+) \tag{3.26}$$

with respect to the one-particle Green's function

$$\Xi(3,5;4,6) = \frac{\delta\left(\Sigma_{\mathrm{H}}(3,4) + \Sigma(3,4)\right)}{\delta G_1(6,5)}. \tag{3.27}$$

In the following, we will focus on the description of electron-hole pairs and exclude electron-electron or hole-hole pairs by requiring that $t_1 = t_1'$ and $t_2 = t_2'$. That is, we are only interested in charge-neutral excitations. In this framework L_0, for example, describes the *independent* propagation of an electron and a hole through the system and is only dependent on one time difference $t_2 - t_1$ [3].

Choosing the GW-approximation for the self-energy (3.18), the functional-derivative (3.27) is evaluated to yield:

$$\begin{aligned}\Xi(3,5,4,6) = -\mathrm{i}\delta(3,4)\delta(5,6)v(3,6) + \mathrm{i}\delta(3,6)\delta(4,5)W(3,5)\\ + \mathrm{i}G_1(3,5)\frac{\delta W(3,5)}{\delta G_1(6,4)}.\end{aligned} \tag{3.28}$$

The first term in eq. (3.28) describes the *repulsive exchange interaction*, while the second one accounts for the *screened electron-hole attraction*. The last term is neglected in practical applications, meaning that no change of the screening due to the excitations is considered.

To make the Bethe-Salpeter equation computationally more tractable, we approximate the interaction kernel (3.28) further by assuming that the screening is frequency independent, i.e. static, and all interactions are instantaneous

$$\begin{aligned}\Xi(3,5,4,6) \approx -\mathrm{i}\delta(3,4)\delta(5,6)v(\boldsymbol{r}_3,\boldsymbol{r}_6)\delta(t_3-t_6)\\ + \mathrm{i}\delta(3,6)\delta(4,5)W(\boldsymbol{r}_3,\boldsymbol{r}_5)\delta(t_3-t_5).\end{aligned} \tag{3.29}$$

This entails that the Fourier transform of the kernel in this approximation is *frequency-independent*, i.e. $\Xi(\omega) = \Xi$.

Once the BSE is solved for L, the density correlation function can be expressed using eq. (3.22). Form this function one can extract the dielectric response of the system which accounts for excitonic effects (see chapter 2).

3.3.5. BSE in diagrams

The integral equation (3.24) can be visualized in terms of Feynman diagrams according to

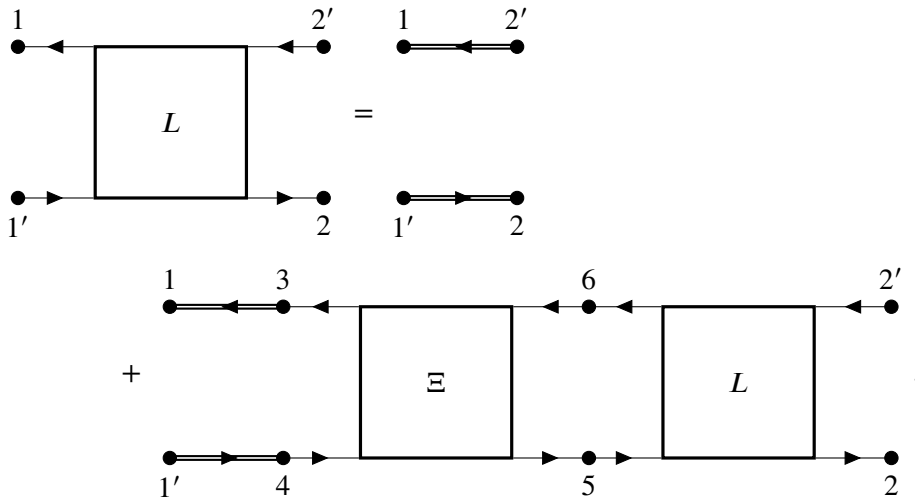

(3.30)

where we used the "box with four tails" notation of the four-point functions and we denote the quasi-particle propagator as $G(2,1) =$ 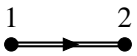 . The tails are not associated with any propagators but define how to connect propagators to the four-point function. The approximation for the interaction kernel Ξ (3.29) can be written diagrammatically as

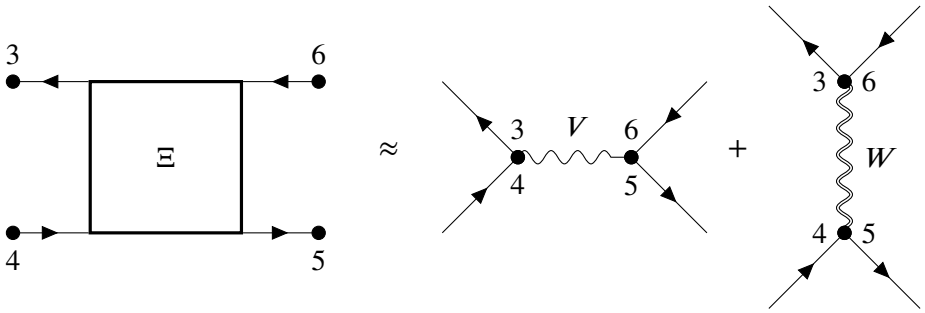

(3.31)

and the screened Coulomb interaction itself is given by the Dyson equation in terms of the irreducible polarization P

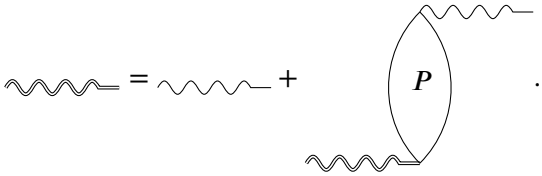

(3.32)

In the following, we will approximate P as

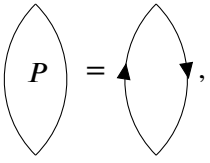

(3.33)

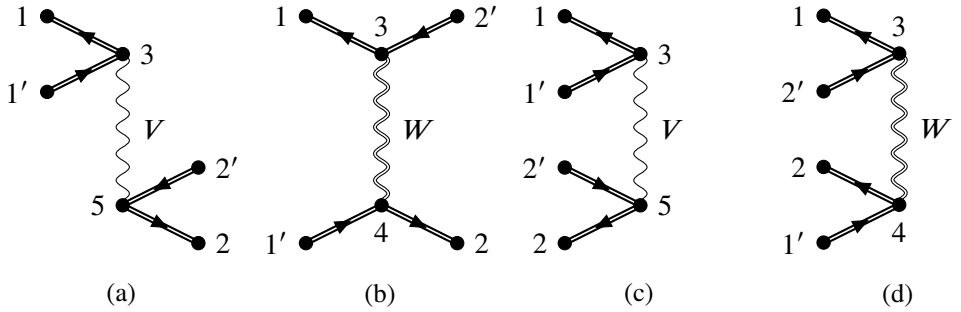

Figure 3.1.: First-order time-ordered Goldstone diagrams corresponding to the interactions mitigated by the bare (V) and the screened (W) Coulomb potential in the BSE (3.30) with the two-particle interaction kernel (3.31). Time increases from left to right. Diagrams (a) and (b) describe the resonant-resonant coupling between the e-h pairs ($11'$) and ($22'$), where both are associated with the frequency ω. Diagrams (c) and (d) describe the resonant-anti-resonant coupling, in which the ($22'$) pair is associated with the frequency of opposite sign. See also [9].

which is commonly referred to as *random phase approximation* (RPA) [33].

It is instructive to look at the time-ordered Goldstone versions of the first order interaction processes in eq. (3.30) with the kernel (3.31) as shown in figure 3.1. In the exchange diagram (a) the incoming electron-hole (e-h) pair ($11'$) is annihilated at $(\boldsymbol{r}_3, t_3)$ and the outgoing e-h pair ($22'$) is created at $(\boldsymbol{r}_5, t_3)$ with the same associated frequency ω. In contrast, in diagram (c) the incoming resonant e-h pair annihilates with an anti-resonant e-h pair of opposite frequency. Diagram (b) describes the scattering of the incoming resonant e-h pair into another resonant e-h pair of the same frequency. Lastly, in diagram (d) the incoming resonant e-h pair scatters into an anti-resonant e-h pair of opposite frequency.

A common approximation to the BSE is the so-called *Tamm-Dancoff approximation*, where no coupling between resonant and anti-resonant e-h pairs is regarded, i.e. diagrams of the type (c) and (d) are neglected. Within the TDA there is only one electron-hole pair present at any given time, whereas any number of electron-hole pairs are permitted otherwise [15].

4. Solving the Bethe-Salpeter equation

In this chapter we discuss how to bring the BSE into a numerically accessible form. In section 4.1 the integral equation (3.24) is written in matrix notation by expanding all functions in terms of a two-particle basis. Then, the formulation of the BSE is specialized for crystalline systems in section 4.2 and the explicit expressions of the momentum-transfer dependent matrix elements are derived in section 4.3. Subsequently, in sections 4.4 to 4.6 the connection between the eigen-solutions of an effective two-particle Hamiltonian and the reducible polarization function is made. Finally, in section 4.7 the computation of the macroscopic dielectric tensor in the limit of vanishing momentum transfer is discussed.

4.1. Matrix form of the BSE

We start by defining the four-point extension of the time-ordered density-correlation function eq. (3.22) as

$$\chi(1,2,1',2') \coloneqq -\mathrm{i}L(1,2,1',2'), \tag{4.1}$$

where $\chi(1,2) = \chi(1,2,1,2)$. Then, using the approximate (static) interaction kernel (3.29), the BSE eq. (3.24) can be Fourier transformed in the time difference $t_2 - t_1$ resulting in

$$\begin{aligned}\chi(\boldsymbol{r}_1,\boldsymbol{r}_2,\boldsymbol{r}_1',\boldsymbol{r}_2',\omega) &= \chi_0(\boldsymbol{r}_1,\boldsymbol{r}_2,\boldsymbol{r}_1',\boldsymbol{r}_2',\omega) \\ &+ \int \chi_0(\boldsymbol{r}_1,\boldsymbol{r}_4,\boldsymbol{r}_1',\boldsymbol{r}_3,\omega)\Xi(\boldsymbol{r}_3,\boldsymbol{r}_5,\boldsymbol{r}_4,\boldsymbol{r}_6)\chi(\boldsymbol{r}_6,\boldsymbol{r}_2,\boldsymbol{r}_5,\boldsymbol{r}_2',\omega)\,\mathrm{d}^3r_3\,\mathrm{d}^3r_4\,\mathrm{d}^3r_5\,\mathrm{d}^3r_6\,. \end{aligned} \tag{4.2}$$

With the independent quasi-particle approximation of the one-particle Green's function eq. (3.20), the Fourier transform of $\chi_0 = -\mathrm{i}L_0$ eq. (3.25) takes on the form (see Appendix F)

$$\chi_0(\boldsymbol{r}_1,\boldsymbol{r}_2,\boldsymbol{r}_1',\boldsymbol{r}_2',\omega) = \sum_{o,u} \frac{\psi_o(\boldsymbol{r}_1)\psi_u^*(\boldsymbol{r}_1')\psi_o^*(\boldsymbol{r}_2')\psi_u(\boldsymbol{r}_2)}{\omega - (\varepsilon_u - \varepsilon_o) + \mathrm{i}\delta} + \frac{\psi_u(\boldsymbol{r}_1)\psi_o^*(\boldsymbol{r}_1')\psi_u^*(\boldsymbol{r}_2')\psi_o(\boldsymbol{r}_2)}{-\omega - (\varepsilon_u - \varepsilon_o) + \mathrm{i}\delta}. \tag{4.3}$$

Equation (4.3) suggests the introduction of a two-particle basis $\Upsilon_j(\boldsymbol{r},\boldsymbol{r}')$ that is split into two subspaces according to

$$\Upsilon_\alpha^{\mathrm{r}}(\boldsymbol{r},\boldsymbol{r}') = \psi_{o_\alpha}(\boldsymbol{r})\psi_{u_\alpha}^*(\boldsymbol{r}') \quad \text{and} \quad \Upsilon_\alpha^{\mathrm{a}}(\boldsymbol{r},\boldsymbol{r}') = \psi_{u_\alpha}(\boldsymbol{r})\psi_{o_\alpha}^*(\boldsymbol{r}'). \tag{4.4}$$

The superscripts r and a denote the resonant and anti-resonant subspaces respectively, and the subscript α labels a combination of one unoccupied and one unoccupied state. In other words, α labels the independent (quasi-)particle transitions. Resonat (anti-resonant) refers here to the part of χ_0 that has poles when ω is positive (negative).

By restricting the one-particle Hilbert space to the span of a finite number of N_o occupied and N_u unoccupied orbitals, the Bethe-Salpeter equation (4.2) can be written as a matrix equation in the two-particle basis (4.4):

$$\chi_{ij}(\omega) = \chi_{0ij}(\omega) + \sum_{kl} \chi_{0ik}(\omega) \underbrace{\left(V_{kl} - W_{kl}\right)}_{\Xi_{kl}} \chi_{lj}(\omega). \tag{4.5}$$

Using the basis functions of (4.4), the matrix elements of the kernel are computed according to the prescription

$$\Xi^{\mathrm{rr}}_{\alpha\alpha'} = \iiiint \Upsilon^{\mathrm{r}*}_{\alpha}(\boldsymbol{r}_1, \boldsymbol{r}_1')\Xi(\boldsymbol{r}_1, \boldsymbol{r}_2, \boldsymbol{r}_1', \boldsymbol{r}_2')\Upsilon^{\mathrm{r}}_{\alpha'}(\boldsymbol{r}_2', \boldsymbol{r}_2)\,\mathrm{d}^3r_1\,\mathrm{d}^3r_1'\,\mathrm{d}^3r_2\,\mathrm{d}^3r_2', \tag{4.6}$$

and the ra-, ar- and aa-blocks are computed analogously. In this notation, the exchange part of Ξ is

$$\Xi_v(\boldsymbol{r}_1, \boldsymbol{r}_2, \boldsymbol{r}_1', \boldsymbol{r}_2') = \delta(\boldsymbol{r}_1 - \boldsymbol{r}_1')\delta(\boldsymbol{r}_2 - \boldsymbol{r}_2')v(\boldsymbol{r}_1, \boldsymbol{r}_2) \tag{4.7}$$

while the screened Coulomb interaction takes of the form

$$\Xi_w(\boldsymbol{r}_1, \boldsymbol{r}_2, \boldsymbol{r}_1', \boldsymbol{r}_2') = -\delta(\boldsymbol{r}_1 - \boldsymbol{r}_2')\delta(\boldsymbol{r}_1' - \boldsymbol{r}_2)W(\boldsymbol{r}_1, \boldsymbol{r}_2). \tag{4.8}$$

The solution of the integral equation (4.2) is thus mapped to the linear algebra problem

$$\boldsymbol{\chi} = \left[\chi_0^{-1}(\omega) - \Xi\right]^{-1}. \tag{4.9}$$

4.2. BSE for crystalline systems

In a crystalline system, χ follows the periodicity of the lattice

$$\chi(\boldsymbol{r}_1 + \boldsymbol{R}, \boldsymbol{r}_2 + \boldsymbol{R}, \boldsymbol{r}_1' + \boldsymbol{R}, \boldsymbol{r}_2' + \boldsymbol{R}, \omega) = \chi(\boldsymbol{r}_1, \boldsymbol{r}_2, \boldsymbol{r}_1', \boldsymbol{r}_2', \omega) \tag{4.10}$$

and can be expressed in terms of a sum of functions defined for each point in the Brillouin zone [19]

$$\chi(\boldsymbol{r}_1, \boldsymbol{r}_2, \boldsymbol{r}_1', \boldsymbol{r}_2', \omega) = \sum_{\boldsymbol{q}_\mathrm{mt} \in \mathrm{B.z.}} \chi_{\boldsymbol{q}_\mathrm{mt}}(\boldsymbol{r}_1, \boldsymbol{r}_2, \boldsymbol{r}_1', \boldsymbol{r}_2', \omega). \tag{4.11}$$

Since the one-particle wave functions are Bloch functions, also the two-particle basis functions can be chosen to be Bloch-periodic in $\boldsymbol{q}_\mathrm{mt}$. We define the resonant and anti-resonant basis functions as

$$\Upsilon^{\mathrm{r}}_{\alpha,\boldsymbol{q}_\mathrm{mt}}(\boldsymbol{r}, \boldsymbol{r}') = \psi_{o_\alpha \boldsymbol{k}_\alpha + \boldsymbol{q}_\mathrm{mt}/2}(\boldsymbol{r})\psi^*_{u_\alpha \boldsymbol{k}_\alpha - \boldsymbol{q}_\mathrm{mt}/2}(\boldsymbol{r}') \tag{4.12a}$$

and

$$\Upsilon^{\mathrm{a}}_{\alpha,\boldsymbol{q}_\mathrm{mt}}(\boldsymbol{r}, \boldsymbol{r}') = \psi_{u_\alpha \boldsymbol{k}_\alpha + \boldsymbol{q}_\mathrm{mt}/2}(\boldsymbol{r})\psi^*_{o_\alpha \boldsymbol{k}_\alpha - \boldsymbol{q}_\mathrm{mt}/2}(\boldsymbol{r}'). \tag{4.12b}$$

It is now possible to solve eq. (4.5) for each $\boldsymbol{q}_\mathrm{mt}$ component separately by restricting the two-particle basis according to eq. (4.12), i.e.

$$\boldsymbol{\chi}(\boldsymbol{q}_\mathrm{mt}, \omega) = \left[\boldsymbol{\chi}_0^{-1}(\boldsymbol{q}_\mathrm{mt}, \omega) - \Xi(\boldsymbol{q}_\mathrm{mt})\right]^{-1}. \tag{4.13}$$

In the following we approximate the quasi-particle states $\psi_{i,\boldsymbol{k}}$ with the Kohn-Sham orbitals $\phi_{i,\boldsymbol{k}}$. For diamond, Si, Ge, and LiCl this is known to be a good approximation [31]. Changing the enumeration of the $\boldsymbol{k}$ points in the definition of the anti-resonant part of the two-particle basis according to

$$\Upsilon^{\bar{\mathrm{a}}}_{\alpha,\boldsymbol{q}_{\mathrm{mt}}}(\boldsymbol{r},\boldsymbol{r}') = \phi_{u_\alpha-\boldsymbol{k}_\alpha+\boldsymbol{q}_{\mathrm{mt}}/2}(\boldsymbol{r}),\phi^*_{o_\alpha-\boldsymbol{k}_\alpha-\boldsymbol{q}_{\mathrm{mt}}/2}(\boldsymbol{r}') \tag{4.14}$$

is useful when considering the symmetry properties of the Bloch states under time-reversal

$$\phi_{\boldsymbol{k}} = \phi^*_{-\boldsymbol{k}} \quad \text{and} \quad \varepsilon_{\boldsymbol{k}} = \varepsilon_{-\boldsymbol{k}} \tag{4.15}$$

(see Appendix A.3.2). In this way, there is a direct connection between the resonant and anti-resonant basis functions [9]

$$\begin{aligned}\Upsilon^{\bar{\mathrm{a}}}_{\alpha,\boldsymbol{q}_{\mathrm{mt}}}(\boldsymbol{r},\boldsymbol{r}') &= \phi_{u_\alpha-\boldsymbol{k}_\alpha+\boldsymbol{q}_{\mathrm{mt}}/2}(\boldsymbol{r})\phi^*_{o_\alpha-\boldsymbol{k}_\alpha-\boldsymbol{q}_{\mathrm{mt}}/2}(\boldsymbol{r}') \\ &= \phi_{o_\alpha\boldsymbol{k}_\alpha+\boldsymbol{q}_{\mathrm{mt}}/2}(\boldsymbol{r}')\phi^*_{u_\alpha\boldsymbol{k}_\alpha-\boldsymbol{q}_{\mathrm{mt}}/2}(\boldsymbol{r}) = \Upsilon^{\mathrm{r}}_{\alpha,\boldsymbol{q}_{\mathrm{mt}}}(\boldsymbol{r}',\boldsymbol{r}).\end{aligned} \tag{4.16}$$

4.3. Matrix elements

In this section, the explicit form of the matrix elements needed for $\chi(\boldsymbol{q}_{\mathrm{mt}},\omega)$ (4.13) in the two-particle Bloch basis functions are given. The calculation of those matrix elements in `exciting` will be discussed in chapter 5. The matrix representation of an operator $\hat{\mathrm{O}}$ has the block structure

$$\mathbf{O} = \begin{pmatrix} \mathbf{O}^{\mathrm{rr}} & \mathbf{O}^{\mathrm{ra}} \\ \mathbf{O}^{\mathrm{ar}} & \mathbf{O}^{\mathrm{aa}} \end{pmatrix}, \tag{4.17}$$

where the superscripts corresponds to the subspaces. In the following, we also adapt the notational convention for matrix elements in terms of the single-particle states

$$\langle m,n|\hat{\mathrm{O}}|i,j\rangle = \iint \phi^*_m(\boldsymbol{r})\phi^*_n(\boldsymbol{r}')O(\boldsymbol{r},\boldsymbol{r}')\phi_i(\boldsymbol{r})\phi_j(\boldsymbol{r}')\,\mathrm{d}^3r\,\mathrm{d}^3r' \,. \tag{4.18}$$

To shorten the notation in the following we write

$$\boldsymbol{k}_+ = \boldsymbol{k} + \boldsymbol{q}_{\mathrm{mt}}/2 \quad \text{and} \quad \boldsymbol{k}_- = \boldsymbol{k} - \boldsymbol{q}_{\mathrm{mt}}/2. \tag{4.19}$$

4.3.1. Independent-particle polarization function

The matrix elements of χ_0 are straightforwardly computed using eq. (4.3) and eq. (4.6). In the subsequent discussion, we will drop the infinitesimal δ which will eventually be re-introduced in the final expression for the dielectric function. It is

$$\boldsymbol{\chi}_0^{-1}(\boldsymbol{q}_{\mathrm{mt}},\omega) = -\left[\begin{pmatrix} \mathbf{E}^{\mathrm{ip}}(\boldsymbol{q}_{\mathrm{mt}}) & 0 \\ 0 & \mathbf{E}^{\mathrm{ip}}(-\boldsymbol{q}_{\mathrm{mt}}) \end{pmatrix} - \omega\begin{pmatrix} \mathbb{1} & 0 \\ 0 & -\mathbb{1} \end{pmatrix}\right] \tag{4.20}$$

with the independent-particle transition energies as matrix elements (note that $\boldsymbol{k}_\pm$ implicit depends on $\boldsymbol{q}_{\mathrm{mt}}$)

$$E^{\mathrm{ip}}_{\alpha,\alpha'}(\boldsymbol{q}_{\mathrm{mt}}) = \left(\varepsilon_{u,\boldsymbol{k}_-} - \varepsilon_{o,\boldsymbol{k}_+}\right)\delta_{\alpha,\alpha'}. \tag{4.21}$$

Changing both k-summation variables from $\boldsymbol{k}$ to $-\boldsymbol{k}$ in the anti-resonant part of χ_0 and using the time-reversal symmetry (4.15) allows us to write

$$\sum_{o,u,\boldsymbol{k},\boldsymbol{k}'} \frac{\psi_{u,\boldsymbol{k}'}(\boldsymbol{r}_1)\psi^*_{o,\boldsymbol{k}}(\boldsymbol{r}_1')\psi^*_{u,\boldsymbol{k}'}(\boldsymbol{r}_2')\psi_{o,\boldsymbol{k}}(\boldsymbol{r}_2)}{-\omega-(\varepsilon_{u,\boldsymbol{k}'}-\varepsilon_{o,\boldsymbol{k}})+\mathrm{i}\delta} = \sum_{o,u,\boldsymbol{k},\boldsymbol{k}'} \frac{\psi^*_{u,\boldsymbol{k}'}(\boldsymbol{r}_1)\psi_{o,\boldsymbol{k}}(\boldsymbol{r}_1')\psi_{u,\boldsymbol{k}'}(\boldsymbol{r}_2')\psi^*_{o,\boldsymbol{k}}(\boldsymbol{r}_2)}{-\omega-(\varepsilon_{u,\boldsymbol{k}'}-\varepsilon_{o,\boldsymbol{k}})+\mathrm{i}\delta} \tag{4.22}$$

from which follows that $\boldsymbol{\chi}_0^{-1}$ can be written in the anti-resonant basis choice of eq. (4.16) as

$$\boldsymbol{\chi}_0^{-1}(\boldsymbol{q}_{\mathrm{mt}},\omega) = -\left[\begin{pmatrix}\mathbf{E}^{\mathrm{ip}}(\boldsymbol{q}_{\mathrm{mt}}) & 0\\ 0 & \mathbf{E}^{\mathrm{ip}}(\boldsymbol{q}_{\mathrm{mt}})\end{pmatrix} - \omega\begin{pmatrix}\mathbb{1} & 0\\ 0 & -\mathbb{1}\end{pmatrix}\right]. \tag{4.23}$$

Partial occupations

To account for partial occupation numbers of the Kohn-Sham system, we introduce the diagonal matrix of occupation number difference as

$$\mathbf{F}_{\alpha,\alpha'}(\boldsymbol{q}_{\mathrm{mt}}) = \left(f_{o,\boldsymbol{k}_+} - f_{u,\boldsymbol{k}_-}\right)\delta_{\alpha,\alpha'} \tag{4.24}$$

and rewrite eq. (4.23) in view of eq. (F.5) in a symmetric fashion (omitting $\boldsymbol{q}_{\mathrm{mt}}$)

$$\boldsymbol{\chi}_0^{-1}(\boldsymbol{q}_{\mathrm{mt}},\omega) = -\left[\begin{pmatrix}\mathbf{F}^{-\frac{1}{2}}\mathbf{E}^{\mathrm{ip}}\mathbf{F}^{-\frac{1}{2}} & 0\\ 0 & \mathbf{F}^{-\frac{1}{2}}\mathbf{E}^{\mathrm{ip}}\mathbf{F}^{-\frac{1}{2}}\end{pmatrix} - \omega\begin{pmatrix}\mathbb{1} & 0\\ 0 & -\mathbb{1}\end{pmatrix}\right]. \tag{4.25}$$

It is apparent, that this is an approximate approach and only possible as long as there is no occupation inversion.

4.3.2. Exchange interaction matrix elements

The calculation of the matrix elements of the Coulomb potential using eqs. (4.6) and (4.7) reduces to

$$V_{ij}(\boldsymbol{q}_{\mathrm{mt}}) = \iint \Upsilon^*_{i,\boldsymbol{q}_{\mathrm{mt}}}(\boldsymbol{r},\boldsymbol{r})v(\boldsymbol{r},\boldsymbol{r}')\Upsilon_{j,\boldsymbol{q}_{\mathrm{mt}}}(\boldsymbol{r}',\boldsymbol{r}')\,\mathrm{d}^3r\,\mathrm{d}^3r'\,. \tag{4.26}$$

The Coulomb potential is symmetrical in $\boldsymbol{r}$ and $\boldsymbol{r}'$ and obeys the lattice periodicity, i.e.

$$v(\boldsymbol{r},\boldsymbol{r}') = v(\boldsymbol{r}',\boldsymbol{r}) = v(\left|\boldsymbol{r}'-\boldsymbol{r}\right|) \quad \text{and} \quad v(\boldsymbol{r}+\boldsymbol{R},\boldsymbol{r}'+\boldsymbol{R}) = v(\boldsymbol{r},\boldsymbol{r}'). \tag{4.27}$$

Choosing the basis according to eq. (4.12), the elements of the four blocks are computed according to

$$\begin{aligned} V^{\mathrm{rr}}_{\alpha\alpha'}(\boldsymbol{q}_{\mathrm{mt}}) &= \left\langle o\boldsymbol{k}_+, u'\boldsymbol{k}'_- \middle| v(\boldsymbol{r},\boldsymbol{r}') \middle| u\boldsymbol{k}_-, o'\boldsymbol{k}'_+ \right\rangle \\ &\overset{(4.27)}{=} \left\langle u'\boldsymbol{k}'_-, o\boldsymbol{k}_+ \middle| v(\boldsymbol{r},\boldsymbol{r}') \middle| o'\boldsymbol{k}'_+, u\boldsymbol{k}_- \right\rangle \end{aligned} \tag{4.28a}$$

$$V^{\mathrm{aa}}_{\alpha\alpha'}(\boldsymbol{q}_{\mathrm{mt}}) = \left\langle u\boldsymbol{k}_+, o'\boldsymbol{k}'_- \middle| v(\boldsymbol{r},\boldsymbol{r}') \middle| o\boldsymbol{k}_-, u'\boldsymbol{k}'_+ \right\rangle \tag{4.28b}$$

$$V^{\mathrm{ra}}_{\alpha\alpha'}(\boldsymbol{q}_{\mathrm{mt}}) = \left\langle o\boldsymbol{k}_+, o'\boldsymbol{k}'_- \middle| v(\boldsymbol{r},\boldsymbol{r}') \middle| u\boldsymbol{k}_-, u'\boldsymbol{k}'_+ \right\rangle \tag{4.28c}$$

$$V^{\mathrm{ar}}_{\alpha\alpha'}(\boldsymbol{q}_{\mathrm{mt}}) = \left\langle u\boldsymbol{k}_+, u'\boldsymbol{k}'_- \middle| v(\boldsymbol{r},\boldsymbol{r}') \middle| o\boldsymbol{k}_-, o'\boldsymbol{k}'_+ \right\rangle . \tag{4.28d}$$

The rr-block elements correspond to the diagram 3.1.a, while the ra-block elements are depicted in the diagram 3.1.c. These four blocks become all equal when the basis functions of eq. (4.16) are used instead and the time-reversal symmetry is employed. This follows directly from eq. (4.16) and eq. (4.26). Consequently, only the resonant-resonant block of the exchange interaction matrix needs to be computed.

For further calculations, it is useful to use the lattice Fourier representation of the Coulomb potential v

$$v(\boldsymbol{r},\boldsymbol{r}') = \frac{1}{V}\sum_{\boldsymbol{G}}\sum_{\boldsymbol{q}\in \mathrm{B.z}} \frac{4\pi}{|\boldsymbol{G}+\boldsymbol{q}|} \mathrm{e}^{\mathrm{i}(\boldsymbol{G}+\boldsymbol{q})(\boldsymbol{r}-\boldsymbol{r}')} \tag{4.29}$$

and the plane-wave matrix elements M (see appendix D)

$$\left\langle f\boldsymbol{k}_f \middle| \mathrm{e}^{-\mathrm{i}(\boldsymbol{G}+\boldsymbol{q})\boldsymbol{r}} \middle| i\boldsymbol{k}_i \right\rangle = \delta_{\left\lfloor \boldsymbol{k}_f-\boldsymbol{k}_i+\boldsymbol{q}\right\rceil_{1^{\mathrm{st}}\,\mathrm{BZ}},0} M_{f i\boldsymbol{k}_f}(\boldsymbol{G},\boldsymbol{q}), \tag{4.30}$$

where the Kronecker-delta ensures the conservation of crystal momentum. Then, the matrix elements (4.28a) take on the form

$$\begin{aligned} V^{\mathrm{rr}}_{\alpha\alpha'}(\boldsymbol{q}_{\mathrm{mt}}) = \frac{1}{V}\sum_{\boldsymbol{G}}\sum_{\boldsymbol{q}} & v(\boldsymbol{G},\boldsymbol{q}) \\ & \times \left\langle u\boldsymbol{k}_- \middle| \mathrm{e}^{-\mathrm{i}(\boldsymbol{G}+\boldsymbol{q})\boldsymbol{r}} \middle| o\boldsymbol{k}_+ \right\rangle^* \left\langle u'\boldsymbol{k}'_- \middle| \mathrm{e}^{-\mathrm{i}(\boldsymbol{G}+\boldsymbol{q})\boldsymbol{r}'} \middle| o'\boldsymbol{k}'_+ \right\rangle \\ & = \frac{1}{V}\sum_{\boldsymbol{G}} v(\boldsymbol{G},\boldsymbol{q}_{\mathrm{mt}}) M^*_{uo\boldsymbol{k}_-}(\boldsymbol{G},\boldsymbol{q}_{\mathrm{mt}}) M_{u'o'\boldsymbol{k}'_-}(\boldsymbol{G},\boldsymbol{q}_{\mathrm{mt}}). \end{aligned} \tag{4.31}$$

4.3.3. Screened Coulomb interaction

The matrix elements of the screened Coulomb interaction are computed with

$$W_{ij}(\boldsymbol{q}_{\mathrm{mt}}) = \iint \Upsilon^*_{i,\boldsymbol{q}_{\mathrm{mt}}}(\boldsymbol{r},\boldsymbol{r}') W(\boldsymbol{r},\boldsymbol{r}') \Upsilon_{j,\boldsymbol{q}_{\mathrm{mt}}}(\boldsymbol{r},\boldsymbol{r}') \,\mathrm{d}^3r\,\mathrm{d}^3r' , \tag{4.32}$$

where W is the statically screened Coulomb potential [see (3.16) and (3.28)]

$$W(\boldsymbol{r},\boldsymbol{r}') = \int v(\boldsymbol{r},\boldsymbol{r}'')\varepsilon^{-1}(\boldsymbol{r}'',\boldsymbol{r}')\,\mathrm{d}^3r'' . \tag{4.33}$$

For a crystalline system, we assume that W is real-valued and that

$$W(\boldsymbol{r},\boldsymbol{r}') = W(\boldsymbol{r}',\boldsymbol{r}) \quad \text{and} \quad W(\boldsymbol{r}+\boldsymbol{R},\boldsymbol{r}'+\boldsymbol{R}) = W(\boldsymbol{r},\boldsymbol{r}') \tag{4.34}$$

hold. Then, in the basis (4.12), the four blocks are given by

$$\begin{aligned} W^{\mathrm{rr}}_{\alpha\alpha'}(\boldsymbol{q}_{\mathrm{mt}}) &= \left\langle o\boldsymbol{k}_+, u'\boldsymbol{k}'_- \middle| W(\boldsymbol{r},\boldsymbol{r}') \middle| o'\boldsymbol{k}'_+, u\boldsymbol{k}_- \right\rangle \\ &\overset{(4.34)}{=} \left\langle u'\boldsymbol{k}'_-, o\boldsymbol{k}_+ \middle| W(\boldsymbol{r},\boldsymbol{r}') \middle| u\boldsymbol{k}_-, o'\boldsymbol{k}'_+ \right\rangle \end{aligned} \tag{4.35a}$$

$$W^{\mathrm{aa}}_{\alpha\alpha'}(\boldsymbol{q}_{\mathrm{mt}}) = \left\langle u\boldsymbol{k}_+, o'\boldsymbol{k}'_- \middle| W(\boldsymbol{r},\boldsymbol{r}') \middle| u'\boldsymbol{k}'_+, o\boldsymbol{k}_- \right\rangle \tag{4.35b}$$

$$W^{\mathrm{ra}}_{\alpha\alpha'}(\boldsymbol{q}_{\mathrm{mt}}) = \left\langle o\boldsymbol{k}_+, o'\boldsymbol{k}'_- \middle| W(\boldsymbol{r},\boldsymbol{r}') \middle| u'\boldsymbol{k}'_+, u\boldsymbol{k}_- \right\rangle \tag{4.35c}$$

$$W^{\mathrm{ar}}_{\alpha\alpha'}(\boldsymbol{q}_{\mathrm{mt}}) = \left\langle u\boldsymbol{k}_+, u'\boldsymbol{k}'_- \middle| W(\boldsymbol{r},\boldsymbol{r}') \middle| o'\boldsymbol{k}'_+, o\boldsymbol{k}_- \right\rangle . \tag{4.35d}$$

For the case of zero-momentum transfer, $\boldsymbol{q}_{\mathrm{mt}} = 0$, these blocks are related according to

$$\mathbf{W}^{\mathrm{rr}} = \left(\mathbf{W}^{\mathrm{rr}}\right)^\dagger = \left(\mathbf{W}^{\mathrm{aa}}\right)^* \quad \text{and} \quad \mathbf{W}^{\mathrm{ra}} = \left(\mathbf{W}^{\mathrm{ra}}\right)^{\mathrm{T}} = \left(\mathbf{W}^{\mathrm{ar}}\right)^* . \tag{4.36}$$

For finite momentum transfer these relations do not hold anymore and four distinct blocks are left.

Again, this can be remedied by switching to the basis defined in eq. (4.16) and using the time-reversal symmetry. From eqs. (4.16), (4.32) and (4.34) it follows directly that there are only two distinct blocks, because

$$\mathbf{W}^{\mathrm{rr}} = \mathbf{W}^{\bar{\mathrm{a}}\bar{\mathrm{a}}} = \left(\mathbf{W}^{\mathrm{rr}}\right)^\dagger \quad \text{and} \quad \mathbf{W}^{\mathrm{r}\bar{\mathrm{a}}} = \mathbf{W}^{\bar{\mathrm{a}}\mathrm{r}} = \left(\mathbf{W}^{\mathrm{r}\bar{\mathrm{a}}}\right)^\dagger . \tag{4.37}$$

This result also holds for finite momentum transfer. In terms of the single particle states the elements of $\mathbf{W}^{\mathrm{r}\bar{\mathrm{a}}}$ are calculated according to

$$\begin{aligned}
W^{\mathrm{r}\bar{\mathrm{a}}}_{\alpha\alpha'}(\boldsymbol{q}_{\mathrm{mt}}) &= \iint \Upsilon^{\mathrm{r}*}_{\alpha}(\boldsymbol{r},\boldsymbol{r}') W(\boldsymbol{r},\boldsymbol{r}') \Upsilon^{\mathrm{r}}_{\alpha'}(\boldsymbol{r}',\boldsymbol{r}) \\
&= \iint \phi^*_{o\boldsymbol{k}_+}(\boldsymbol{r}) \phi_{u\boldsymbol{k}_-}(\boldsymbol{r}') W(\boldsymbol{r},\boldsymbol{r}') \phi_{o'\boldsymbol{k}'_+}(\boldsymbol{r}') \phi^*_{u'\boldsymbol{k}_-}(\boldsymbol{r}) \,\mathrm{d}^3r \,\mathrm{d}^3r' \\
&= \iint \phi^*_{o\boldsymbol{k}_+}(\boldsymbol{r}) \phi_{o'\boldsymbol{k}'_+}(\boldsymbol{r}') W(\boldsymbol{r},\boldsymbol{r}') \phi^*_{u'\boldsymbol{k}_-}(\boldsymbol{r}) \phi_{u\boldsymbol{k}_-}(\boldsymbol{r}') \,\mathrm{d}^3r \,\mathrm{d}^3r' \\
&\coloneqq \left\langle o\boldsymbol{k}_+, (o'\boldsymbol{k}'_+)^* \middle| W(\boldsymbol{r},\boldsymbol{r}') \middle| (u'\boldsymbol{k}'_-)^*, u\boldsymbol{k}_- \right\rangle \\
&\overset{(4.34)}{=} \left\langle (o'\boldsymbol{k}'_+)^*, o\boldsymbol{k}_+ \middle| W(\boldsymbol{r},\boldsymbol{r}') \middle| u\boldsymbol{k}_-, (u'\boldsymbol{k}'_-)^* \right\rangle .
\end{aligned} \tag{4.38}$$

As for the exchange interaction, we use the lattice Fourier representation of $W(\boldsymbol{r},\boldsymbol{r}')$. Plugging into eq. (4.33) the Fourier representations of the Coulomb potential and of the inverse dielectric function and integrating over the doubly-primed coordinates yields

$$W(\boldsymbol{r},\boldsymbol{r}') = \frac{1}{V} \sum_{\boldsymbol{G}\boldsymbol{G}'} \sum_{\boldsymbol{q}\in \mathrm{B.z}} \mathrm{e}^{\mathrm{i}(\boldsymbol{G}+\boldsymbol{q})\boldsymbol{r}} W_{\boldsymbol{G},\boldsymbol{G}'}(\boldsymbol{q}) \,\mathrm{e}^{-\mathrm{i}(\boldsymbol{G}'+\boldsymbol{q})\boldsymbol{r}'}, \tag{4.39}$$

with the coefficients

$$W_{\boldsymbol{G},\boldsymbol{G}'}(\boldsymbol{q}) = \frac{4\pi}{|\boldsymbol{G}+\boldsymbol{q}|^2} \varepsilon^{-1}_{\boldsymbol{G}\boldsymbol{G}'}(\boldsymbol{q},\omega=0). \tag{4.40}$$

The appearance of ε, which is our target quantity, in the setup of the screened interaction signals that, in theory, the BSE needs to be solved self-consistently starting from some approximation to ε. In practice, however, the microscopic dielectric matrix in the independent particle approximation $\varepsilon^0_{\boldsymbol{G}\boldsymbol{G}'}(\boldsymbol{q},\omega=0)$ is used for a one-shot BSE calculation. For

the construction of ε^0 the retarded polarizability (see section 2.2) P is calculated for the Kohn-Sham system and the exchange-correlation kernel is neglected (see appendix E).

The resonant-resonant-block of W eq. (4.35a) can then be stated in terms of the plane-wave matrix elements (4.30) as

$$\begin{aligned} W^{\mathrm{rr}}_{\alpha\alpha'}(\boldsymbol{q}_{\mathrm{mt}}) &= \frac{1}{V}\sum_{\boldsymbol{G}\boldsymbol{G}'}\sum_{\boldsymbol{q}} W_{\boldsymbol{G}\boldsymbol{G}'}(\boldsymbol{q}) \left\langle o'\boldsymbol{k}'_+\middle|\mathrm{e}^{-\mathrm{i}(\boldsymbol{G}+\boldsymbol{q})\boldsymbol{r}}\middle|o\boldsymbol{k}_+\right\rangle^* \left\langle u'\boldsymbol{k}'_-\middle|\mathrm{e}^{-\mathrm{i}(\boldsymbol{G}'+\boldsymbol{q})\boldsymbol{r}'}\middle|u\boldsymbol{k}_-\right\rangle \\ &= \frac{1}{V}\sum_{\boldsymbol{G}\boldsymbol{G}'} W_{\boldsymbol{G}\boldsymbol{G}'}(\boldsymbol{k}-\boldsymbol{k}') M^*_{o'o\boldsymbol{k}'_+}(\boldsymbol{G},\boldsymbol{k}-\boldsymbol{k}') M_{u'u\boldsymbol{k}'_-}(\boldsymbol{G}',\boldsymbol{k}-\boldsymbol{k}') \\ &\overset{(4.34)}{=} \frac{1}{V}\sum_{\boldsymbol{G}\boldsymbol{G}'} W_{\boldsymbol{G}\boldsymbol{G}'}(\boldsymbol{k}'-\boldsymbol{k}) M^*_{uu'\boldsymbol{k}_-}(\boldsymbol{G},\boldsymbol{k}'-\boldsymbol{k}) M_{oo'\boldsymbol{k}_+}(\boldsymbol{G}',\boldsymbol{k}'-\boldsymbol{k}), \end{aligned} \tag{4.41}$$

while the coupling block eq. (4.38) takes on the form of

$$\begin{aligned} W^{\mathrm{r\bar{a}}}_{\alpha\alpha'}(\boldsymbol{q}_{\mathrm{mt}}) &= \frac{1}{V}\sum_{\boldsymbol{G}\boldsymbol{G}'}\sum_{\boldsymbol{q}} W_{\boldsymbol{G}\boldsymbol{G}'}(\boldsymbol{q}) \left\langle u\boldsymbol{k}_-\middle|\mathrm{e}^{-\mathrm{i}(\boldsymbol{G}+\boldsymbol{q})\boldsymbol{r}}\middle|(o'\boldsymbol{k}'_+)^*\right\rangle^* \left\langle o\boldsymbol{k}_+\middle|\mathrm{e}^{-\mathrm{i}(\boldsymbol{G}'+\boldsymbol{q})\boldsymbol{r}'}\middle|(u'\boldsymbol{k}'_-)^*\right\rangle \\ &= \frac{1}{V}\sum_{\boldsymbol{G}\boldsymbol{G}'} W_{\boldsymbol{G}\boldsymbol{G}'}(-\boldsymbol{k}'-\boldsymbol{k}) N^*_{uo'\boldsymbol{k}_-}(\boldsymbol{G},-\boldsymbol{k}'-\boldsymbol{k}) N_{ou'\boldsymbol{k}_+}(\boldsymbol{G}',-\boldsymbol{k}'-\boldsymbol{k}), \end{aligned} \tag{4.42}$$

where we used the symmetry again and introduced the modified plane wave matrix elements N

$$\left\langle f\boldsymbol{k}_f\middle|\mathrm{e}^{-\mathrm{i}(\boldsymbol{G}+\boldsymbol{q})\boldsymbol{r}}\middle|(i\boldsymbol{k}_i)^*\right\rangle =: \delta_{\lfloor \boldsymbol{k}_f+\boldsymbol{k}_i+\boldsymbol{q}\rfloor_{1^{\mathrm{st}}\mathrm{BZ}},0}\, N_{fi\boldsymbol{k}_f}(\boldsymbol{G},\boldsymbol{q}). \tag{4.43}$$

They are related to the plane-wave matix elments M due to the time-reversal symmetry

$$\left\langle f\boldsymbol{k}_f\middle|\mathrm{e}^{-\mathrm{i}(\boldsymbol{G}+\boldsymbol{q})\boldsymbol{r}}\middle|(i\boldsymbol{k}_i)^*\right\rangle = \left\langle f\boldsymbol{k}_f\middle|\mathrm{e}^{-\mathrm{i}(\boldsymbol{G}+\boldsymbol{q})\boldsymbol{r}}\middle|i-\boldsymbol{k}_i\right\rangle. \tag{4.44}$$

The advantage of calculating the Ns directly, is that we do not need to calculated the $|-\boldsymbol{k}_i\rangle$ eigenstates and that we fix the phase between $|-\boldsymbol{k}\rangle$ and $(|\boldsymbol{k}\rangle)^*$ implicitly to 1.

4.4. BSE as an eigenvalue problem

With the results of 4.3 we can write eq. (4.13) as

$$\boldsymbol{\chi}(\boldsymbol{q}_{\mathrm{mt}},\omega) = -\mathbf{F}^{\frac{1}{2}}(\boldsymbol{q}_{\mathrm{mt}})\left[\mathbf{H}^{\mathrm{e}}(\boldsymbol{q}_{\mathrm{mt}}) - \omega\boldsymbol{\Delta}\right]^{-1}\mathbf{F}^{\frac{1}{2}}(\boldsymbol{q}_{\mathrm{mt}}), \tag{4.45}$$

where we introduce the effective two-particle Hamiltonian $\mathbf{H}^{\mathrm{e}}$,

$$\boldsymbol{\Delta} = \begin{pmatrix} \mathbb{1} & 0 \\ 0 & -\mathbb{1} \end{pmatrix} \quad \text{and redefine} \quad \mathbf{F}^{\frac{1}{2}} = \begin{pmatrix} \mathbf{F}^{\frac{1}{2}} & 0 \\ 0 & \mathbf{F}^{\frac{1}{2}} \end{pmatrix}. \tag{4.46}$$

Using time-reversal symmetry as discussed above, the Hamiltonian is hermitian and takes on the form

$$\mathbf{H}^{\mathrm{e}}(\boldsymbol{q}_{\mathrm{mt}}) = \mathbf{F}^{\frac{1}{2}}(\boldsymbol{q}_{\mathrm{mt}}) \begin{pmatrix} \mathbf{A}(\boldsymbol{q}_{\mathrm{mt}}) & \mathbf{B}(\boldsymbol{q}_{\mathrm{mt}}) \\ \mathbf{B}(\boldsymbol{q}_{\mathrm{mt}}) & \mathbf{A}(\boldsymbol{q}_{\mathrm{mt}}) \end{pmatrix} \mathbf{F}^{\frac{1}{2}}(\boldsymbol{q}_{\mathrm{mt}}). \tag{4.47}$$

The diagonal block is given by

$$\mathbf{A}(\boldsymbol{q}_{\mathrm{mt}}) = \mathbf{E}^{\mathrm{ip}}(\boldsymbol{q}_{\mathrm{mt}}) + 2\gamma_{\mathrm{x}}\mathbf{V}^{\mathrm{rr}}(\boldsymbol{q}_{\mathrm{mt}}) - \gamma_{\mathrm{c}}\mathbf{W}^{\mathrm{rr}}(\boldsymbol{q}_{\mathrm{mt}}), \tag{4.48}$$

and the coupling block by

$$\mathbf{B}(\boldsymbol{q}_{\mathrm{mt}}) = 2\gamma_{\mathrm{x}}\mathbf{V}^{\mathrm{rr}}(\boldsymbol{q}_{\mathrm{mt}}) - \gamma_{\mathrm{c}}\mathbf{W}^{\mathrm{r\bar{a}}}(\boldsymbol{q}_{\mathrm{mt}}). \tag{4.49}$$

Here, we introduce the factors γ_x and γ_{c} which allow to account for the spin degree of freedom, as discussed in Ref. [19]. Spin-singlet excitations are obtained by setting $\gamma_{\mathrm{x}} = 1$ and $\gamma_{\mathrm{c}} = 1$, and spin-triplet excitations are calculated with $\gamma_{\mathrm{x}} = 0$ and $\gamma_{\mathrm{c}} = 1$. This treatment is allowed as long as the spin-up and spin-down components of the orbitals are considered to be identical.

The resolvent (4.45) can be found using the solutions of the generalized eigenvalue problem (dropping the $\boldsymbol{q}_{\mathrm{mt}}$ for brevity)

$$\mathbf{H}^{\mathrm{e}}\begin{pmatrix}\boldsymbol{X}_\lambda\\ \boldsymbol{Y}_\lambda\end{pmatrix} = E_\lambda \boldsymbol{\Delta}\begin{pmatrix}\boldsymbol{X}_\lambda\\ \boldsymbol{Y}_\lambda\end{pmatrix}, \tag{4.50}$$

according to [34]

$$\left[\mathbf{H}^{\mathrm{e}} - \omega\boldsymbol{\Delta}\right]^{-1} = \sum_\lambda \left[\frac{1}{E_\lambda - \omega}\begin{pmatrix}\boldsymbol{X}_\lambda\\ \boldsymbol{Y}_\lambda\end{pmatrix}\begin{pmatrix}\boldsymbol{X}_\lambda\\ \boldsymbol{Y}_\lambda\end{pmatrix}^\dagger + \frac{1}{E_\lambda + \omega}\begin{pmatrix}\boldsymbol{Y}_\lambda\\ \boldsymbol{X}_\lambda\end{pmatrix}\begin{pmatrix}\boldsymbol{Y}_\lambda\\ \boldsymbol{X}_\lambda\end{pmatrix}^\dagger\right]. \tag{4.51}$$

4.4.1. Squared eigenvalue problem

The generalized eigenvalue problem eq. (4.50) can be mapped, following [9, 34], onto an auxiliary "squared" EVP of half its size, given by

$$\mathbf{S} = (\mathbf{A} - \mathbf{B})^{\frac{1}{2}}\,(\mathbf{A} + \mathbf{B})\,(\mathbf{A} - \mathbf{B})^{\frac{1}{2}} \tag{4.52a}$$

and

$$\mathbf{S}\boldsymbol{Z}_\lambda = W_\lambda \boldsymbol{Z}_\lambda. \tag{4.52b}$$

As long as $\mathbf{A} - \mathbf{B}$ and $\mathbf{A} + \mathbf{B}$ are positive definite, the solutions of eq. (4.50) are exactly given by

$$E_\lambda = \sqrt{W_\lambda}, \tag{4.53a}$$

$$\left(\boldsymbol{X}_\lambda + \boldsymbol{Y}_\lambda\right) = (\mathbf{A} - \mathbf{B})^{\frac{1}{2}}\,\frac{1}{\sqrt{E_\lambda}}\boldsymbol{Z}_\lambda, \tag{4.53b}$$

and

$$\left(\boldsymbol{X}_\lambda - \boldsymbol{Y}_\lambda\right) = (\mathbf{A} - \mathbf{B})^{\frac{1}{2}}\,\sqrt{E_\lambda}\boldsymbol{Z}_\lambda. \tag{4.53c}$$

Using the shorthand notation

$$\mathbf{C} = (\mathbf{A} - \mathbf{B})^{\frac{1}{2}} \tag{4.54}$$

and the scaling factors

$$E_\lambda^\pm = \frac{1}{\sqrt{E_\lambda}} \pm \sqrt{E_\lambda}, \tag{4.55}$$

we can write

$$\begin{pmatrix} \boldsymbol{X}_\lambda \\ \boldsymbol{Y}_\lambda \end{pmatrix} = \frac{1}{2} \begin{pmatrix} \mathbf{C} E_\lambda^+ \boldsymbol{Z}_\lambda \\ \mathbf{C} E_\lambda^- \boldsymbol{Z}_\lambda \end{pmatrix}. \tag{4.56}$$

4.5. Density correlation function

The time-ordered density correlation function $\chi(\boldsymbol{r}, \boldsymbol{r}', \omega)$ can now be calculated using the matrix elements χ_{ij} and the basis functions according to

$$\chi(\boldsymbol{r}, \boldsymbol{r}', \omega) = \chi(\boldsymbol{r}, \boldsymbol{r}', \boldsymbol{r}, \boldsymbol{r}', \omega) = \sum_{ij} \Upsilon_i(\boldsymbol{r}, \boldsymbol{r}) \chi_{ij}(\omega) \Upsilon_j^*(\boldsymbol{r}', \boldsymbol{r}'). \tag{4.57}$$

A subsequent Fourier transform yields the form (2.37)

$$\begin{aligned} \chi_{\boldsymbol{G}\boldsymbol{G}'}(\boldsymbol{q}_{\mathrm{mt}}, \omega) &= \frac{1}{V} \iint \mathrm{e}^{-\mathrm{i}(\boldsymbol{G}+\boldsymbol{q}_{\mathrm{mt}})\boldsymbol{r}} \chi(\boldsymbol{r}, \boldsymbol{r}', \omega) \mathrm{e}^{\mathrm{i}(\boldsymbol{G}'+\boldsymbol{q}_{\mathrm{mt}})\boldsymbol{r}'} \, \mathrm{d}^3 r \, \mathrm{d}^3 r' \\ &= \frac{1}{V} \sum_{ij} \left(\int \Upsilon_i(\boldsymbol{r}, \boldsymbol{r}) \mathrm{e}^{-\mathrm{i}(\boldsymbol{G}+\boldsymbol{q}_{\mathrm{mt}})\boldsymbol{r}} \mathrm{d}^3 r \right) \chi_{ij}(\omega) \left(\int \Upsilon_j(\boldsymbol{r}', \boldsymbol{r}') \mathrm{e}^{-\mathrm{i}(\boldsymbol{G}'+\boldsymbol{q}_{\mathrm{mt}})\boldsymbol{r}'} \, \mathrm{d}^3 r' \right)^* \\ &= \frac{1}{V} \sum_{ij} M_i(\boldsymbol{G}, \boldsymbol{q}_{\mathrm{mt}}) \chi_{ij}(\omega) M_j^*(\boldsymbol{G}', \boldsymbol{q}_{\mathrm{mt}}). \end{aligned} \tag{4.58}$$

Here, the plane-wave matrix elements M ensure that only basis functions with the Bloch periodicity $\boldsymbol{q}_{\mathrm{mt}}$ are needed. For the resonant basis functions, the associated plane-wave elements are

$$M_\alpha^{\mathrm{r}}(\boldsymbol{G}, \boldsymbol{q}_{\mathrm{mt}}) = \int \Upsilon_{\alpha,\boldsymbol{q}}^{\mathrm{r}}(\boldsymbol{r}, \boldsymbol{r}) \mathrm{e}^{-\mathrm{i}(\boldsymbol{G}+\boldsymbol{q}_{\mathrm{mt}})\boldsymbol{r}} \mathrm{d}^3 r = \delta_{\boldsymbol{q}_{\mathrm{mt}},\boldsymbol{q}} M_{uo\boldsymbol{k}\_}(\boldsymbol{G}, \boldsymbol{q}_{\mathrm{mt}}) \tag{4.59}$$

that are equal to the anti-resonant ones when the time-reversal symmetry is used. In view of eq. (4.45) we also absorb the occupation factors into the projecting plane wave elements

$$\tilde{\boldsymbol{M}}(\boldsymbol{G}, \boldsymbol{q}_{\mathrm{mt}}) = \mathbf{F}^{\frac{1}{2}} \boldsymbol{M}^{\mathrm{r}}(\boldsymbol{G}, \boldsymbol{q}_{\mathrm{mt}}) \tag{4.60}$$

so that

$$\chi_{\boldsymbol{G}\boldsymbol{G}'}(\boldsymbol{q}_{\mathrm{mt}}, \omega) = -\frac{1}{V} \sum_{ij} \tilde{M}_i(\boldsymbol{G}, \boldsymbol{q}_{\mathrm{mt}}) \left[\mathbf{H}^{\mathrm{e}} - \omega \boldsymbol{\Delta} \right]_{ij}^{-1} \tilde{M}_j^*(\boldsymbol{G}', \boldsymbol{q}_{\mathrm{mt}}). \tag{4.61}$$

Combining the expressions of eq. (4.58) and of the matrix $\boldsymbol{\chi}$ in terms of the eigenvectors (4.51) yields

$$\chi_{\boldsymbol{G}\boldsymbol{G}'}^{\mathrm{T}}(\boldsymbol{q}_{\mathrm{mt}}, \omega) = \sum_\lambda \left(\frac{1}{\omega - E_\lambda + \mathrm{i}\delta} + \frac{1}{-\omega - E_\lambda + \mathrm{i}\delta} \right) t_\lambda^*(\boldsymbol{G}, \boldsymbol{q}_{\mathrm{mt}}) t_\lambda(\boldsymbol{G}', \boldsymbol{q}_{\mathrm{mt}}), \tag{4.62}$$

where we have introduced the *transition coefficients* t_λ

$$t_\lambda(\boldsymbol{G}, \boldsymbol{q}_{\mathrm{mt}}) = \left(\boldsymbol{X}_\lambda + \boldsymbol{Y}_\lambda\right)^\dagger \tilde{\boldsymbol{M}}^{\mathrm{r}*}(\boldsymbol{G}, \boldsymbol{q}_{\mathrm{mt}}) = \left[\mathbf{C}\frac{1}{\sqrt{E_\lambda}}\boldsymbol{Z}_\lambda\right]^\dagger \tilde{\boldsymbol{M}}^{\mathrm{r}*}(\boldsymbol{G}, \boldsymbol{q}_{\mathrm{mt}}). \tag{4.63}$$

They constitute a sum of weighted plane wave transition matrix elements, where the weights are given by the corresponding BSE eigenvectors. In order to go over to the retarded density correlation function we need to replace $\mathrm{i}\delta$ by $-\mathrm{i}\delta$ in the second denominator of eq. (4.62) [3], leading to

$$\chi^{\mathrm{R}}_{\boldsymbol{G}\boldsymbol{G}'}(\boldsymbol{q}_{\mathrm{mt}}, \omega) = \sum_\lambda \left(\frac{1}{\omega - E_\lambda + \mathrm{i}\delta} + \frac{1}{-\omega - E_\lambda - \mathrm{i}\delta}\right) t^*_\lambda(\boldsymbol{G}, \boldsymbol{q}_{\mathrm{mt}}) t_\lambda(\boldsymbol{G}', \boldsymbol{q}_{\mathrm{mt}}). \tag{4.64}$$

Thus, the macroscopic dielectric function defined in eq. (2.41) can be expressed in terms of χ^{R} using eq. (2.37) as

$$\varepsilon_{\mathrm{M}}(\boldsymbol{Q}_{\mathrm{mt}}, \omega) = \left[1 + v_{\boldsymbol{G}_{\mathrm{mt}}}(\boldsymbol{q}_{\mathrm{mt}}) \sum_\lambda \left(\frac{1}{\omega - E_\lambda + \mathrm{i}\delta} + \frac{1}{-\omega - E_\lambda - \mathrm{i}\delta}\right) \left|t_\lambda(\boldsymbol{G}_{\mathrm{mt}}, \boldsymbol{q}_{\mathrm{mt}})\right|^2\right]^{-1}. \tag{4.65}$$

The square moduli of the transition coefficients t_λ are also referred to as *the oscillator strengths*.

4.6. The Tamm-Dancoff approximation

As already discussed in 3.3.5, a common approximation to the BSE is to zero the coupling block between the resonant and anti-resonant subspace eq. (4.47). Doing so, one is left with two decoupled eigenvalue problems for the resonant and the anti-resonant subspace, which are identical when the time-reversal symmetry is used. In this case, only the solutions of

$$\mathbf{H}^{\mathrm{e,\,TDA}} = \mathbf{F}^{\frac{1}{2}}\mathbf{A}(\boldsymbol{q}_{\mathrm{mt}})\mathbf{F}^{\frac{1}{2}}\boldsymbol{X}_\lambda = E_\lambda \boldsymbol{X}_\lambda \tag{4.66}$$

enter the expression for the transition coefficients t_λ (4.63),

$$t^{\mathrm{TDA}}_\lambda(\boldsymbol{G}_{\mathrm{mt}}, \boldsymbol{q}_{\mathrm{mt}}) = \boldsymbol{X}^\dagger_\lambda \tilde{\boldsymbol{M}}^{\mathrm{r}*}(\boldsymbol{G}_{\mathrm{mt}}, \boldsymbol{q}_{\mathrm{mt}}). \tag{4.67}$$

In [9] it is warned against the use of eq. (4.65) with the TDA, and it is suggested to use the extension of the scheme discussed in section 2.5.1 to finite momentum transfer. This is done by setting the corresponding $\boldsymbol{G}_{\mathrm{mt}}$ component of of the bare Coulomb potential to zero in the BSE setup and calculate the dielectric function according to

$$\varepsilon^{\mathrm{TDA}}_{\mathrm{M}}(\boldsymbol{Q}_{\mathrm{mt}}, \omega) = 1 - v_{\boldsymbol{G}_{\mathrm{mt}}}(\boldsymbol{q}_{\mathrm{mt}}) \sum_\lambda \left(\frac{1}{\omega - E_\lambda + \mathrm{i}\delta} + \frac{1}{-\omega - E_\lambda - \mathrm{i}\delta}\right) \left|t^{\mathrm{TDA}}_\lambda(\boldsymbol{G}_{\mathrm{mt}}, \boldsymbol{q}_{\mathrm{mt}})\right|^2. \tag{4.68}$$

In the calculations of the current work it was confirmed, that this procedure indeed yields significantly more accurate results when the TDA results are compared to the non-TDA calculations and experimental data.

4.6.1. Coupling measure

In order to assess, when the use of the TDA can be justified we first write eq. (4.50) in components:

$$\left(E_\alpha^{\mathrm{ip}} - E_\lambda\right) X_{\alpha,\lambda} + \sum_{\alpha'} \left(2\gamma_x V^{\mathrm{rr}}_{\alpha\alpha'} - \gamma_c W^{\mathrm{rr}}_{\alpha\alpha'}\right) X_{\alpha',\lambda} + \sum_{\alpha'} \left(2\gamma_x V^{\mathrm{rr}}_{\alpha\alpha'} - \gamma_c W^{\mathrm{r\bar{a}}}_{\alpha\alpha'}\right) Y_{\alpha',\lambda} = 0 \tag{4.69a}$$

$$\left(E_\alpha^{\mathrm{ip}} + E_\lambda\right) Y_{\alpha,\lambda} + \sum_{\alpha'} \left(2\gamma_x V^{\mathrm{rr}}_{\alpha\alpha'} - \gamma_c W^{\mathrm{rr}}_{\alpha\alpha'}\right) Y_{\alpha',\lambda} + \sum_{\alpha'} \left(2\gamma_x V^{\mathrm{rr}}_{\alpha\alpha'} - \gamma_c W^{\mathrm{r\bar{a}}}_{\alpha\alpha'}\right) X_{\alpha',\lambda} = 0. \tag{4.69b}$$

For the solutions with $E_\lambda > 0$, it is permissible restate eq. (4.69a) as

$$\begin{aligned} Y_{\alpha,\lambda} &= \sum_{\alpha'} \frac{\gamma_c W^{\mathrm{rr}}_{\alpha\alpha'} - 2\gamma_x V^{\mathrm{rr}}_{\alpha\alpha'}}{E_\alpha^{\mathrm{ip}} + E_\lambda} Y_{\alpha',\lambda} + \sum_{\alpha'} \frac{\gamma_c W^{\mathrm{r\bar{a}}}_{\alpha\alpha'} - 2\gamma_x V^{\mathrm{rr}}_{\alpha\alpha'}}{E_\alpha^{\mathrm{ip}} + E_\lambda} X_{\alpha',\lambda} \\ &=: \sum_{\alpha'} r^\lambda_{\alpha,\alpha'} Y_{\alpha',\lambda} + \sum_{\alpha'} a^\lambda_{\alpha,\alpha'} X_{\alpha',\lambda}, \end{aligned} \tag{4.70}$$

where we defined the resonant and anti-resonant coupling factors r^λ and a^λ, respectively. From eqs. (4.69a) and (4.70) it follows that for the TDA to be an appropriate approximation both coupling factors need to be small for all transitions and considered excitons. That is, the difference between the matrix elements of the screened and unscreened Coulomb potential must be small compared to the unperturbed energies. This condition is also discussed in [15] for the case of no screening, i.e. $W = V$. Consequently, we introduce the corresponding coupling measures

$$r_{\max} = \max_{\alpha,\alpha',\lambda} \left(\left|r^\lambda_{\alpha,\alpha'}\right|\right) \quad \text{and} \quad a_{\max} = \max_{\alpha,\alpha',\lambda} \left(\left|a^\lambda_{\alpha,\alpha'}\right|\right) \tag{4.71}$$

and investigate their magnitudes for several materials in section 6.2.5.

4.7. Optical limit

For excitations with light in the optical range, i.e. 400 nm – 700 nm, the momentum transfer to the electron is negligible. For example, a photon with a wave-length of 400 nm carries a momentum of $\sim 1 \times 10^{-3}$ in atomic units. Thus, we will investigate the limit of $\boldsymbol{q} \to 0$ in the following. As discussed in section 2.5.1, to treat this limit it is useful to compute the modified polarizability $\bar{P}$ instead of the susceptibility χ. In the context of the BSE, this just amounts to replace the full Coulomb potential in the exchange term, eq. (4.26), with the long-range-truncated one eq. (2.44) [5]. Equation (4.64) then becomes

$$\bar{P}^{\mathrm{R}}_{\boldsymbol{G}\boldsymbol{G}'}(\boldsymbol{q}_{\mathrm{mt}}, \omega) = \sum_\lambda \left(\frac{1}{\omega - E_\lambda + \mathrm{i}\delta} + \frac{1}{-\omega - E_\lambda - \mathrm{i}\delta}\right) t^*_\lambda(\boldsymbol{G}, \boldsymbol{q}_{\mathrm{mt}}) t_\lambda(\boldsymbol{G}', \boldsymbol{q}_{\mathrm{mt}}). \tag{4.72}$$

In order to take the limit $\boldsymbol{G} = 0$, $\boldsymbol{G}' = 0$, and $\boldsymbol{q}_{\mathrm{mt}} \to 0$, we first approximate the plane-wave matrix elements by the dipole matrix elements D (see D.2)

$$M^{\mathrm{r}}_{\alpha}(0, \boldsymbol{q}) \overset{q \ll 1}{=} \mathrm{i} \sum_{j} D^{\mathrm{r}}_{\alpha,j} q_j, \tag{4.73}$$

where we define the resonant dipole matrix elements in terms of the momentum operator as

$$D^{\mathrm{r}}_{\alpha,j} = \mathrm{i} \frac{\langle u\boldsymbol{k} | \hat{p}_j | o\boldsymbol{k} \rangle}{\epsilon_{u\boldsymbol{k}} - \epsilon_{o\boldsymbol{k}}}. \tag{4.74}$$

Inserting eq. (4.73) into eq. (4.63) yields for the transition coefficients

$$t_{\lambda}(0, \boldsymbol{q}) = -\mathrm{i} \left(\boldsymbol{X}_{\lambda} + \boldsymbol{Y}_{\lambda} \right)^{\dagger} \mathbf{F}^{\frac{1}{2}} \mathbf{D}^{\mathrm{r}*} \frac{\hat{\boldsymbol{q}}}{|\boldsymbol{q}|} =: -\mathrm{i} \left(\boldsymbol{X}_{\lambda} + \boldsymbol{Y}_{\lambda} \right)^{\dagger} \tilde{\mathbf{D}}^{\mathrm{r}*} \frac{\hat{\boldsymbol{q}}}{|\boldsymbol{q}|}. \tag{4.75}$$

where $\hat{\boldsymbol{q}}$ is the unit vector along the direction of $\boldsymbol{q}$, and we have included the occupation factors into $\mathbf{D}$. This allows us to cancel the $1/|\boldsymbol{q}|^2$ factor of the Coulomb potential, and we write

$$\begin{aligned} \varepsilon_{\mathrm{M}}(\omega) &= 1 - \lim_{q \to 0} \frac{4\pi}{q^2} \bar{P}_{0,0}(\boldsymbol{q}, \omega) \\ &= 1 - 4\pi \sum_{i,j} \hat{q}_i \left(\sum_{\lambda} \left(\frac{1}{\omega - E_{\lambda} + \mathrm{i}\delta} + \frac{1}{-\omega - E_{\lambda} - \mathrm{i}\delta} \right) t^{*}_{\lambda,i} t_{\lambda,j} \right) \hat{q}_j, \end{aligned} \tag{4.76}$$

where

$$t_{\lambda,i} = -\mathrm{i} \sum_{\alpha} \left(\boldsymbol{X}_{\lambda} + \boldsymbol{Y}_{\lambda} \right)^{\dagger}_{\alpha} \tilde{\mathbf{D}}^{\mathrm{r}*}_{\alpha,i} \tag{4.77}$$

define the transition coefficients for each Cartesian direction. From this expression we can recover the form of the (macroscopic) transversal dielectric matrix eq. (2.30)

$$\varepsilon^{ij}_{\mathrm{M}}(\omega) = \delta_{ij} - 4\pi \sum_{\lambda} \left(\frac{1}{\omega - E_{\lambda} + \mathrm{i}\delta} + \frac{1}{-\omega - E_{\lambda} - \mathrm{i}\delta} \right) t^{*}_{\lambda,i} t_{\lambda,j}. \tag{4.78}$$

As noted in section 2.4, we are mainly interested in the imaginary part of ε which is given by a sum of scaled positive and negative Lorentzian functions of width δ centered at the positive and negative BSE eigen-energies, respectively. The roots of the real part, on the other hand, are also useful to interpret the spectrum in terms of the classical Drude-Lorentz model. They can be used to determine the positions of plasmoic excitations [35].

$$\mathfrak{I}\left[\varepsilon^{ii}_{\mathrm{M}}(\omega)\right] = \sum_{\lambda} 4\pi^2 \left| t_{\lambda,i} \right|^2 \left(\frac{1}{\pi\delta} \frac{\delta^2}{(\omega - E_{\lambda})^2 + \delta^2} - \frac{1}{\pi\delta} \frac{\delta^2}{(\omega + E_{\lambda})^2 + \delta^2} \right), \tag{4.79a}$$

$$\mathfrak{R}\left[\varepsilon^{ii}_{\mathrm{M}}(\omega)\right] = 1 - \sum_{\lambda} 4\pi^2 \left| t_{\lambda,i} \right|^2 \left(\frac{1}{\pi} \frac{\omega - E_{\lambda}}{(\omega - E_{\lambda})^2 + \delta^2} - \frac{1}{\pi} \frac{\omega + E_{\lambda}}{(\omega + E_{\lambda})^2 + \delta^2} \right). \tag{4.79b}$$

The scaling factors are determined by the oscillator strengths.

5. Implementation of the q-dependent BSE beyond the TDA in `exciting`

In this chapter, the changes made to the `exciting` code that were needed to set up and solve the q-dependent BSE without the TDA using the concepts of chapter 4 are described. First, in section 5.1 the general features of the `exciting` code are presented. Then, in section 5.2 the major changes to the pre-existing routines of the BSE module are discussed for each sub-task. A broad overview of the work flow is given in fig. 5.2, while detailed listings of input/output files, new source code files, and new input elements can be found in appendices G to I.

5.1. The `exciting` code

`exciting` is a *full-potential all-electron* computer package that implements methods of density-functional theory and many-body perturbation theory for periodic systems. It is able to achieve highly accurate results due to its finely tunable *(linearized) augmented plane-wave basis set* that allows for the additional inclusion of *local orbitals* (see appendix C). Apart from ground-state properties, such as structural parameters and elastic moduli, the package contains different methods for describing excited state properties. On the one hand, it contains an implementation of *time-dependent density-functional theory*, that aims at the calculation of optical and electron-loss spectra of materials with weak electron-hole interactions. On the other hand, it implements the single-shot G_0W_0 approach (see section 3.3.3) to generate the quasi-particle band structure, and the BSE formalism to describe the optical absorption spectrum of systems with strongly bound excitons (see section 3.3.4). A full review of the capabilities of the code can be found in ref. [10], and at exciting-code.org.

5.1.1. Ground state calculations

At its core `exciting` solves the Kohn-Sham (KS) equations of DFT self-consistently (see section 3.2) for a periodic effective potential $v_{\text{eff}}(\boldsymbol{r} + \boldsymbol{R}) = v_{\text{eff}}(\boldsymbol{r})$ using the non-orthogonal (L)APW+lo basis (see appendix C for a detailed description of the basis). In the basis functions ϕ_j, the Bloch wave functions $\phi_{n\boldsymbol{k}}$ are expressed as

$$\phi_{n\boldsymbol{k}}(\boldsymbol{r}) = \sum_j c_j \phi_j(\boldsymbol{r}), \tag{5.1}$$

and the KS equations are then solved for each $\boldsymbol{k}$-point independently using the secular equation

$$\sum_j H_{ij} c_j^{(n)} = \varepsilon^{(n)} \sum_j S_{ij} c_j^{(n)}, \tag{5.2}$$

where $\varepsilon^{(n)}$ are the KS eigenvalues, H_{ij} denote the Hamiltonian matrix elements

$$H_{ij} = \left\langle \phi_i \middle| \hat{\mathrm{h}}_{\mathrm{KS}}(\boldsymbol{r}) \middle| \phi_j \right\rangle \tag{5.3}$$

and S_{ij} are the overlap matrix elements

$$S_{ij} = \left\langle \phi_i \middle| \phi_j \right\rangle . \tag{5.4}$$

The ground-state module of `exciting` grants access to the KS eigenstates and eigenvalues for a uniformly spaced grid in k-space.

5.1.2. Excited state calculations

The description of excited-state quantities, such as optical absorption or electron energy loss spectrum, relies on the computation of the retarded density correlation function χ^{R} (see chapter 2), and `exciting` provides two methods for this purpose: One is based on TDDFT, which is the extension of the KS scheme to time-dependent effective potentials [36], where χ^{R} is computed with the time-dependent exchange-correlation kernel (see appendix E, eq. (E.14)). In the other method, the Bethe-Salpeter equation is solved. In the following we discuss the second approach exclusively.

5.1.3. Previous BSE implementation

The previous implementation of the BSE was used the Tamm-Dancoff approximation (see sections 3.3.5 and 4.6) and the computation of the macroscopic dielectric tensor in the optical limit of vanishing momentum transfer, i.e. $\boldsymbol{q}_{\mathrm{mt}} = 0$ (see sections 2.4.2 and 4.7) [20]. The code was structured into a collection of interdependent code blocks, or *tasks*, that are executed when `exciting` does a BSE calculation. This task-structure is mostly unchanged in extensions to the code discussed in this thesis. It is displayed in figure 5.2.

5.2. Extensions to the BSE implementation

In the following sections we discuss the extensions made to the BSE-tasks and other auxiliary routines that are needed for the q-dependent BSE beyond the TDA. A detailed listing of all required input files and generated output files, as well as a short description for each task can be found in table G.1. Table H.1 lists the main source code files for each BSE-task, while table H.2 list new inter-task support modules. Newly introduced `exciting`-input elements are listed in table I.1. Further information can be found in the in-code documentation and the `excitingsubroutines.pdf` document that can be generated using the make system of `exciting`.

5.2.1. One-shot ground-state calculations

Starting from the density and KS potential of a converged ground-state (GS) calculation, `exciting` executes two additional one-shot GS calculations when the BSE is to be solved.

The first one is done by the task `xsgeneigvec` and the calculated eigenvalues and eigenstates are used in the construction of the BSE Hamiltonian and the macroscopic dielectric matrix (or function). Due to the much higher computational demand of a BSE calculation compared to a GS one, the k-space is usually sampled with a much coarser grid. Additionally, the k-grid is generally shifted from the Γ-point by some offset $\boldsymbol{v}_{\text{off}}$ to avoid points of high symmetry. The second GS calculation is done by the task `scrgeneigvec`. The results of this calculation are used to build the KS dielectric response that is needed to set up the direct term of the BSE (see section 4.3.3). Here, all parameters of `xsgeneigvec` are adopted by default, but one usually chooses a higher number of unoccupied states to be computed in order to better converge the sum over states needed for the KS polarizability (see eq. (E.18)).

The setup of the BSE for an arbitrary momentum transfer $\boldsymbol{q}_{\text{mt}}$ also requires the KS eigen-solutions for the two k-grids $\{\boldsymbol{k}_+\}$ and $\{\boldsymbol{k}_-\}$ (see, e.g. eq. (4.28a)), which generally differ from the reference k-grid $\{\boldsymbol{k}\}$. To account for that, the wrapper routine (xsgeneigvec.F90) for the one-shot GS routine used in both tasks was changed. For the task `xsgeneigvec` it now also calculates the KS eigen-solutions for the two shifted grids for each momentum transfer vector specified in the input file, while the task `scrgeneigvec` still only needs to generate KS eigen-solutions for the reference k-grid. The used k-grids are sketched in fig. 5.1.a. For the generation of the $\boldsymbol{q}_{\text{mt}}$-derived offsets and various k-point index maps, the module `mod_xsgrids.f90` was introduced which makes use of the module `mod_kpointset.f90` of the *GW*-part of `exciting` .

5.2.2. Plane-wave matrix elements

Apart from the KS ground-state quantities, the main quantities needed in the BSE formalism as discussed in chapter 4 are the plane-wave matrix elements (PWE) $M_{mn\boldsymbol{k}}(\boldsymbol{G}, \boldsymbol{q})$. The core computational routine for their construction `ematqk`, was already available. It calculates the matrix elements in terms of the (L)APW+lo basis functions (see appendix D.3.1) for the case that both the bra- and ket-state belong to the same k-point grid, i.e. are stored in the same eigenvector file ($\boldsymbol{q}_{\text{mt}} = 0$). To account for arbitrary finite momentum this routine was extended to read the bra- and ket-states from differing eigenstate files and added the possibility to use the complex conjugate for of the bra-state. The last change is needed to compute the modified plane-wave matrix elements $N_{nmk}(\boldsymbol{G}, \boldsymbol{q})$ (see section 4.3.3 and appendix D.3.2). Additionally, the input and output of the routine were changed from global quantities stored in the module `modxs` to direct ones and grouped all routines related to the generation of the PWEs in the new module file `m_b_ematqk` to improve usability.

5.2.3. Screening calculation

The lattice Fourier coefficients of the KS microscopic dielectric function (screening) in the RPA $\varepsilon^0_{\boldsymbol{G}\boldsymbol{G}'}(\boldsymbol{q}, 0)$ (see eqs. (E.17) and (E.18)) are computed in the task `screen`. They are needed for the set up of the screened Coulomb interaction of the BSE Hamiltonian. If the TDA is used, these coefficients are only needed for those q-vectors formed by the difference vectors of the reference k-grid, i.e. $\{\boldsymbol{q} = \boldsymbol{k}' - \boldsymbol{k}\}$ (see eqs. (4.40) and (4.41)). Here,

the resulting q-grid is identical to the reference k-grid *without* offset. This case was already implemented and the corresponding core computational routine is `dfq`. However, if the coupling block is also considered in the BSE, the coefficients are also needed for the q-vectors formed by the sum of two reference k-grid vectors, i.e. $\{\boldsymbol{q} = -\boldsymbol{k}' - \boldsymbol{k}\}$ (see eq. (4.42)). This results in a q-grid with an offset, if the reference k-grid also has an offset (which is the usually the case). Thus, the wrapper routine `b_screenlauncher` was added that adjusts environmental settings such that `dfq` could be used with the shifted q-grid. In this case also the modified plane-wave matrix elements are used to replace eigenvectors at $-\boldsymbol{k}'$ with the computed ones at $\boldsymbol{k}$. The two q-grids are displayed in fig. 5.1.b. Since we are using symmetrically shifted k-grids for each momentum transfer vector $\boldsymbol{q}_{\text{mt}}$ in the BSE matrix elements, $\boldsymbol{q}_{\text{mt}}$ does not enter the screening calculations.

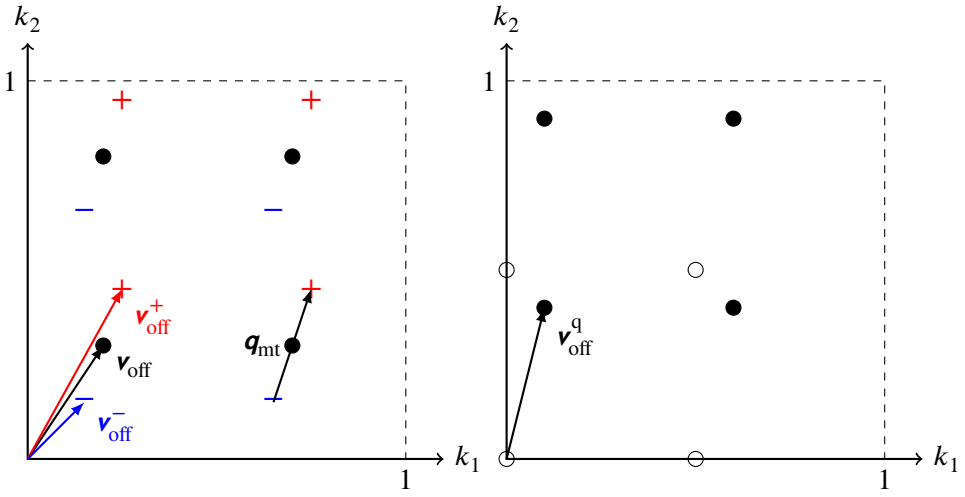

(a) The black dots represent the reference k-grid specified in the `xs`-part of the `exciting`-input. The shifted grids, denoted with + and -, are generated for each momentum transfer $\boldsymbol{q}_{\text{mt}}$ listed in the input.

(b) The hollow dots represent the difference vectors of the reference k-grid $\boldsymbol{q} = \boldsymbol{k}' - \boldsymbol{k}$, whereas the filled dots denote $\boldsymbol{q} = -\boldsymbol{k}' - \boldsymbol{k}$.

Figure 5.1.: k-grids needed for a q-dependent BSE calculation without the TDA.

5.2.4. BSE matrix elements

Index handling and selection of transitions

In order to handle the various indices for states and k-points appearing in the setup of the q-dependent BSE beyond the TDA, the support module `modbse` was introduced. It contains routines that generate and store the BSE-index map $\{\alpha \to u, \boldsymbol{k}_-, o, \boldsymbol{k}_+\}$ for a considered momentum transfer, where α labels a considered IP transition (see section 4.1). The module also generates the corresponding IP transition energies E_α (see eq. (4.21)) and the occupation factors F_α (see eq. (4.24)). The use of this index map in the following setup

of the BSE matrix elements allows for the inclusion of an arbitrary selection of IP transitions as a basis. Two selection methods were implemented:The first one behaves identical to the previous BSE implementation where all transitions between a selection of valence and conduction bands are considered. The only difference is that transitions with negative occupation difference (occupation inversion, should in general not occur) are excluded to ensure hermiticity of the Hamiltonian. The second one uses all IP transitions that lie within a specified energy range, which can lead to a different number of considered transitions for each k-point.

Exchange interaction matrix elements

The generation of the exchange matrix elements is handled by the task `exccoulint`. The associated routines were extended to handle finite $\boldsymbol{q}_{\mathrm{mt}}$ (see eq. (4.28a)) and to use the full non-truncated Coulomb potential in the non-TDA case. For zero momentum transfer the truncated Coulomb potential is still used (see section 4.7). As discussed in section 4.3.2, only the resonant-resonant block of $\mathbf{V}$ needs to be calculated even for non-TDA calculations. Another change with respect to the original implementation is that this task now uses the KS eigen-solution generated by the task `xsgeneigvec`, instead of those of task `scrxsgeneigvec`, in order to consistently differentiate between BSE and screening calculations.

Screened Coulomb interaction matrix elements

The generation of the screened Coulomb matrix elements (see section 4.3.3) is handled by the task `scrcoulint` and by the homonymous routine. As for the exchange matrix elements, the code was extended to handle finite $\boldsymbol{q}_{\mathrm{mt}}$, and code was added for the construction of the coupling block of $\mathbf{W}$ (see eqs. (4.41) and (4.42)). This task now also uses the results of `xsgeneigvec`. Additionally, the number of processes for the `MPI`-parallelization of this task is no longer restricted to the number of q-points, but can be chosen arbitrarily.

5.2.5. Setup and diagonalization of the BSE-Hamiltonian

The task `bse` is responsible for (a) the construction of the BSE Hamiltonian matrix from the previously calculated exchange and screened Coulomb interaction matrix elements, (b) the subsequent diagonalization of it, (c) the calculation of the dielectric function from the resulting eigenvalues and eigenvectors, and (d) the calculation of quantities derived from the dielectric function. The previous implementation does all these steps in the routine `bse` (`bse.F90`). In an effort to make the code more accessible and easier to extend this routine was refactored into several subroutines as listed in table H.1.

The module `m_setup_bse` now handles step (a) and, depending on whether the TDA is used or not, sets up either the resonant BSE Hamiltonian eq. (4.66) or the auxiliary Hamiltonian for the squared EVP eq. (4.52b). For step (b) the original implementation uses the linear algebra library `Lapack` [37] and thus can only utilize a single (multi-core) CPU and it's local memory. Since the involved matrices can become very large even in the TDA, the

possibility to use the distributed memory linear algebra library `ScaLapack` [38] was added. The library relies on the `BLACS` [39] library and requires the matrices to be distributed in a block-cyclic manner over the participating processes. To help with the use of `ScaLapack` and the distribution of the matrices the support module `modscl` was written (see table H.2). Instead of parallelizing the diagonalization itself, it is also possible to do it serially using `Lapack` and to distribute the specified momentum transfer vectors over the `MPI` processes. Lastly, steps (c-d) were adapted for the case of finite momentum transfer, i.e. eq. (4.65) and eq. (2.42) are now calculated. The output of this task has been restructured and is listed in detail in table G.1.

5.2.6. Post-processing of BSE-eigenvectors

A complete understanding of the BSE results includes not only the analysis of the spectra and of the exciton binding energies, but also of the electron-hole pair distribution, in real- and reciprocal-space. To that end `exciting` can write out a selected set of BSE-eigenvectors to a binary file after the diagonalization step (see table I.1). The task `writebevec` can then be used to write out the most important eigen-coefficients to a formatted text file. For usability, the possibility to select the exciton solution by energy instead of index was added. For the reciprocal-space analysis of the excitons, the excitonic weights can be inspected. They are defined for each occupied and unoccupied state that was considered in the BSE as

$$w^{\mathrm{r},\lambda}_{u\boldsymbol{k}_-} = \sum_o \left| X^{\lambda}_{(u\boldsymbol{k}_-)(o\boldsymbol{k}_+)} \right|^2 \quad \text{and} \quad w^{\mathrm{r},\lambda}_{o\boldsymbol{k}_+} = \sum_u \left| X^{\lambda}_{(u\boldsymbol{k}_-)(o\boldsymbol{k}_+)} \right|^2. \tag{5.5}$$

When the coupling blocks are also considered the anti-resonant weights can be computed as

$$w^{\mathrm{ar},\lambda}_{u\boldsymbol{k}_-} = \sum_o \left| Y^{\lambda}_{(u\boldsymbol{k}_-)(o\boldsymbol{k}_+)} \right|^2 \quad \text{and} \quad w^{\mathrm{ar},\lambda}_{o\boldsymbol{k}_+} = \sum_u \left| Y^{\lambda}_{(u\boldsymbol{k}_-)(o\boldsymbol{k}_+)} \right|^2. \tag{5.6}$$

These weights can then be interpolated onto a band structure path and plotted and visualized. For this purpose a `python`-script was available, but in order to do this step more efficiently the task `writekpathweights` was implemented which does the interpolation in `exciting` using the `bspline-fortran` [40] routines.

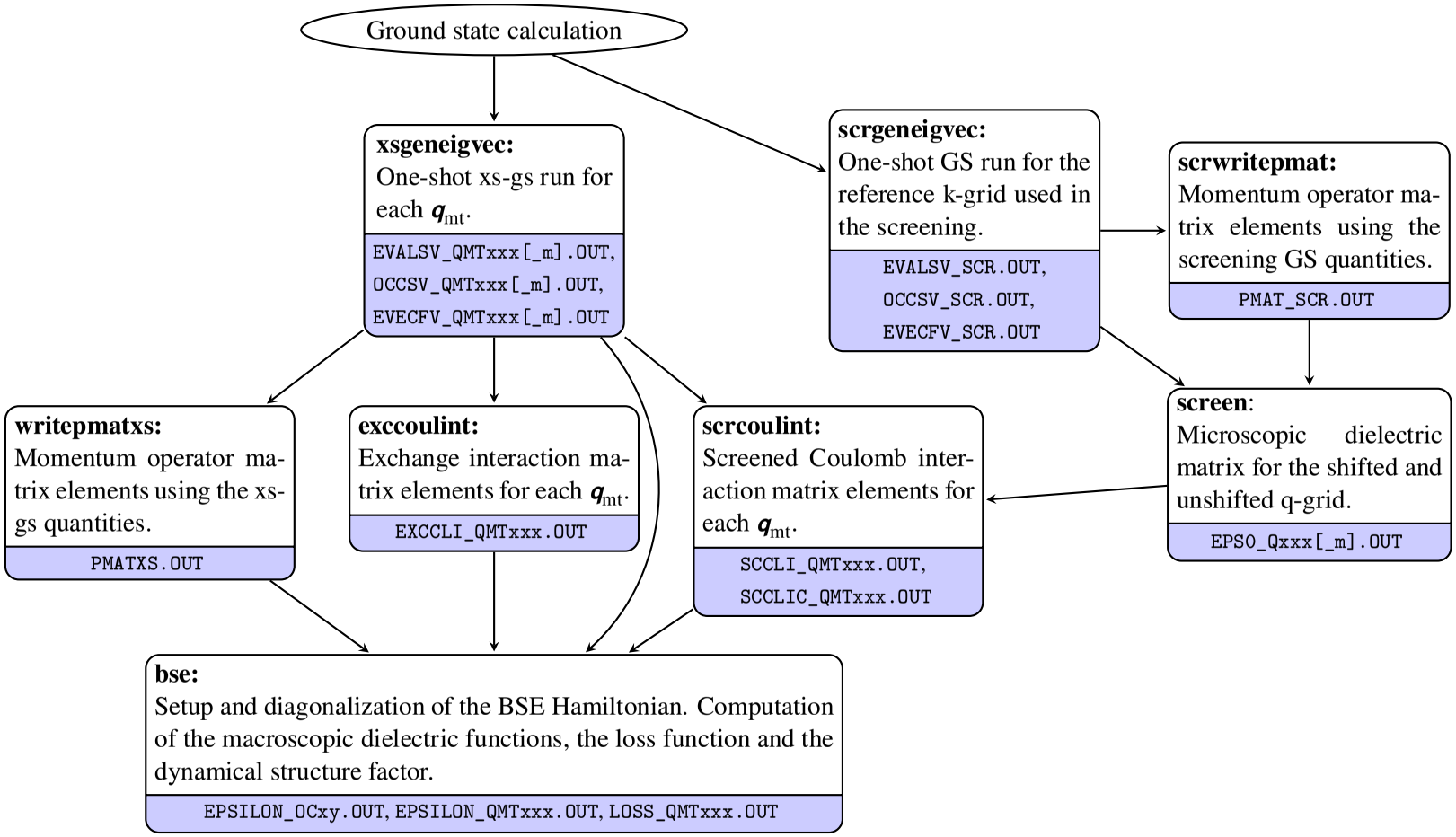

Figure 5.2.: Work flow of a BSE calculation with task names and main output files. The file extensions _QMTxxx and _m label the momentum transfer and indicate whether the k-grid is shifted by $-\boldsymbol{q}_{\mathrm{mt}}/2$ instead of by $\boldsymbol{q}_{\mathrm{mt}}/2$, respectively. In the case of screening calculation, the ending _m signals the use of the shifted q-grid. The analysis routines are not show here, but listed in table G.1.

6. Results

In this chapter numerical results that demonstrate the primary two features of the new BSE implementation are presented – the possibility to go beyond the TDA and to calculate the response of materials at finite momentum transfers. To that end, two groups of materials are investigated: 1) two prototypical solids silicon (Si) and lithium fluoride (LiF) and 2) three semiconducting organic crystals formed from naphthalene (2A), biphenyl (2P) and bithiophene (2T). The latter were chosen, since previous works [7, 41] report a breakdown of the TDA in similar materials.

6.1. Prototypical solids

Silicon is the most prototypical semiconductor with a relatively small indirect band gap of 1.17 eV [42]. No strongly bound excitons are found in its optical absorption spectrum. The insulator lithium fluoride, on the other hand, has a large direct band gap of 14.2 eV [42] and is known for its strongly bound exciton. Both materials have been studied in the context of the BSE beyond the TDA [6, 8, 9] and thus can be used to validate the current implementation.

6.1.1. Optical absorption

First, the effect of the TDA on the optical absorption spectrum is investigated. To that end the imaginary part of the transversal macroscopic dielectric tensor $\varepsilon_{\mathrm{M}}^{ij}(\omega)$ was calculated in the limit of vanishing momentum transfer $Q = 0$ (see sections 2.4.2 and 4.7).

Due to their cubic lattice symmetry, the dielectric tensor of Si and LiF is diagonal and has only one independent element. The xx-element of Si and LiF is calculated using the BSE with and without the TDA and shown in figs. 6.1 and 6.2, respectively. Additionally, the independent-particle spectrum is plotted as reference. It corresponds to zeroing the screened Coulomb interaction as well as the exchange interaction blocks of the BSE Hamiltonian, i.e. $\mathbf{W} = \mathbf{V} = 0$. The vertical bars indicate oscillator strengths $\left|t_{\lambda,x}\right|^2$ and energies of the dominant excitons [see eq. (4.79a)]. In all three cases the TDA and non-TDA spectra, as well as the positions and oscillator strengths of the excitons are nearly identical. A very slight decrease of the oscillator strengths can be observed when going beyond the TDA. The energies of the first (energetically lowest) excition for both methods are compared in table 6.1 for each material. The observed differences are of the order 10^{-3} – 10^{-4}eV, which also holds for the higher lying excitons. These differences are similar to the numerical precision of the BSE calculation with the used parameters (see section 6.1.4). Also the ratio between contributions of anti-resonant transitions to the eigenvectors is three orders of

magnitude smaller than those of the resonant transitions, i.e. $\left|Y_{\alpha,\lambda}\right| / \left|X_{\alpha',\lambda}\right| \sim 10^{-3}$. These observations agree well with the results published in [9].

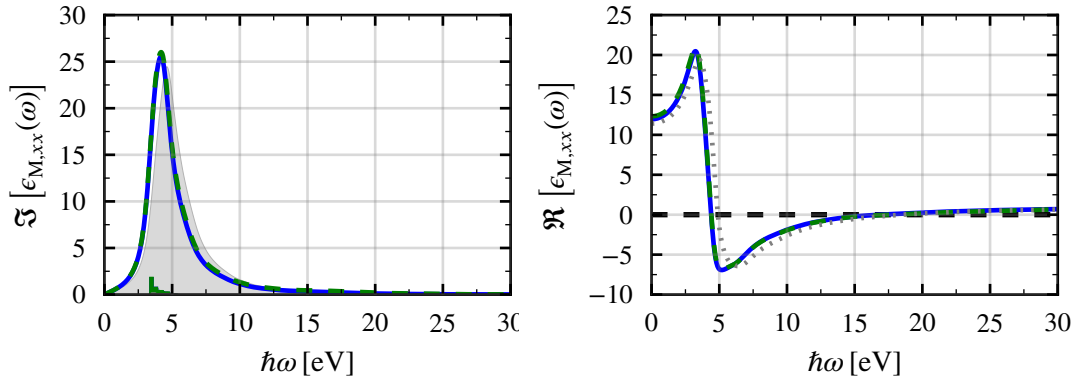

Figure 6.1.: Imaginary and real part of the macroscopic dielectric function of Si: BSE results with (dashed green curve) and without (solid blue curve) the TDA. The independent particle results are shown in grey. The vertical bars indicate the oscillator strengths of the dominant excitations.

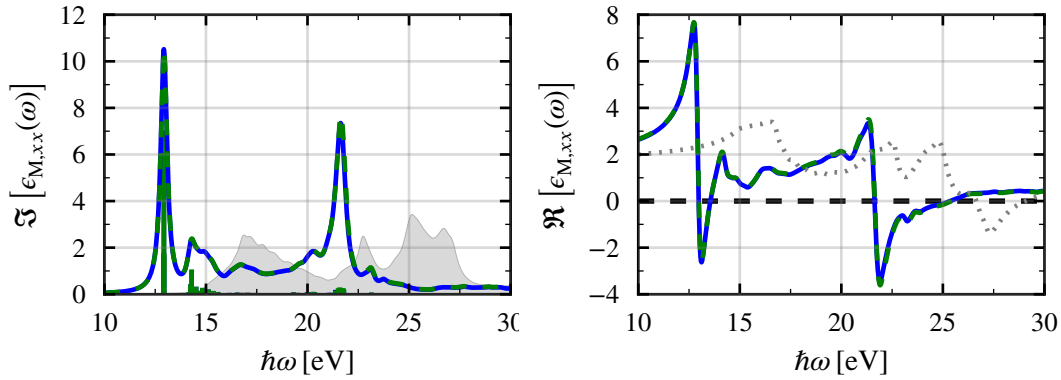

Figure 6.2.: Imaginary and real part of the macroscopic dielectric function of LiF: BSE results with (dashed green curve) and without (solid blue curve) the TDA. The independent particle results are shown in grey. The vertical bars indicate the oscillator strengths of the dominant excitations.

6.1.2. Electron energy loss

In Drude's model of metals, a plasmon is a collective excitation of the electrons which oscillate on a background of positively charged ions. According to the model, the position of the plasmon peak is situated at the energy at where the real part of the dielectric function changes from negative to positive values. This concept is often transferred to non-metals to interpret the resonances observed in EEL spectra at higher energies. In fig. 6.3 the electron energy loss function at vanishing momentum transfer $L_{xx}(\omega)$ [see eq. (2.28)] is shown for

Table 6.1.: Energies of the lowest energy exciton computed with and without the TDA and the corresponding differences. All energies are given in electron volts.

Material	E_1	E_1^{TDA}	ΔE_1
Si	3.4350	3.4353	-3×10^{-4}
LiF	12.925	12.932	-7×10^{-3}

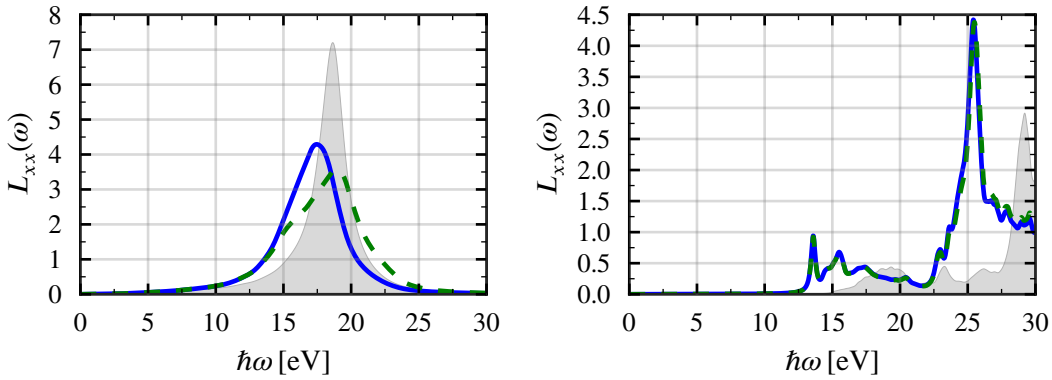

Figure 6.3.: Electron energy loss function for vanishing momentum transfer for silicon (left) and lithium fluoride (right).

silicon and lithium fluoride. The large peaks at around 16 eV (Si) and 26 eV (LiF) can be attributed to such plasmonic excitations, while the peak at 14 eV in the LiF spectrum is of excitonic nature. For LiF, no significant change between the TDA and non-TDA solution can be seen. Conversely, in the case of Si a considerable difference emerges. This was first reported in [6] and explained with the importance of the real part of ε for the EEL spectrum, which in turn requires a good description of the negative frequency transitions. In fig. 6.4 the result of the current implementation is compared with that of [6]. In the computation, 4 occupied, 12 unoccupied bands and a k-grid of $8 \times 8 \times 8$ was used. A rigid scissor shift was applied to open the KS band gap. The reference calculation also used 4 occupied, but 13 unoccupied bands and a total of 256 k-points. Additionally, the KS band structure was corrected by a *GW*-calculation. The computed TDA and non-TDA spectra are in good agreement with the reference.

Dynamical structure factor of Si

Next, the EEL spectra for finite momentum transfers are considered. To that end, the BSE is solved for $\mathrm{Q} \neq 0$ and the dynamical structure factor $S(\boldsymbol{Q}, \omega)$ [see eq. (2.38)] is computed. In fig. 6.5, we show the dynamical structure factor of silicon along the Γ–X path. Observed is the plasmon peak at around 20 eV that fades out with increasing Q. No pronounced excitonic features are visible.

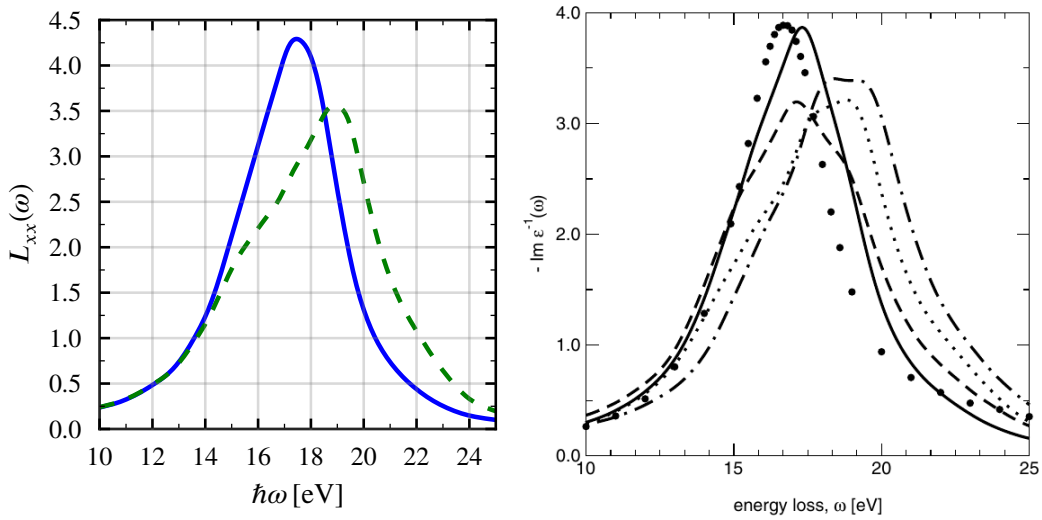

Figure 6.4.: Electron energy loss function of Si at vanishing momentum transfer. Left: Current result with (solid line) and without (dashed line) TDA. Right: Results of [6]. Dots: experimental data from [43]; solid line: BSE including coupling terms on top of GW corrected DFT-LDA bands; dotted line: same as the solid line but neglecting the coupling.

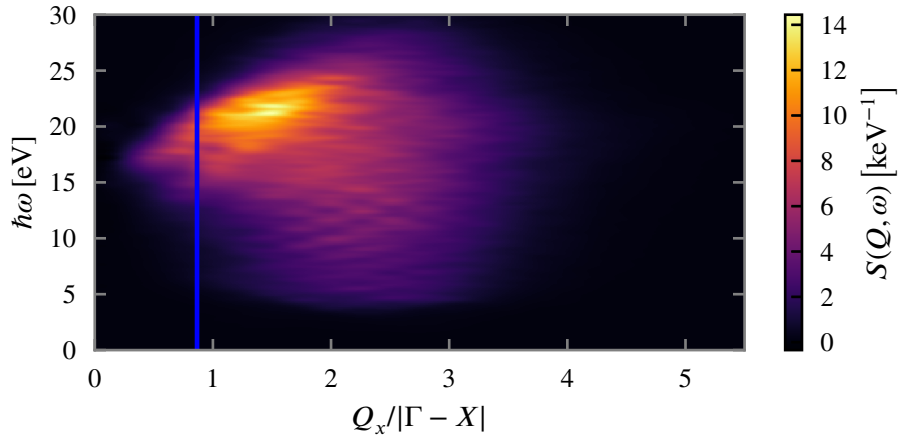

Figure 6.5.: Dynamical structure factor of Si along the Γ–X path. The electron energy loss spectrum was calculated for momentum transfer vectors $\boldsymbol{Q}$ in steps of $|\Gamma–X|/4$ and intermediate points were interpolated linearly. The blue line indicates the slice of the spectrum plotted in fig. 6.6.

In order to compare the results with the measurements and previous TDDFT computations reported in [44], the DSF for $Q = 0.53\,\mathrm{a_0}^{-1}$ along the same direction was computed. The results of the computations are shown in fig. 6.6 together with the results of [44]. Opposite to the behaviour at $Q = 0$, going beyond the TDA reduces the intensities and red-shifts the main peak slightly. For both methods good agreement for the positions and relative intensities of the spectral features is found. The absolute intensities of the measurements

are not reproduced.

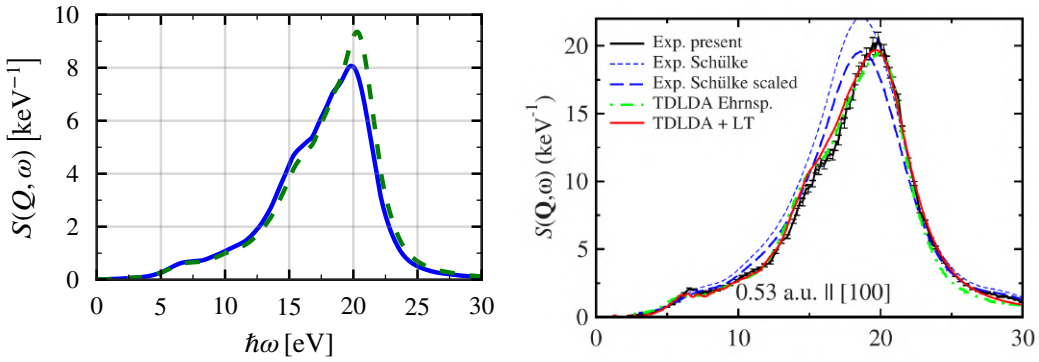

Figure 6.6.: Dynamical structure factor of Si for $Q_{\mathrm{mt}} = 0.53\,\mathrm{a_0}^{-1}$ along the Γ–X direction ([100]). Left: Current results using the BSE with (dashed line) or without (solid line) the TDA. Right: Experimental and computational results reported in [44].

As a final test for silicon, the longitudinal dielectric function for $Q = 0.795\,\mathrm{a_0}^{-1}$ along the Γ–L direction was computed and is compared with the results of [9] in fig. 6.7. The spectra of the full and approximated BSE computations agree well with the reference. The absolute values and the position of the peaks are comparable and the emergence of the peak at ~ 17 eV when the TDA is lifted is observed as reported in [9].

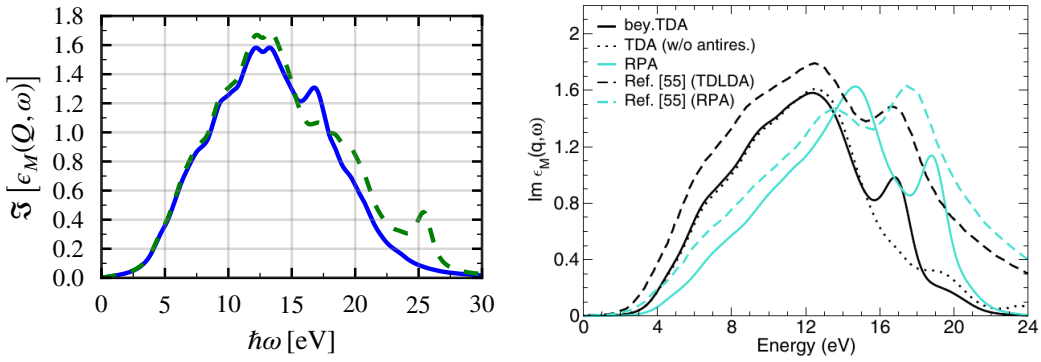

Figure 6.7.: Longitudinal macroscopic dielectric function of Si for $Q = 0.795\,\mathrm{a_0}^{-1}$ along the Γ–L direction ([111]). Left: Current results using the BSE with (dashed line) or without (solid line) the TDA. Right: Numerical results of [9]. Full BSE (solid black line) and TDA (dotted line) excluding the negative-frequency branch in eq. (4.65).

Dynamical structure factor of LiF

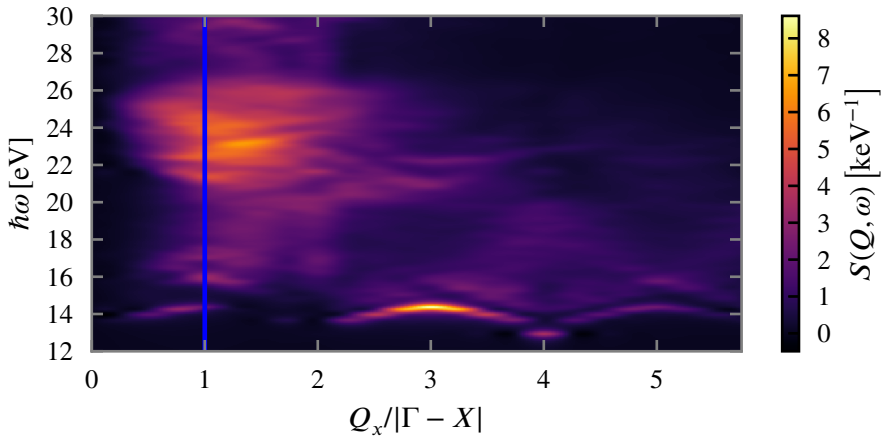

Figure 6.8.: Dynamical structure factor of LiF along the Γ–X path calculated using the BSE without the TDA. The DSFs were calculated for momentum transfer vectors in steps of $|\Gamma–X|/4$ and intermediate points were interpolated linearly. The DSF $Q = X$ indicated by the blue vertical line is shown in fig. 6.9

In the following, tests of the current q-dependent BSE implementation for the strongly excitonic LiF are presented. The dynamical structure factor along the Γ–X direction was computed using the full BSE and the result is shown in fig. 6.8. Compared to the result at $Q = 0$ the plasmon peak shifts to lower energies for increasing Q-values and eventually dissipates at around $3.5|\Gamma–X|$. The narrow peak at around 14 eV is attributed to a tightly bound exciton and its intensity is strongly modulated. Overall, the current results are in good agreement with the calculations published in [8] which used the TDA and the experimental spectrum published in [45]. In [8], it is argued that the ultimate disappearance of the plasmon and the exciton peaks for higher q-values is governed by the decay of the independent-particle transition coefficients, i.e. the plane-wave matrix elements [see eq. (4.63)]. The modulation of the excitonic peak, on the other hand, can only be explained when also the BSE eigenvectors are used in the construction of the transition coefficients and thus demonstrates the many-body character of the excitation.

In contrast to the results at vanishing momentum transfer, differences between the TDA and the non-TDA results are obsevable at finite Q. This is demonstrated in fig. 6.9 for $\boldsymbol{Q} = \boldsymbol{X}$. The excitonic peak is barely affected by the approximation and only slightly red-shifted. Likewise, the oscillator strength of the exciton remains largely the same. However, the high energy part of the spectrum (21 eV and above) that is defined by the plasmon exhibits more pronounced differences. In this range, the oscillator strengths are redistributed resulting in a decrease of the overall intensity and a slight red-shift of the plasmon peak. This is consistent with the issues of the TDA to describe the plasmon peak of Si. The TDA solution exhibits a significantly larger intensities above 26 eV. However, this cannot definitely be attributed to a breakdown of the TDA, since transition energies up to 29 eV were used to build the BSE Hamiltonian. Thus, the observed differences in the high energy end of the

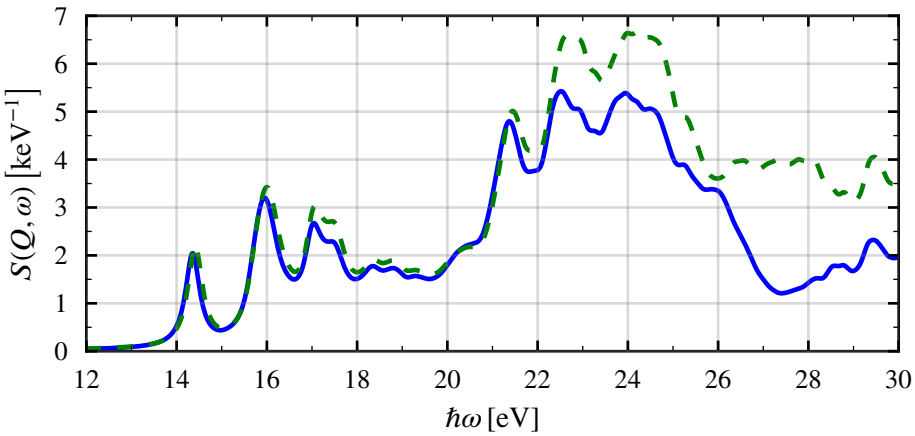

Figure 6.9.: Dynamical structure factor of LiF computed using the BSE with (dashed) and without (solid) the TDA at a momentum transfer of $\boldsymbol{Q} = \boldsymbol{X}$.

spectrum cannot be excluded to be due to a differing convergence behaviours of the TDA and non-TDA approach with respect to the number of used bands.

6.1.3. Exciton band structure

The possibility to access the BSE eigenvalues and eigenvectors at any momentum transfer allows for a detailed analysis of measured spectra from electron energy loss or inelastic x-ray scattering experiments on the level of individual excitations. In order to demonstrate this, the exciton band structure of the first four (bound) excitons along the Γ–X direction is shown in fig. 6.10 and is in good agreement with the results of [8]. As expected, the excitonic energies are periodic with respect to the reciprocal lattice vector $2X$. Conversely, the oscillator strengths are not and exhibit varying and decaying intensities with respect to Q. The absolute energy of the excitons increases with increasing distance to the Γ-point (or equivalent point). This is due to the fact that LiF has a direct band gap at Γ so that excitons composed of non-direct transitions must necessarily have higher energies. It is not directly obvious, why the three lowest degenerate excitons at Γ split with increasing distance from Γ. To investigate this further, the resonant excitonic weights [see eq. (5.5)] of the first and third exciton are shown for $\boldsymbol{Q} = \boldsymbol{\Gamma}$ and $\boldsymbol{Q} = \boldsymbol{X}$ in fig. 6.11. The anti-resonant are six orders of magnitude smaller and do not contribute. The distribution of the weights illuminates the stronger increase in energy of the third exciton compared to the first. At a momentum transfer of $Q = \Gamma$ both excitons are mainly composed of transitions from one of the three degenerate valence states at Γ to the corresponding lowest conduction states. When a momentum transfer of $\boldsymbol{Q} = \boldsymbol{X}$ is required, transitions starting from Γ are no longer energetically favourable. Instead the main contribution to the excitons stems from transitions starting from X and ending in Γ. The valence bands are no longer fully degenerate at X; one of the three valence bands is shifted by approximately 2 eV to lower energies. The third exciton includes transitions starting mainly from this band, and consequently has a

higher energy.

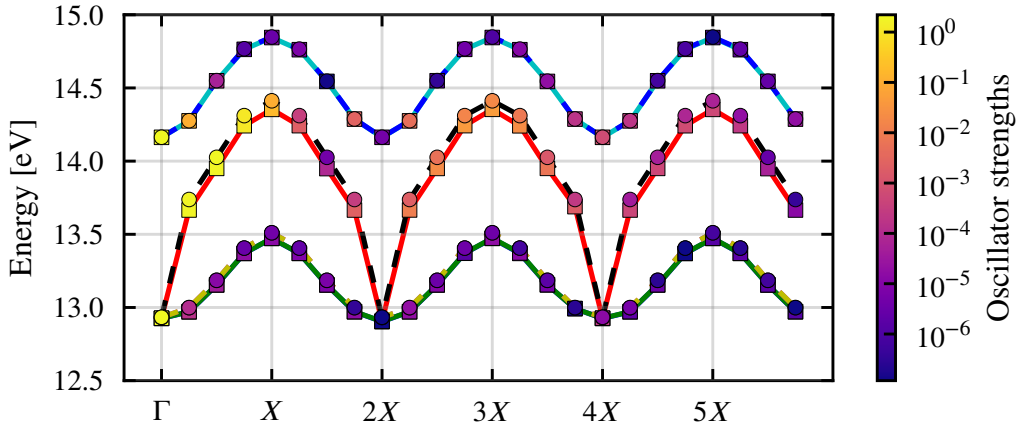

Figure 6.10.: Exciton band structure of LiF along Γ–5X for the four lowest excitons (the first two are degenerate). Shown is the absolute excitonic energy over the momentum transfer $\boldsymbol{Q}$ for both the TDA solutions (dashed lines) and non-TDA solutions (solid lines). The circles (TDA) and squares (non-TDA) indicate the oscillator strengths.

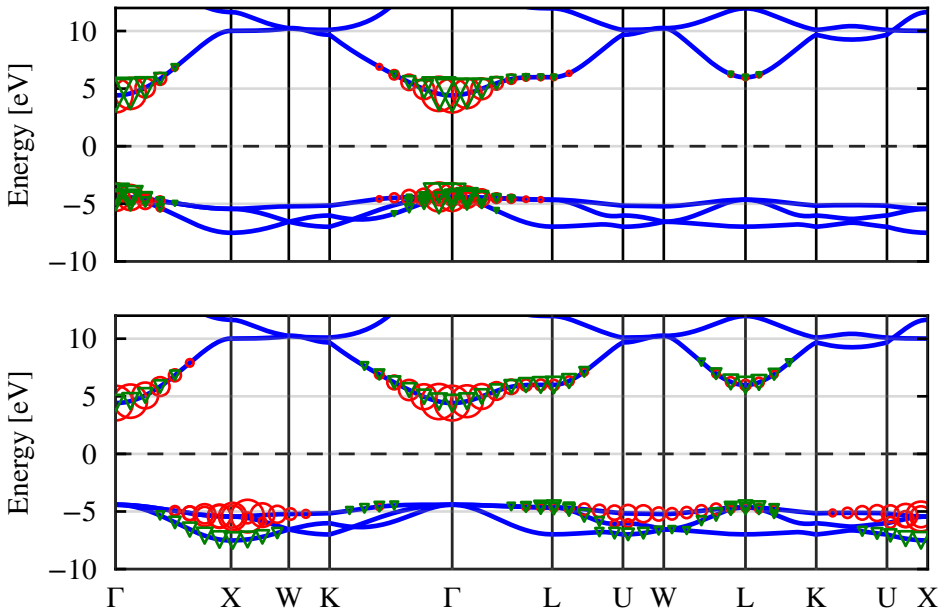

Figure 6.11.: Resonant excitonic weights of the first (red circles) and third (green triangles) exciton of LiF at $\boldsymbol{Q} = 0$ (top) and $\boldsymbol{Q} = \boldsymbol{X}$ (bottom).

6.1.4. Computational details

As noted in section 4.2, all BSE computations of this work are based on the KS wave functions and eigenvalues in place of the corresponding quasi-particle quantities. For all KS calculations the LDA exchange-correlation functional of Perdew and Wang [46] was used. The crystal structures for Si and LiF used in the calculations were procured from the *Inorganic Crystal Structure Database* [47] and stem from powder diffraction measurements of refs. [48, 49], respectively. No further structure relaxation was done. The ground state calculations used in the BSE were performed on a moderate k-grid of $8 \times 8 \times 8$. For both silicon and lithium fluoride 4 occupied and 12 unoccupied bands were used. The relatively light computational parameters were sufficient to verify the implementation against several reference calculations. The numerical error of the exciton energies for these parameters was estimated by running the same calculation using differing k-grid offsets and found to be of the order 10^{-3} or lower.

6.2. Molecular crystals

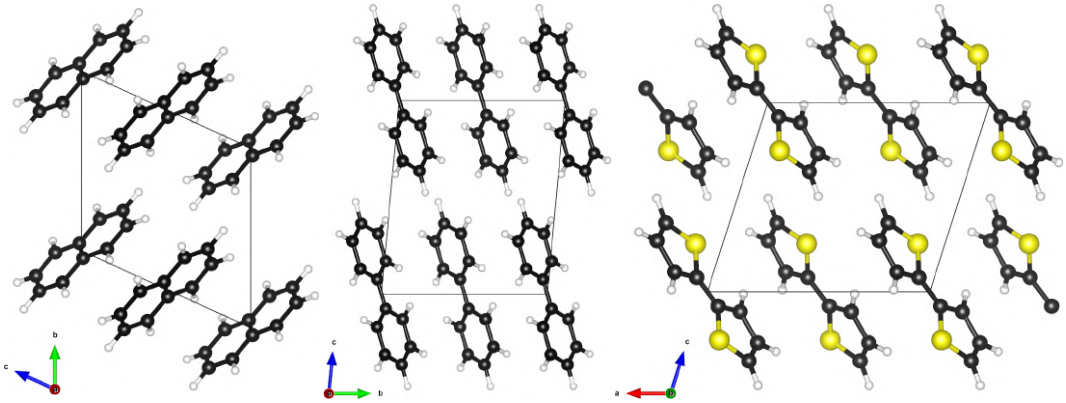

Figure 6.12.: Left to right: Naphthalene (2A), biphenyl (2P) and bithiophene (2T) molecular crystals. The bottom to top direction indicates the Cartesian y- (2A) or z-direction (2P and 2T). The vectors a, b and c show the direction of the used lattice vectors; the unit cell is outlined. Hydrogen, carbon and sulfur atoms are color-coded in white, black, and yellow, respectively.

6.2.1. Optical absorption

In [41], the effect of the TDA on the optical absorption spectra of several organic molecular crystals was investigated using the `WIEN2K` code [50]. In particular, the two crystals consisting of naphthalene and biphenyl molecules exhibited a relatively large shift in the spectrum. Consequently, these two systems are considered in the following in order to further validate the current implementation. Additionally, the molecular crystal formed from bithiophene is investigated. The structures of these materials are displayed in fig. 6.12. In

all cases the lattice is monoclinic, thus the diagonal components of the dielectric tensor differ from one another.

In figs. 6.13 and 6.14, the real and the imaginary part of the diagonal components which exhibit the most striking differences between the two approximations are shown. In contrast to the previously discussed materials, the spectra differ considerably for all three molecular crystals when the TDA is not used. The peak structure is shifted towards lower energies and, generally, the oscillator strengths are reduced. The same observation was made in [41]. The relative peak positions and intensities of the 2A and 2P spectra reported there agree well with the current results. Comparing the BSE eigenvalues of the TDA and non-TDA results reveals that the first few excitons are affected the most by the approximation (see fig. 6.15). This is reasonable considering that the exciton energy appears in the denominator of the coupling factors defined in eq. (4.70). In table 6.2, the differences between the TDA and non-TDA exciton energies are listed for the energetically lowest ($\lambda = 1$) and the maximally shifted exciton (λ_{max}) for each molecular crystal. The latter corresponds in all three cases to the first bright exciton. The observed shift for 2P agrees well with the shift reported in [41], while the shift for 2A is found to be about 25% smaller. While the oscillator strengths are overall reduced, they also redistribute, effectively red-shifting the peaks observed in the TDA spectrum even for energetically higher lying excitations. However, this redistribution also leads to an increased amplitude of some peaks relative to the corresponding TDA peak, e.g. the peaks around 3.6 eV and 8 eV in the naphthalene spectrum (see fig. 6.13). The computed static dielectric constants, i.e. $\varepsilon_i = \mathfrak{R}\left[\varepsilon^{ii}_{\text{M}}(0)\right]$, are listed in table 6.3. Similar to the behaviour of the imaginary part of the dielectric tensor, also the real part generally decreases when the TDA is lifted (see fig. 6.14). With respect to the results of [41], comparable but significantly smaller values are found. The results for 2T demonstrate the same general trends as those for 2A and 2P, but the effects are even more pronounced. The roots of the real part of the dielectric tensor of 2A and 2P indicate the presence of plasmonic excitations for energies larger than 5 eV in the case of 2A and 2P. For 2T this onset is around 8 eV. For all three materials the full BSE treatment drastically shifts the first root of $\mathfrak{R}\left[\varepsilon_{\text{M}}\right]$ in this regime to lower energies.

Table 6.2.: Energies of the lowest-energy exciton computed with and without the TDA and the corresponding differences. Additionally listed is the exciton with the highest difference which corresponds to exciton defining the first peak in the absorption spectra (fig. 6.13). In ref. [41] the shift of the first peak is referred to as the difference in excitonic binding energy ΔE_b. All energies are given in electron volts.

Material	E_1	E_1^{TDA}	ΔE_1	λ_{max}	$E_{\lambda_{\text{max}}}$	$\Delta E_\lambda^{\text{max}}$	ΔE_b^{ref}
2 A	1.81	1.83	−0.02	3	1.84	−0.34	−0.40
2 P	1.82	1.83	−0.01	6	2.17	−0.30	−0.28
2 T	1.36	1.77	−0.41	2	1.36	−0.41	-

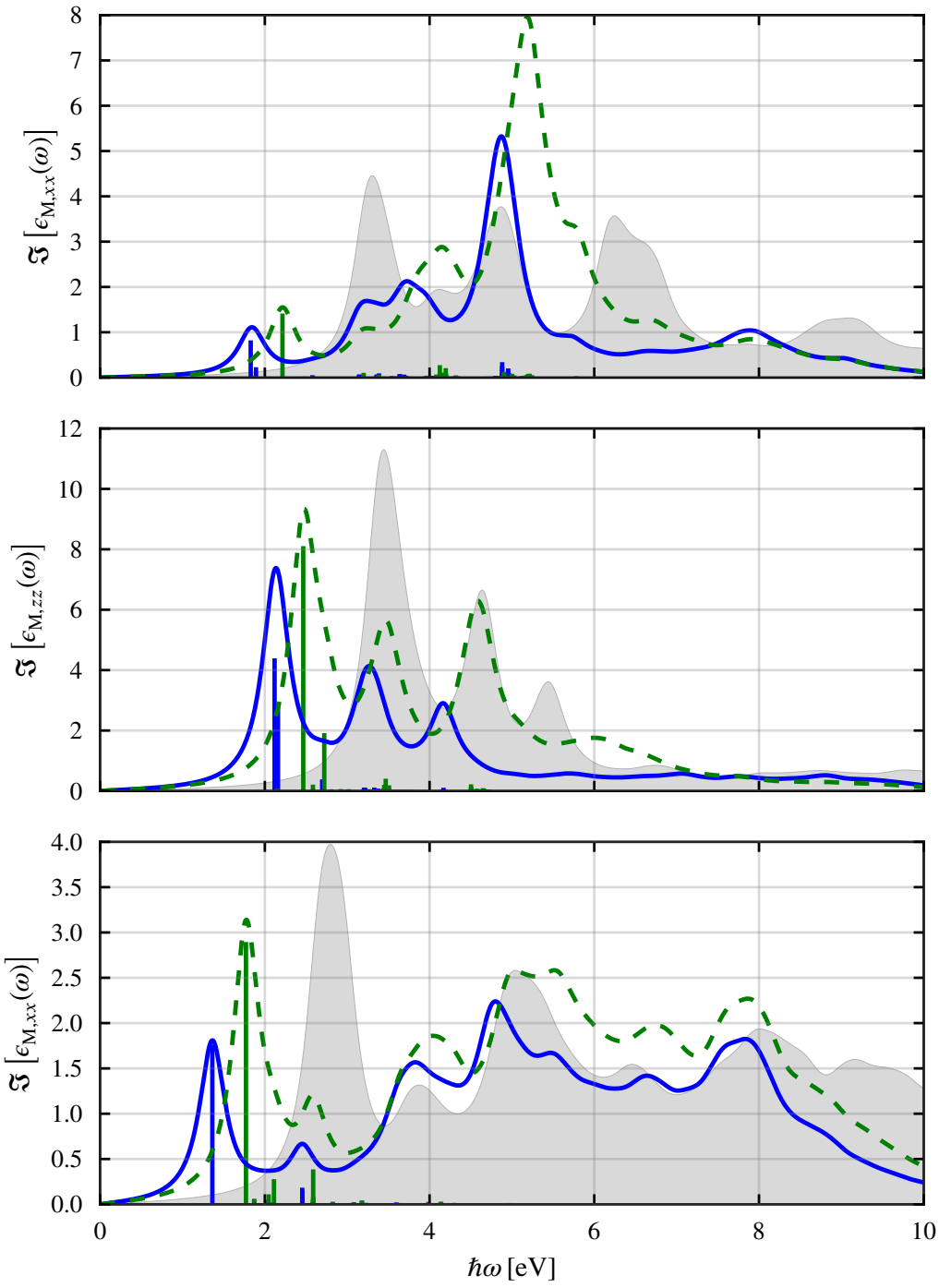

Figure 6.13.: Imaginary part of the macroscopic dielectric tensor of (top to bottom) naphthalene (2A), biphenyl (2P) and bithiophene (2T) calculated using the BSE with (dashed green line) and without (solid blue line) the TDA. The independent particle results are shown in grey. The vertical bars indicate the oscillator strengths of the dominant excitons.

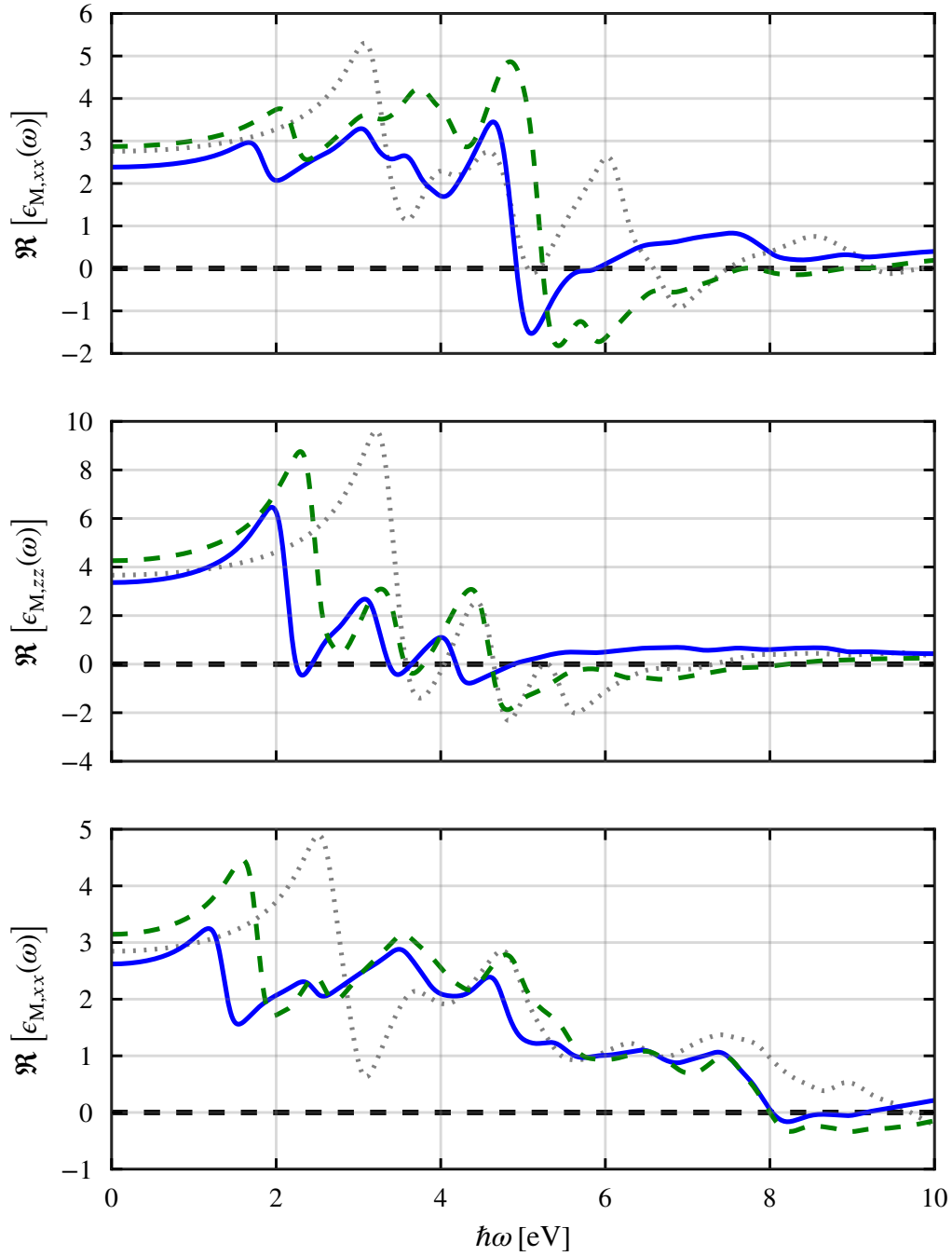

Figure 6.14.: Real part of the macroscopic dielectric function of (top to bottom) naphthalene (2A), biphenyl (2P) and bithiophene (2T) calculated using the BSE with (dashed green line) and without (solid blue line) the TDA. The independent particle results are shown in grey.

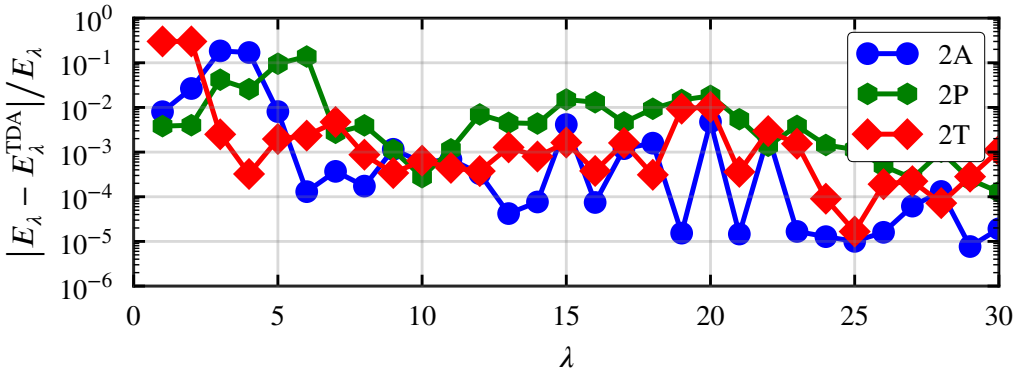

Figure 6.15.: Difference in magnitude of exciton energies for TDA and non-TDA results for the molecular crystals.

Table 6.3.: Static dielectric constants of 2 A, 2 P and 2 T for each Cartesian direction. The reference values are taken from [41] and correspond to the non-TDA results.

Material	ε_x	ε_y	ε_z	$\varepsilon_x^{\mathrm{TDA}}$	$\varepsilon_y^{\mathrm{TDA}}$	$\varepsilon_z^{\mathrm{TDA}}$	$\varepsilon_x^{\mathrm{ref}}$	$\varepsilon_y^{\mathrm{ref}}$	$\varepsilon_z^{\mathrm{ref}}$
2A	2.4	2.3	2.7	2.9	2.8	3.3	2.8	3.8	4.9
2P	2.1	1.9	3.4	2.5	2.1	4.3	3.1	3.5	4.6
2T	2.6	2.6	3.5	3.1	3.1	4.4	-	-	-

6.2.2. Electron energy loss

In fig. 6.16 the electron energy loss function for 2A and 2P is shown. As was already indicated by the zeros of the real part of the dielectric tensor, large plasmon peaks are visible above $\sim$ 5 eV and the full BSE treatment significantly changes the loss spectrum. The TDA completely fails to describe the low lying plasmonic at resonances at $\sim$ 6 eV (2A) and $\sim$ 5 eV (2P).

In [7] the effect of the TDA on the spectrum of the *trans*-azobenzene molecule and carbon nano-tubes was investigated. They also report considerable red-shifts of the peak structure, as well as a pronounced redistribution of the oscillator strengths in the optical absorption spectrum. It is then argued that the excitations in this system show a mixed excitonic-plasmonic behaviour, which cannot be captured using the TDA. This argumentation would also fit well to describe the behaviour of the molecular materials studied in this work. If we assume that there is a coupling between excitons and plasmons in these materials, then the strong effect of the TDA on the optical absorption spectra is not due to a wrong description of the bound excitons themselves, but the influence of the plasmons on the excitons is not captured correctly. Then, the difference to the case of LiF is that the plasmon is energetically closer to the excitons. The energy difference of the first exciton and the plasmon is $\sim$ 12 eV

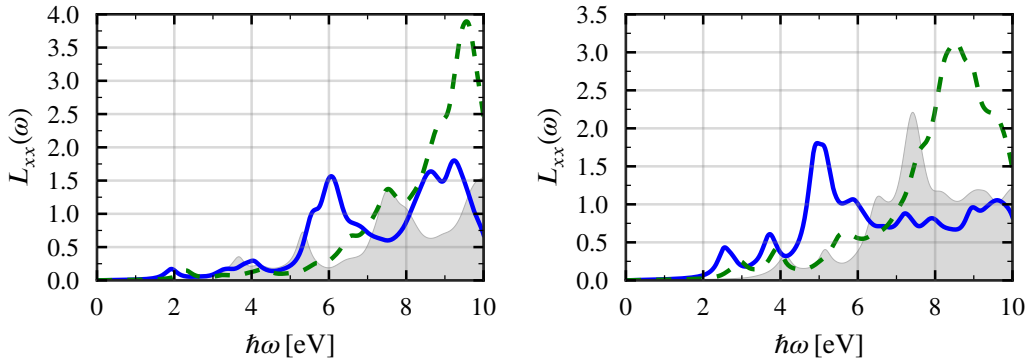

Figure 6.16.: Electron energy loss function for 2A (left) and 2P (right) calculated using the BSE with (dashed green line) and without (solid blue line) the TDA. The independent particle results are shown in grey.

in LiF, while it is only $\sim$ 4 eV in 2A. Further investigation on the energy dependence of this coupling is not within the scope of this work.

Dynamical structure factor of 2A

The Q dependence of the EEL spectrum was calculated for 2A using the full BSE. In fig. 6.19 the DSF for the Γ–Y path is shown. For four points along the path the DSF was calculated and the intermediate points were linearly interpolated. The spectrum exhibits a strong excitonic feature around 4 eV that gains in intensity the closer Q approaches Y. Additionally, two broader peaks at around 6.5 eV and 9 eV which are attributed to the plasmonic excitations, also visible at vanishing Q (see fig. 6.16), increase in intensity.

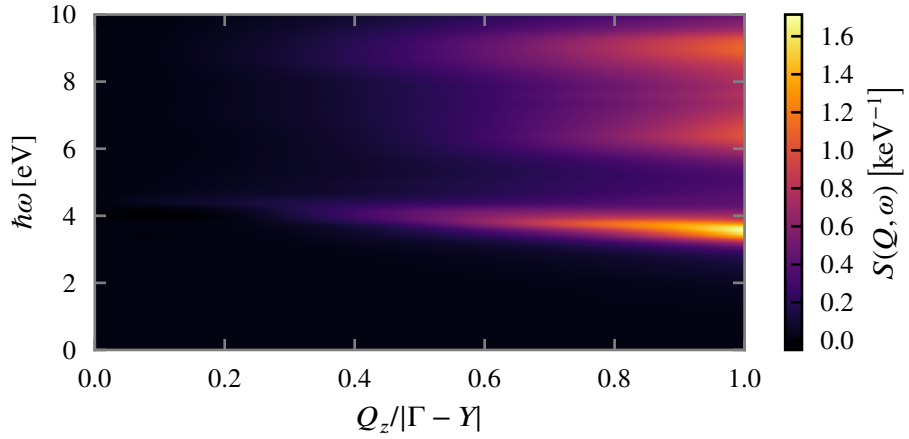

Figure 6.17.: Dynamical structure factor of 2A along the Γ–Y path: The DSF was calculated using the full BSE; Q was sampled in steps of $|\Gamma$–$Y|/4$ and intermediate points were interpolated linearly.

6.2.3. Excitonic weights

To further investigate the nature of the excitations, the excitonic weights are shown for the excitons most strongly affected by the TDA in fig. 6.18. Two observations can be made: 1) The weights are completely delocalized in k-space, consequently transitions from states of any k-point contribute to the excitations. By the usual Fourier arguments, this implies that the corresponding real-space extension of the excitation is strongly localized. 2) The positions of the relevant resonant and anti-resonant weights coincide, i.e. the same states are important for the excitation and the de-excitations processes. The maximal ratio between the resonant and anti-resonant weights is of the order 10^{-2} which is consistent with the observed ratio between the respective eigenvector components of 10^{-1}. The latter is two orders of magnitude larger than the ratio observed in the prototypical solids discussed previously.

6.2.4. Exciton band structure

The exciton energies of the four lowest energy excitons of 2A along the Γ–Y path are shown in fig. 6.19. One can observe two effects. First, the pair of the higher two excitons degenerates at Y. Second, that the lower two excitons drops rapidly about 0.3 eV in energy between $Y/4$ and $Y/2$. The first observation is likely due to the fact that the two lowest conduction bands also degenerate at Y. To investigate the second observation the resonant and anti-resonant excitonic weights are shown in fig. 6.20 for the first exciton at $\boldsymbol{Q} = \boldsymbol{\Gamma}$ and $\boldsymbol{Q} = \boldsymbol{Y}/2$. The significant increase in the anti-resonant weights could be seen as an indicator that at this Q-value a previously forbidden de-excitation channel was activated.

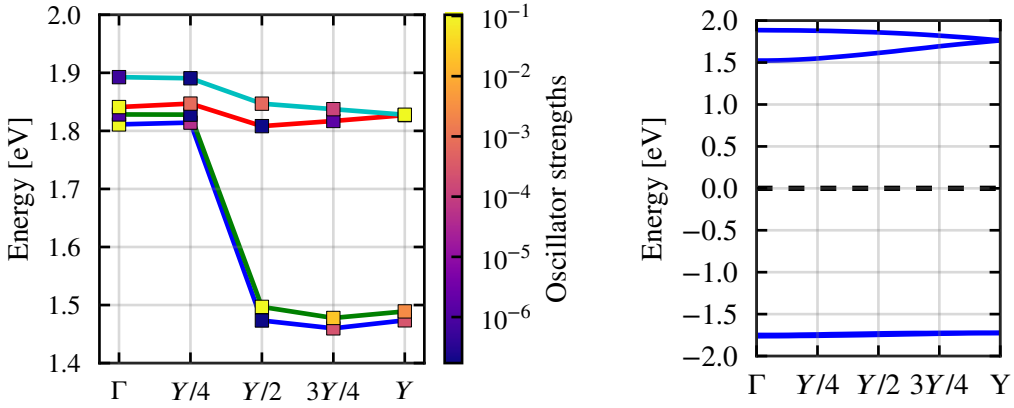

Figure 6.19.: Left: Exciton band structure of naphthalene (2A) along Γ–Y for the first four excitons. Shown is the absolute excitonic energy over the momentum transfer $\boldsymbol{Q}$ for full BSE solutions (solid line). Right: First two valence and conduction bands are dominantly contributing to the excitons.

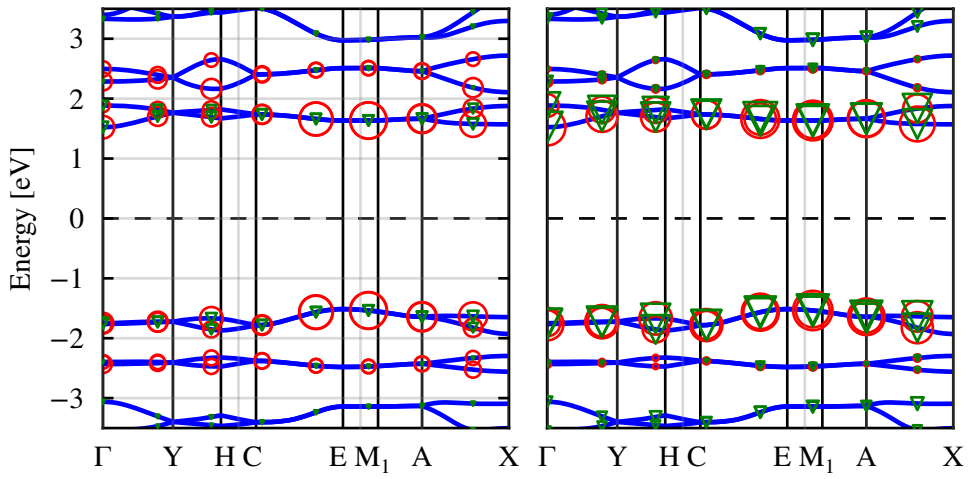

Figure 6.20.: Resonant (red cirles) and anti-resonant (green triangles) excitonic weights of the first exciton of 2 A at $\boldsymbol{Q} = 0$ (left) and $\boldsymbol{Q} = \boldsymbol{Y}/2$ (right). The anti-resonant weights are scaled by a factor of 5.

6.2.5. Coupling measures and artificial decoupling

In section 4.6.1 the resonant and anti-resonant coupling factors were introduced and the corresponding coupling measures were defined as the maximal occurring coupling factors [see eqs. (4.70) and (4.71)]. The measures for all considered materials and the case of zero momentum transfer were calculated. No scissor shift was used to open the LDA band gap in these calculations in order to compare the measures between the materials on equal footing. The results are listed in table 6.4. Two observations can be made: First, the anti-resonant coupling measures are consistently one order of magnitude smaller than the resonant ones. Second, the measures vary in a relatively narrow window. While the coupling measures of the molecular crystals are larger than those of the prototypical solids, the largest and smallest observed measure differ only by a factor of three. In order to properly evaluate whether the measures have predictive power, more materials need to be considered and strict convergence tests need to be conducted. This was not possible within the scope of the work.

In [7], the bare Coulomb interaction was identified as the dominant contribution to the BSE coupling. Since this term measures the degree of inhomogeneity of the electron density, the conclusion was drawn that the TDA description is prone to fail for inhomogeneous systems. The computations of the current work confirm that the matrix elements of the bare Coulomb interaction are about one order of magnitude larger than those of the screened one for the coupling terms for all considered materials (see table 6.4).

The coupling factors depend inversely on the independent-particle transition energies. Consequently, we expect that the size of the band gap crucially influences the applicability of the TDA. To demonstrate the decoupling of the resonant and anti-resonant problems we used scissor shifts of zero, one and ten Hartree to artificially open the band gap of

the naphthalene molecular crystal and solved the BSE with and without the TDA. Both measures decrease by one order of magnitude for each step and the resulting spectra are shown in fig. 6.21. As expected, the non-TDA spectrum becomes identical to the TDA one for increasing scissor shifts.

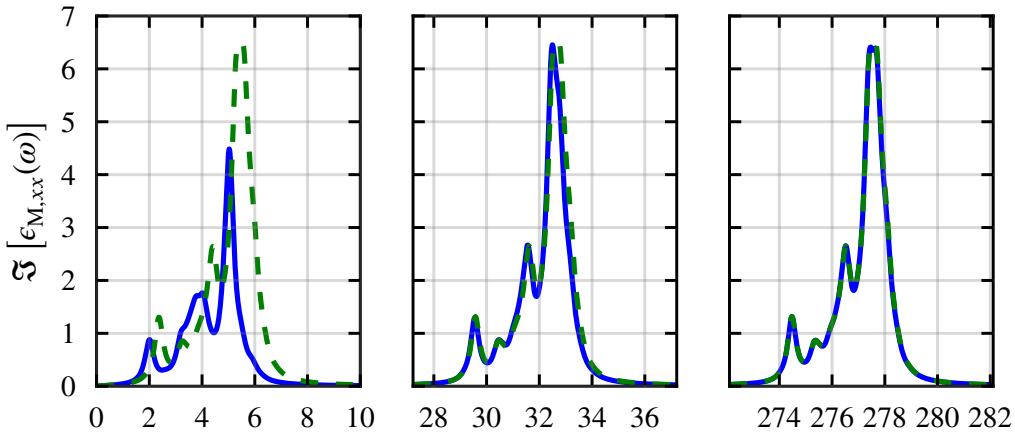

Figure 6.21.: Effect of artificially opening the band gap on the TDA and non-TDA BSE absorption spectra. Shown is the absorption spectra of naphthalene calculated with (dashed line) and without (solid line) the TDA for scissor energies of 0.0 eV, 27.2 eV and 272.1 eV (left to right).

Table 6.4.: Resonant and anti-resonant coupling measures for the considered materials and the maximal Coulomb matrix elements. The scissor shift was set to zero in the calculations for Si,C and LiF.

Material	$r_{\max}$	$a_{\max}$	$\lvert V^{\mathrm{rr}}\rvert_{\max}/E_{\mathrm{h}}$	$\lvert W^{\mathrm{rr}}\rvert_{\max}/E_{\mathrm{h}}$	$\lvert W^{\mathrm{r\bar{a}}}\rvert_{\max}/E_{\mathrm{h}}$
Si	3.4×10^{-2}	4.0×10^{-3}	1.7×10^{-3}	7.2×10^{-3}	1.1×10^{-3}
LiF	5.2×10^{-2}	5.3×10^{-4}	5.9×10^{-4}	3.0×10^{-2}	1.7×10^{-4}
2 A	1.0×10^{-1}	5.4×10^{-3}	1.4×10^{-3}	2.0×10^{-2}	2.5×10^{-4}
2 P	9.7×10^{-2}	6.4×10^{-3}	2.0×10^{-3}	2.0×10^{-2}	2.9×10^{-4}
2 T	1.1×10^{-1}	6.4×10^{-3}	1.2×10^{-3}	1.8×10^{-2}	2.2×10^{-4}

6.2.6. Computational details

The structural data for the naphthalene (2A) and bithiophene (2T) crystals was taken from the *Crystallography Open Database* [51–55] and originates from [56] and [57], respectively. For the biphenyl (2P) crystal the same structure as in [58] was used. The k-grids used in the BSE calculations where chosen such that a k-point density of 8 Å in each reciprocal lattice direction was achieved. The bands where chosen such that highest included

independent particle transition energy was about 12 eV. The resulting values are listed in table 6.5. For 2T this yielded the largest considered BSE matrix of size 119070×119070. The band structure paths of 2A and 2P were generated using the tools provided by the *pymatgen* library [59] which implements the k-path standards of [60]. For 2T a shortened, but representative path was chosen.

Table 6.5.: Number of occupied (valence) and unoccupied (conduction) bands included in the calculation of the optical absorption spectra

Material	occupied	unoccupied	k-grid
2 A	16	13	$8 \times 7 \times 7$
2 P	25	13	$9 \times 6 \times 5$
2 T	14	21	$6 \times 9 \times 7$

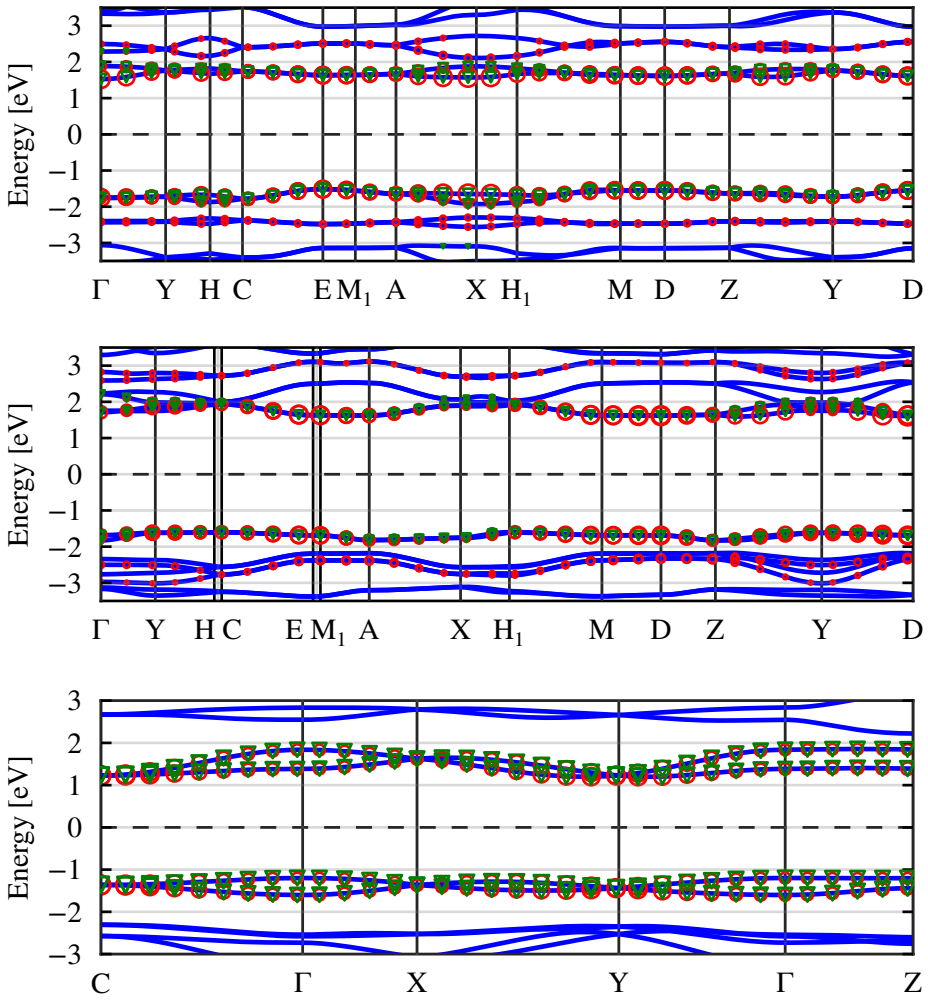

Figure 6.18.: Excitonic weights of the (top to bottom) naphthalene (2A), biphenyl (2P) and bithiophene (2T) crystals. The excitons with the largest anti-resonant contributions were chosen. The corresponding exciton energies are 1.83 eV (2A), 2.12 eV (2P) and 1.36 eV (2T). Shown are the resonant weights as red circles and the anti-resonant weights as green triangles. The latter are scaled by a factor of 10 w.r.t. the former. The weights have been linearly interpolated from the k-grid used in the BSE calculation onto the band structure path.

7. Conclusion and outlook

The BSE implementation of `exciting` was extended in two major ways: On the one hand, it is now possible to go beyond the commonly used TDA and include the coupling between resonant and anti-resonant transitions. On the other hand, the support for finite momentum transfer was added.

The diagonalization of the full non-hermitian BSE matrix was avoided following the approach of [9] which is about 50%-25% faster than that of the full diagonalization and allowed for the use of the well tested hermitian `ScaLapack` distributed memory eigen-solvers, making the BSE implementation fully scalable for cluster computing. For a considered momentum transfer of $\boldsymbol{q}_{\mathrm{mt}}$, the implementation shifts both valence and conduction states symmetrically around the reference k-point. As a result, the screening calculation needed to set up the screened Coulomb interaction becomes independent of the momentum transfer and needs to be calculated only once for the reference grid.

The EEL spectra for LiF and Si as well as the exciton band structure of LiF were calculated and are in good agreement with previously published results. The breakdown of the TDA for the EEL spectra of Si at $Q = 0$ as reported in [6] was also confirmed. The same behaviour was observed in the EEL spectra of both Si and LiF at $Q \neq 0$. This breakdown is due to the fact that the TDA fails to describe plasmonic excitations correctly. Similarly, the TDA was found to be inadequate for the description of the optical absorption spectra of the molecular crystals 2A, 2P, and 2T, confirming [41]. The large difference between the full BSE and TDA results for these materials is attributed to an interaction between the excitons and an energetically close plasmons which are not present in the TDA calculation. It was also observed that the anti-resonant BSE eigenvector components in these materials are considerably larger that in Si and LiF. These eigenvector components were also shown to be informative in the analysis of the excitonic band structure of 2A. To extract more information about the relevance of the anti-resonant eigenvector components, real space visualization routines for the full BSE solutions should be implemented in the future.

Measures for the importance of the BSE coupling terms were introduced, and the influence of the band gap on the coupling strength was investigated. In order to make definitive statements about the predictive power of these measures, more refined computations need to be conducted. The effect of artificially opening the band gap, however, clearly decouples the BSE yielding the TDA result. This indicates that there is probably no need to lift the TDA when the absorption spectrum of core excitations is considered. The loss spectrum, however might still show differences and should be investigated.

A. Bloch states

This appendix summarizes the well-known results of Bloch's theory of electrons in a periodic potential in appendices A.1 to A.3. In particular, the effect of the time reversal symmetry of the underlying Hamiltonian is discussed in appendix A.3.2.

A.1. Crystal lattices

We consider a solid as an infinite periodic assembly of ions. The crystalline structure is defined by the *real space lattice vectors* $\{\boldsymbol{R}\}$ that are spanned by all integer combinations of the corresponding *real space basis vectors* $\left\{\boldsymbol{a}_i\right\}$. The volume spanned by the basis vectors is the volume of the *unit cell* denoted as Ω. An associated *basis in reciprocal space* $\left\{\boldsymbol{b}_i\right\}$ is defined by

$$\boldsymbol{a}_i \cdot \boldsymbol{b}_j = 2\pi\delta_{i,j}. \tag{A.1}$$

Integer combinations of the reciprocal basis vectors define the *reciprocal lattice vectors* $\{\boldsymbol{G}\}$. Any point in reciprocal space can then be expressed as $\boldsymbol{k} = \boldsymbol{q} + \boldsymbol{G}$, where $\boldsymbol{q}$ is a vector within the *reciprocal unit cell*.

A.2. Electron in a perfect crystal

The common way to approach the quantum-mechanical description of a solid is to first consider one electron in a potential which is periodic with respect to translations along the lattice vectors $\{\boldsymbol{R}\}$

$$U(\boldsymbol{r} + \boldsymbol{R}) = U(\boldsymbol{r}). \tag{A.2}$$

The resulting Schrödinger-equation (neglecting spin) becomes

$$\hat{\mathrm{H}}\phi(\boldsymbol{r}) = \left[-\frac{1}{2}\nabla^2 + U(\boldsymbol{r})\right]\phi(\boldsymbol{r}) = \varepsilon\phi(\boldsymbol{r}). \tag{A.3}$$

Then, *Bloch's theorem* states that the eigenstates of eq. (A.3) are of the form

$$\phi_{n\boldsymbol{k}}(\boldsymbol{r}) = \mathrm{e}^{\mathrm{i}\boldsymbol{k}\boldsymbol{r}} u_{n\boldsymbol{k}}(\boldsymbol{r}), \tag{A.4}$$

where $u_{n\boldsymbol{k}}(\boldsymbol{r}) = u_{n\boldsymbol{k}}(\boldsymbol{r} + \boldsymbol{R})$ has the same periodicity as the potential [61]. Equation (A.4) define the so-called *Bloch states*, they are labeled by a, a priori, continuous wave-vector $\boldsymbol{k}$ and a discrete quantum index n.

A.2.1. Born-von Karman boundary condition

Instead of the infinite crystal, one usually defines a finite, but large volume commensurate with the primitive cell of the underlying Bravais lattice and considers the boundary condition

$$\phi(\boldsymbol{r} + N_i \boldsymbol{a}_i) = \phi(\boldsymbol{r}) \quad \text{for} \quad i = 1, 2, 3. \tag{A.5}$$

This is known as the *Born-von-Karman boundary condition* and

$$V = N_1 N_2 N_3 \Omega, \; N_i \in \mathbb{Z} \tag{A.6}$$

is the *Born-von-Karman volume*. Applying this condition restricts the continuous $\boldsymbol{k}$ to a discrete set defined by

$$\boldsymbol{k} = \sum_{i=1}^{3} \frac{m_i}{N_i} \boldsymbol{b}_i \quad \text{for} \quad m_i \in \mathbb{Z}. \tag{A.7}$$

In the following we will denote only the fractional part of eq. (A.7), i.e. the part within the reciprocal unit cell, with $\boldsymbol{k}$ and the integer part is described by a reciprocal lattice vector $\boldsymbol{G}$.

Using the BKB and the Bloch ansatz, the Schrödinger equation can be restated for each k-vector in the reciprocal unit cell in terms of the periodic part alone

$$\hat{\mathrm{H}}_{\boldsymbol{k}} u_{\boldsymbol{k}}(\boldsymbol{r}) = \left((-i\nabla + \boldsymbol{k})^2 + U(\boldsymbol{r})\right) u_{\boldsymbol{k}}(\boldsymbol{r}) = \varepsilon_{\boldsymbol{k}} u_{\boldsymbol{k}}(\boldsymbol{r}). \tag{A.8}$$

A.3. Properties of a Bloch wave

A.3.1. General properties

In the following we state the properties of a Bloch wave in a system with BKB conditions with respect to translations in $\boldsymbol{r}$ and $\boldsymbol{k}$ (see chap. 8 of ref. [61]). The Bloch functions satisfy

$$\phi_{n\boldsymbol{k}}(\boldsymbol{r} + \boldsymbol{R}) = \mathrm{e}^{\mathrm{i}\boldsymbol{k}\boldsymbol{R}} \phi_{n\boldsymbol{k}}(\boldsymbol{r}) \quad \text{and} \quad \phi_{n\boldsymbol{k}+\boldsymbol{G}}(\boldsymbol{r}) = \phi_{n\boldsymbol{k}}(\boldsymbol{r}), \tag{A.9}$$

while the periodic part behaves as

$$u_{n\boldsymbol{k}}(\boldsymbol{r} + \boldsymbol{R}) = u_{n\boldsymbol{k}}(\boldsymbol{r}) \quad \text{and} \quad u_{n\boldsymbol{k}+\boldsymbol{G}}(\boldsymbol{r}) = \mathrm{e}^{-\mathrm{i}\boldsymbol{G}\boldsymbol{r}} u_{n\boldsymbol{k}}(\boldsymbol{r}). \tag{A.10}$$

The eigenvalues do not change for different $\boldsymbol{G}$-components

$$\epsilon_{n\boldsymbol{k}+\boldsymbol{G}} = \epsilon_{n\boldsymbol{k}}. \tag{A.11}$$

Any function $f(\boldsymbol{r})$ can be used to construct a corresponding Bloch function by

$$f_{\boldsymbol{k}}^{\mathrm{Bloch}}(\boldsymbol{r}) = \sum_{\boldsymbol{R}} \mathrm{e}^{\mathrm{i}\boldsymbol{k}\boldsymbol{R}} f(\boldsymbol{r} - \boldsymbol{R}). \tag{A.12}$$

A.3.2. Time reversal symmetry

The Hamiltonian eq. (A.3) is invariant under *time reversal*. Time reversal is a discrete symmetry transformation given by *time reversal operator* $\hat{\mathrm{T}}$. For a spin-less electron $\hat{\mathrm{T}}$ is equal to the operator of the complex conjugation $\hat{\mathrm{C}}$ (see chap. 11.4 of ref. [62]):

$$\hat{\mathrm{T}} = \hat{\mathrm{C}} \quad \text{and} \quad \hat{\mathrm{T}}^{-1} = \hat{\mathrm{C}}. \tag{A.13}$$

Applying this transformation to the $\boldsymbol{k}$-dependent Hamiltonian of eq. (A.8) reveals a connection between the solutions at $\boldsymbol{k}$ and $-\boldsymbol{k}$, namely

$$\hat{\mathrm{T}}^{-1}\hat{\mathrm{H}}_{\boldsymbol{k}}\hat{\mathrm{T}} = \hat{\mathrm{H}}_{-\boldsymbol{k}}. \tag{A.14}$$

From this it follows that

$$\hat{\mathrm{H}}_{-\boldsymbol{k}}\left(\hat{\mathrm{T}}^{-1}u_{\boldsymbol{k}}\right) = \epsilon_{\boldsymbol{k}}\left(\hat{\mathrm{T}}^{-1}u_{\boldsymbol{k}}\right) \tag{A.15}$$

resulting in the useful relations

$$u_{n-\boldsymbol{k}} = u^{*}_{n\boldsymbol{k}} \leftrightarrow \phi_{n,-\boldsymbol{k}} = \phi^{*}_{n\boldsymbol{k}} \tag{A.16a}$$

and

$$\varepsilon_{\boldsymbol{k}} = \varepsilon_{-\boldsymbol{k}}. \tag{A.16b}$$

The spin-1/2 case

Though the present work does not deal with the explicit spin treatment, we will note here the behaviour of a non-relativistic spin-1/2-dependent $\hat{\mathrm{H}}_{\boldsymbol{k}}$ under time reversal. A usual approximate form derived from the Dirac equation is

$$\hat{\mathrm{H}} = \frac{1}{2}\hat{\boldsymbol{p}}^2 + U(\boldsymbol{r}) - \frac{1}{8}\hat{\boldsymbol{p}}^4 + \frac{1}{8}\nabla^2 U(\boldsymbol{r}) + \frac{1}{4}\left(\nabla U(\boldsymbol{r}) \times \hat{\boldsymbol{p}}\right)\sigma, \tag{A.17}$$

where σ is the "vector" of Pauli matrices. The corresponding Bloch Hamiltonian is

$$\hat{\mathrm{H}}_{\boldsymbol{k}} = \frac{1}{2}\left(\hat{\boldsymbol{p}} + \boldsymbol{k}\right)^2 + U(\boldsymbol{r}) - \frac{1}{8}\left(\hat{\boldsymbol{p}} + \boldsymbol{k}\right)^4 + \frac{1}{8}\nabla^2 U(\boldsymbol{r}) + \frac{1}{4}\left(\nabla U(\boldsymbol{r}) \times \left(\hat{\boldsymbol{p}} + \boldsymbol{k}\right)\right)\sigma. \tag{A.18}$$

The time reversal operator can then be defined as (see chap. 11.4.2.3 of ref. [62])

$$\hat{\mathrm{T}} = -\mathrm{i}\boldsymbol{\sigma}_y\hat{\mathrm{C}} \quad \text{and} \quad \hat{\mathrm{T}}^{-1} = \mathrm{i}\boldsymbol{\sigma}_y\hat{\mathrm{C}}, \tag{A.19}$$

where now also the Pauli matrix $\boldsymbol{\sigma}_y$

$$\boldsymbol{\sigma}_y = \begin{pmatrix} 0 & -\mathrm{i} \\ \mathrm{i} & 0 \end{pmatrix} \tag{A.20}$$

enters. It can then be shown that eqs. (A.14) and (A.15) are still valid for eq. (A.18). It then follows, that to each Bloch function at wave-vector $\boldsymbol{k}$

$$\Phi_{n\boldsymbol{k}}(\boldsymbol{r}) = \begin{pmatrix} \phi_{n\boldsymbol{k}\uparrow}(\boldsymbol{r}) \\ \phi_{n\boldsymbol{k}\downarrow}(\boldsymbol{r}) \end{pmatrix} = \mathrm{e}^{\mathrm{i}\boldsymbol{k}\boldsymbol{r}} \begin{pmatrix} u_{n\boldsymbol{k}\uparrow}(\boldsymbol{r}) \\ u_{n\boldsymbol{k}\downarrow}(\boldsymbol{r}) \end{pmatrix} \tag{A.21}$$

the Bloch function at wave-vector $-\boldsymbol{k}$ is related as

$$\Phi_{n-\boldsymbol{k}}(\boldsymbol{r}) = \begin{pmatrix} \phi_{n-\boldsymbol{k}\uparrow}(\boldsymbol{r}) \\ \phi_{n-\boldsymbol{k}\downarrow}(\boldsymbol{r}) \end{pmatrix} = \begin{pmatrix} \phi^*_{n\boldsymbol{k}\downarrow}(\boldsymbol{r}) \\ -\phi^*_{n\boldsymbol{k}\uparrow}(\boldsymbol{r}) \end{pmatrix} \tag{A.22}$$

while both are eigenstates to the same energy $\varepsilon_{n\boldsymbol{k}}$.

B. Lattice Fourier transformation

In this chapter the conventions for the Fourier transform in the context of a periodic crystal (lattice Fourier transform) are presented. They agree with the definitions given in [19, 25].

B.1. Local and non-local functions

The lattice Fourier transform of an arbitrary local function can be defined as

$$F_{\boldsymbol{G}}(\boldsymbol{q}) = \frac{1}{V}\int_V f(\boldsymbol{r})\,\mathrm{e}^{-\mathrm{i}(\boldsymbol{q}+\boldsymbol{G})\boldsymbol{r}}\,\mathrm{d}^3 r\,, \tag{B.1a}$$

and the corresponding inverse transform is given by

$$f(\boldsymbol{r}) = \sum_{\boldsymbol{q},\boldsymbol{G}} F_{\boldsymbol{G}}(\boldsymbol{q})\mathrm{e}^{\mathrm{i}(\boldsymbol{q}+\boldsymbol{G})\boldsymbol{r}}. \tag{B.1b}$$

Similarly, for a non-local function depending on two positions the lattice Fourier transform is chosen to be

$$F_{\boldsymbol{G}\boldsymbol{G}'}(\boldsymbol{q},\boldsymbol{q}') = \frac{1}{V}\iint \mathrm{d}^3 r\,\mathrm{d}^3 r'\,\mathrm{e}^{-\mathrm{i}(\boldsymbol{q}+\boldsymbol{G})\boldsymbol{r}} f(\boldsymbol{r},\boldsymbol{r}')\mathrm{e}^{\mathrm{i}(\boldsymbol{q}'+\boldsymbol{G}')\boldsymbol{r}'} \tag{B.2a}$$

and its inverse then given by

(B.2b)

$$f(\boldsymbol{r},\boldsymbol{r}') = \frac{1}{V}\sum_{\boldsymbol{q},\boldsymbol{G}}\sum_{\boldsymbol{q}',\boldsymbol{G}'} \mathrm{e}^{\mathrm{i}(\boldsymbol{q}+\boldsymbol{G})\boldsymbol{r}} f_{\boldsymbol{G},\boldsymbol{G}'}(\boldsymbol{q},\boldsymbol{q}')\mathrm{e}^{-\mathrm{i}(\boldsymbol{q}'+\boldsymbol{G}')\boldsymbol{r}'}. \tag{B.2c}$$

B.2. Periodic function

Formulas (B.1) and (B.2) simplify in the case that the functions are periodic with respect to a translation with a lattice vector.

For a local function satisfying $f(\boldsymbol{r}+\boldsymbol{R}) = f(\boldsymbol{r})$, only Fourier coefficients with $\boldsymbol{q} = 0$ will be non-vanishing.

$$\begin{aligned} f(\boldsymbol{r}) &= \frac{1}{V}\sum_{\boldsymbol{q}\boldsymbol{G}} F_{\boldsymbol{G}}(\boldsymbol{q})\mathrm{e}^{\mathrm{i}(\boldsymbol{q}+\boldsymbol{G})\boldsymbol{r}} \overset{!}{=} f(\boldsymbol{r}+\boldsymbol{R}) = \frac{1}{V}\sum_{\boldsymbol{q}\boldsymbol{G}} F_{\boldsymbol{G}}(\boldsymbol{q})\mathrm{e}^{\mathrm{i}(\boldsymbol{q}+\boldsymbol{G})\boldsymbol{r}}\mathrm{e}^{\mathrm{i}\boldsymbol{q}\boldsymbol{R}} \\ &= \frac{1}{V}\sum_{\boldsymbol{G}} F_{\boldsymbol{G}}(0)\mathrm{e}^{\mathrm{i}\boldsymbol{G}\boldsymbol{r}} \end{aligned} \tag{B.3}$$

A consequence is that the integral

$$\begin{aligned}\int \mathrm{d}r\, f(\boldsymbol{r})\mathrm{e}^{-\mathrm{i}\boldsymbol{K}\boldsymbol{r}} &= \frac{1}{V}\sum_{\boldsymbol{G}} f(0,\boldsymbol{G}) \int \mathrm{d}r\, \mathrm{e}^{\mathrm{i}(\boldsymbol{G}-\boldsymbol{K})\boldsymbol{r}} \\ &= \frac{1}{V}\sum_{\boldsymbol{G}} f(0,\boldsymbol{G})\delta_{\boldsymbol{G},\boldsymbol{K}} V = \sum_{\boldsymbol{G}} f(0,\boldsymbol{G})\delta_{\boldsymbol{G},\boldsymbol{K}} \\ &= f(0,\boldsymbol{K})\end{aligned} \tag{B.4}$$

is only non-vanishing if $\boldsymbol{K}$ is a reciprocal lattice vector. In a similar fashion it can be shown that the lattice Fourier transform of a non-local function satisfying $f(\boldsymbol{r}+\boldsymbol{R},\boldsymbol{r}'+\boldsymbol{R}) = f(\boldsymbol{r},\boldsymbol{r}')$ only depends on one $\boldsymbol{q}$ variable instead of two

$$\begin{aligned} f(\boldsymbol{r},\boldsymbol{r}') &= \frac{1}{V}\sum_{\boldsymbol{q},\boldsymbol{G}}\sum_{\boldsymbol{q}',\boldsymbol{G}'} \mathrm{e}^{\mathrm{i}(\boldsymbol{q}+\boldsymbol{G})\boldsymbol{r}} F_{\boldsymbol{G}\boldsymbol{G}'}(\boldsymbol{q},\boldsymbol{q}')\mathrm{e}^{-\mathrm{i}(\boldsymbol{q}'+\boldsymbol{G}')\boldsymbol{r}'} \\ \overset{!}{=} f(\boldsymbol{r}+\boldsymbol{R},\boldsymbol{r}'+\boldsymbol{R}) &= \frac{1}{V}\sum_{\boldsymbol{q},\boldsymbol{G}}\sum_{\boldsymbol{q}',\boldsymbol{G}'} \mathrm{e}^{\mathrm{i}(\boldsymbol{q}+\boldsymbol{G})\boldsymbol{r}} F_{\boldsymbol{G}\boldsymbol{G}'}(\boldsymbol{q},\boldsymbol{q}')\mathrm{e}^{-\mathrm{i}(\boldsymbol{q}'+\boldsymbol{G}')\boldsymbol{r}'}\mathrm{e}^{\mathrm{i}(\boldsymbol{q}-\boldsymbol{q}')\boldsymbol{R}} \\ &= \frac{1}{V}\sum_{\boldsymbol{q}}\sum_{\boldsymbol{G},\boldsymbol{G}'} \mathrm{e}^{\mathrm{i}(\boldsymbol{q}+\boldsymbol{G})\boldsymbol{r}} F_{\boldsymbol{G}\boldsymbol{G}'}(\boldsymbol{q},\boldsymbol{q})\mathrm{e}^{-\mathrm{i}(\boldsymbol{q}+\boldsymbol{G}')\boldsymbol{r}'}. \end{aligned} \tag{B.5}$$

B.3. Fourier transform in time

The Fourier transform between the time and (angular) frequency domain is chosen to be

$$F(\omega) = \int f(t)\mathrm{e}^{\mathrm{i}\omega t}\,\mathrm{d}t \tag{B.6a}$$

with the corresponding inverse transform

$$f(t) = \frac{1}{2\pi}\int F(\omega)\mathrm{e}^{-\mathrm{i}\omega t}\,\mathrm{d}\omega\,. \tag{B.6b}$$

C. The (L)APW+lo basis

Exciting employs the *augmented plane wave* method (APW) in which the unit cell is partitioned into spherical regions centered around each atom, the so called *muffin-tins*, and an interstitial region. Within the interstitial region plane waves are used as basis functions, while atomic-like functions are used inside the muffin-tins. Each augmented plane wave is thus defined as

$$\phi^{\mathrm{apw}}_{\boldsymbol{k}+\boldsymbol{G}}(\boldsymbol{r}) = \begin{cases} \dfrac{1}{\sqrt{V}} \mathrm{e}^{\mathrm{i}(\boldsymbol{k}+\boldsymbol{G})\boldsymbol{r}} & , \boldsymbol{r} \in \text{interstitial} \\ \displaystyle\sum_{\alpha,l,m} f^{\alpha,lm}_{\boldsymbol{k}+\boldsymbol{G}}(r_\alpha) Y_{lm}(\hat{\boldsymbol{r}}_\alpha) & , \boldsymbol{r} \in \text{muffin-tin} \end{cases}. \tag{C.1}$$

Here, $\boldsymbol{r}_\alpha = \boldsymbol{r} - \boldsymbol{R}_\alpha$ and $\boldsymbol{R}_\alpha$ is the center of the muffin-tin sphere around atom α. The coefficients $f^{\alpha,lm}_{\boldsymbol{k}+\boldsymbol{G}}(r_\alpha)$ are given in terms the of real-valued radial functions $u^\alpha_{lp}(r_\alpha, E_l)$ and the matching coefficients $A^\alpha_{lmp}(\boldsymbol{k}+\boldsymbol{G})$:

$$f^{\alpha,lm}_{\boldsymbol{k}+\boldsymbol{G}}(r_\alpha) = \sum_{p=0}^{p_{\max}} A^\alpha_{lmp}(\boldsymbol{k}+\boldsymbol{G}) u^\alpha_{lp}(r_\alpha, E_l). \tag{C.2}$$

Within the muffin-tin regions the Kohn-Sham potential is assumed to be spherically symmetric and the *radial wave function* $u^\alpha_l(r_\alpha, E_l)$ is calculated by the radial, scalar-relativistic Schrödinger equation for a fixed *linearization energy* E_l [63]. The radial functions $u^\alpha_{lp}(r_\alpha, E_l)$ are the p-th energy derivate of the radial wave functions and taking $p_{\max} = 1$ yields the so-called *linearized augmented plane wave* method (LAPW). The matching coefficients are chosen such that the basis functions are continuous up to the order $p_{\max}$.

In addition to the APW functions exciting supports so-called *local orbitals*, which are atomic-like functions within the muffin-tins

$$\phi^{\mathrm{lo}}_L(\boldsymbol{r}) = \begin{cases} 0 & , \boldsymbol{r} \in \text{interstitial} \\ v^\alpha_L(r_\alpha) Y_{lm}(\hat{\boldsymbol{r}}_\alpha) & , \boldsymbol{r} \in \text{muffin-tin of atom } \alpha. \end{cases} \tag{C.3}$$

The $v^\alpha_L(r_\alpha)$ are also combinations of the radial functions $u^\alpha_{lp}(r_\alpha, E_b)$ and matching coefficients A^α_b

$$v^\alpha_L(r) = \sum_{b=0}^{p_{\max}} A^\alpha_b u^\alpha_{lp_b}(r, E_b). \tag{C.4}$$

The matching coefficients are chosen such that the derivatives of the local orbital are zero up to the $(p_{\max} - 1)$-th order and such that it is normalized within the muffin-tin. Mathematically, a Bloch basis function is constructed from each local orbital according to

$$\phi^{\mathrm{lo}}_{\boldsymbol{k},L}(\boldsymbol{r}) = \sum_{\boldsymbol{R}} \mathrm{e}^{\mathrm{i}\boldsymbol{R}\boldsymbol{k}} \phi^{\mathrm{lo}}_L(\boldsymbol{r} - \boldsymbol{R}), \tag{C.5}$$

but in practice only integrals over the first unit cell are calculated in which case only eq. (C.3) is needed. Here, the index L contains the indices $\{l, m, \alpha\}$ and the matching order $p_{\max}$. With the inclusion of local orbitals the overall flexibility of the basis set is increased, especially with respect to the description of low lying semi-core states. The expansion of the Bloch wave functions within the (L)APW+lo basis is thus

$$\phi_{n\boldsymbol{k}}(\boldsymbol{r}) = \sum_{\boldsymbol{G}} c_{n\boldsymbol{k}+\boldsymbol{G}} \phi^{\mathrm{apw}}_{\boldsymbol{k}+\boldsymbol{G}} + \sum_{L} c_{n\boldsymbol{k},L} \phi^{\mathrm{lo}}_{\boldsymbol{k},L}(\boldsymbol{r}). \tag{C.6}$$

D. Plane-wave matrix elements

The key quantity to compute for the setup of the BSE Hamiltonian are the plane-wave matrix elements (PWE) $M_{mn\boldsymbol{k}}(\boldsymbol{G}, \boldsymbol{q})$, as seen in section 4.3. In the following, we first note some of their general properties in appendix D.1, then discuss the optical limit in appendix D.2, and go into detail about how they are computed in the (L)APW+lo basis set in appendix D.3.

D.1. General properties

The matrix elements of a (non-normalized) plane wave and two Bloch states (neglecting spin) can be written as

$$\left\langle f\boldsymbol{k}_f \middle| \mathrm{e}^{-\mathrm{i}(\boldsymbol{G}+\boldsymbol{q})\boldsymbol{r}} \middle| i\boldsymbol{k}_i \right\rangle = \delta_{\left\lfloor \boldsymbol{k}_f - \boldsymbol{k}_i + \boldsymbol{q} \right\rfloor_{1^{\text{st}}\,\text{BZ}}, 0}\, M_{fi\boldsymbol{k}_f}(\boldsymbol{G}, \boldsymbol{q}), \tag{D.1}$$

where $\delta_{\left\lfloor \boldsymbol{k}_f - \boldsymbol{k}_i + \boldsymbol{q} \right\rfloor_{1^{\text{st}}\,\text{BZ}}, 0}$ denotes that the element is only non-zero if $\boldsymbol{k}_i = \boldsymbol{k}_f + \boldsymbol{q}$ apart from some reciprocal lattice vector. From the definition above it follows directly that

$$M_{fi\boldsymbol{k}_f}(\boldsymbol{G}, \boldsymbol{q}) = M^*_{if\boldsymbol{k}_i}(-\boldsymbol{G}, -\boldsymbol{q}). \tag{D.2}$$

Using the time reversal symmetry of the Bloch states $|i - \boldsymbol{k}\rangle = \left|(i\boldsymbol{k})^*\right\rangle$, the identity

$$M_{fi\boldsymbol{k}_f}(\boldsymbol{G}, \boldsymbol{q}) = M_{if-\boldsymbol{k}_i}(\boldsymbol{G}, \boldsymbol{q}) \tag{D.3}$$

is found.

D.2. Optical limit of the plane wave matrix elements

In order to take the limit $\boldsymbol{q} \to 0$ of the plane-wave matrix element $\langle f\boldsymbol{k}_\mathrm{f} \left| \mathrm{e}^{-\mathrm{i}(\boldsymbol{G}+\boldsymbol{q})\boldsymbol{r}} \right| i\boldsymbol{k}_\mathrm{f} + \boldsymbol{q}\rangle$ at $\boldsymbol{G} = 0$ some care has to be taken. The expansion for small $\boldsymbol{q}$ is given by

$$\begin{aligned}
\langle f\boldsymbol{k}_\mathrm{f} \left| \mathrm{e}^{-\mathrm{i}\boldsymbol{q}\boldsymbol{r}} \right| i\boldsymbol{k}_\mathrm{f} + \boldsymbol{q}\rangle &= \langle f\boldsymbol{k}_\mathrm{f}| \, 1 - \mathrm{i}\boldsymbol{q}\boldsymbol{r} + \ldots \left(\left| i\boldsymbol{k}_\mathrm{f}\right\rangle + \boldsymbol{q}\nabla_{\boldsymbol{k}} \left| i\boldsymbol{k}\right\rangle |_{\boldsymbol{k}_\mathrm{f}} + \ldots \right) \\
&= \delta_{fi} + \mathrm{i}\boldsymbol{q} \langle f\boldsymbol{k}_\mathrm{f} \left| -\boldsymbol{r} \right| i\boldsymbol{k}_\mathrm{f}\rangle + \boldsymbol{q} \langle f\boldsymbol{k}_\mathrm{f}| \left(\nabla_{\boldsymbol{k}} \left| i\boldsymbol{k}\right\rangle \right)_{\boldsymbol{k}_\mathrm{f}} + O(\boldsymbol{q}^2). \\
&\approx \delta_{fi} + \mathrm{i}\boldsymbol{q} \langle f\boldsymbol{k}_\mathrm{f} \left| -\boldsymbol{r} \right| i\boldsymbol{k}_\mathrm{f}\rangle
\end{aligned} \tag{D.4}$$

If the potential part of the one-particle Hamiltonian is *local*, the usual canonical commutation relations hold

$$\left[\hat{\mathrm{r}}_i, \hat{\mathrm{p}}_j\right] = \mathrm{i}\delta_{ij} \tag{D.5a}$$

$$\left[\hat{\mathrm{h}}, \hat{\boldsymbol{r}}\right] = -\mathrm{i}\hat{\boldsymbol{p}}, \tag{D.5b}$$

which enable us to express the $\boldsymbol{r}$ expectation value in (D.4) in terms of momentum matrix elements

$$\langle f\boldsymbol{k}_\mathrm{f}\big|-\boldsymbol{r}\big|i\boldsymbol{k}_\mathrm{f}\rangle = \mathrm{i}\frac{\langle f\boldsymbol{k}_\mathrm{f}\big|\boldsymbol{p}\big|i\boldsymbol{k}_\mathrm{f}\rangle}{\epsilon_{f\boldsymbol{k}_\mathrm{f}} - \epsilon_{i\boldsymbol{k}_\mathrm{f}}} =: \boldsymbol{D}_{fi\boldsymbol{k}_\mathrm{f}}. \tag{D.6}$$

The $\boldsymbol{D}_{fi\boldsymbol{k}_\mathrm{f}}$ are the dipole operator matrix elements for electronic transitions. Plugging (D.6) into (D.4) yields

$$M_{fi\boldsymbol{k}_\mathrm{f}}(0,\boldsymbol{q}) \overset{q\ll 1}{=} \delta_{fi} + \mathrm{i}\boldsymbol{q}^\mathrm{T}\boldsymbol{D}_{fi\boldsymbol{k}_\mathrm{f}}(1-\delta_{fi}). \tag{D.7}$$

D.3. Computation in the (L)APW+lo basis

The expressions for the PEWs in terms of the (L)APW+lo basis functions are documented in detail in Ref. [20], chapter 8.2. In the following, we note the main results and subsequently point out necessary changes to compute the modified plane-wave matrix elements $N_{mn\boldsymbol{k}}(\boldsymbol{G},\boldsymbol{q})$ (4.43) needed for the construction of the coupling block of the screened Coulomb interaction (4.42).

D.3.1. Plane-wave matrix elements

In terms of the (L)APW+lo basis functions [see eqs. (C.1), (C.3) and (C.6)] the element

$$M_{nm\boldsymbol{k}'}(\boldsymbol{G},\boldsymbol{q}) = \langle\phi_{n\boldsymbol{k}'}\big|\mathrm{e}^{-\mathrm{i}(\boldsymbol{G}+\boldsymbol{q})\boldsymbol{r}}\big|\phi_{m\boldsymbol{k}''}\rangle\,\delta_{\lfloor\boldsymbol{k}'-\boldsymbol{k}''+\boldsymbol{q}\rfloor_{1^{\mathrm{st}}\,\mathrm{BZ}},0} \tag{D.8}$$

can be written as

$$\begin{aligned} M_{nm\boldsymbol{k}'}(\boldsymbol{G},\boldsymbol{q})/N_{\boldsymbol{k}} = &\sum_{\boldsymbol{G}'\boldsymbol{G}''} c^*_{n\boldsymbol{k}'+\boldsymbol{G}'} c_{m\boldsymbol{k}''+\boldsymbol{G}''} M_{\boldsymbol{G}'\boldsymbol{G}''\boldsymbol{k}'}(\boldsymbol{G},\boldsymbol{q}) \\ &+ \sum_{\boldsymbol{G}'L''} c^*_{n\boldsymbol{k}'+\boldsymbol{G}'} c_{m\boldsymbol{k}'',L''} M_{\boldsymbol{G}'L''\boldsymbol{k}'}(\boldsymbol{G},\boldsymbol{q}) \\ &+ \sum_{L'\boldsymbol{G}''} c^*_{n\boldsymbol{k}',L'} c_{m\boldsymbol{k}''+\boldsymbol{G}''} M_{L'\boldsymbol{G}''\boldsymbol{k}'}(\boldsymbol{G},\boldsymbol{q}) \\ &+ \sum_{L'L''} c^*_{n\boldsymbol{k}',L'} c_{m\boldsymbol{k}'',L''} M_{L'L''\boldsymbol{k}'}(\boldsymbol{G},\boldsymbol{q}) \end{aligned}, \tag{D.9}$$

where the integrals over the unit cell between the two types of basis functions are

$$M_{\boldsymbol{G}'\boldsymbol{G}''\boldsymbol{k}'}(\boldsymbol{G},\boldsymbol{q}) = \left\langle\phi_{\boldsymbol{k}'+\boldsymbol{G}'}\big|\mathrm{e}^{-\mathrm{i}(\boldsymbol{G}+\boldsymbol{q})\boldsymbol{r}}\big|\phi_{\boldsymbol{k}''+\boldsymbol{G}''}\right\rangle_\Omega \tag{D.10a}$$

$$M_{\boldsymbol{G}'L''\boldsymbol{k}'}(\boldsymbol{G},\boldsymbol{q}) = \left\langle\phi_{\boldsymbol{k}'+\boldsymbol{G}'}\big|\mathrm{e}^{-\mathrm{i}(\boldsymbol{G}+\boldsymbol{q})\boldsymbol{r}}\big|\phi_{\boldsymbol{k}'',L''}\right\rangle_\Omega \tag{D.10b}$$

$$M_{L'\boldsymbol{G}''\boldsymbol{k}'}(\boldsymbol{G},\boldsymbol{q}) = \left\langle\phi_{\boldsymbol{k}',L'}\big|\mathrm{e}^{-\mathrm{i}(\boldsymbol{G}+\boldsymbol{q})\boldsymbol{r}}\big|\phi_{\boldsymbol{k}''+\boldsymbol{G}''}\right\rangle_\Omega \tag{D.10c}$$

$$M_{L'L''\boldsymbol{k}'}(\boldsymbol{G},\boldsymbol{q}) = \left\langle \phi_{\boldsymbol{k}',L'} \middle| \mathrm{e}^{-\mathrm{i}(\boldsymbol{G}+\boldsymbol{q})\boldsymbol{r}} \middle| \phi_{\boldsymbol{k}'',L''} \right\rangle_{\Omega}. \tag{D.10d}$$

The integrals above can be split into two contribution, stemming from the interstitial and the muffin-tin part of the unit cell

$$M_{ab\boldsymbol{k}}(\boldsymbol{G},\boldsymbol{q}) = M^{\mathrm{I}}_{ab\boldsymbol{k}}(\boldsymbol{G},\boldsymbol{q}) + M^{\mathrm{MT}}_{ab\boldsymbol{k}}(\boldsymbol{G},\boldsymbol{q}), \tag{D.11}$$

where $a, b \in \left\{\boldsymbol{G}', \boldsymbol{G}'', L', L''\right\}$. In the interstitial region, only the plane-wave part of the APW functions is non-zero, so that only $M^{\mathrm{I}}_{\boldsymbol{G}'\boldsymbol{G}''\boldsymbol{k}'}(\boldsymbol{G},\boldsymbol{q})$ needs to be calculated. Using the lattice-theta function $\Theta_{\mathrm{I}}(\boldsymbol{r})$

$$\Theta_{\mathrm{I}}(\boldsymbol{r}) = \begin{cases} 1 & , \boldsymbol{r} \in \text{interstitial} \\ 0 & , \text{else} \end{cases}, \tag{D.12}$$

it is given by

$$\begin{aligned} M^{\mathrm{I}}_{\boldsymbol{G}'\boldsymbol{G}''\boldsymbol{k}'}(\boldsymbol{G},\boldsymbol{q}) &= \frac{1}{\Omega}\int_{\Omega} \Theta_{\mathrm{I}}(\boldsymbol{r}) \mathrm{e}^{-\mathrm{i}(\boldsymbol{k}'+\boldsymbol{G}')\boldsymbol{r}} \mathrm{e}^{-\mathrm{i}(\boldsymbol{q}+\boldsymbol{G})\boldsymbol{r}} \mathrm{e}^{\mathrm{i}(\boldsymbol{k}''+\boldsymbol{G}'')\boldsymbol{r}} \,\mathrm{d}^3\boldsymbol{r} \\ &= \frac{1}{\Omega}\int_{\Omega} \Theta_{\mathrm{I}}(\boldsymbol{r}) \mathrm{e}^{-\mathrm{i}(\boldsymbol{G}'-\boldsymbol{G}''+\boldsymbol{G})\boldsymbol{r}} \,\mathrm{d}^3\boldsymbol{r} = \tilde{\Theta}_{\mathrm{I}}(\boldsymbol{G}'-\boldsymbol{G}''+\boldsymbol{G}), \end{aligned} \tag{D.13}$$

where $\tilde{\Theta}_{\mathrm{I}}$ is the lattice Fourier transform of Θ_{I}. In the muffin-tin regions all four integrals eq. (D.10) are non-vanishing. After expanding the exponential $\mathrm{e}^{-\mathrm{i}(\boldsymbol{q}+\boldsymbol{G})\boldsymbol{r}}$ in terms of spherical harmonics Y_{lm} and spherical Bessel functions of first kind j_l according to

$$\mathrm{e}^{-\mathrm{i}(\boldsymbol{q}+\boldsymbol{G})\boldsymbol{r}} = 4\pi \sum_{lm} (-i)^l j_l(|\boldsymbol{q}+\boldsymbol{G}|r) Y_{lm}(\hat{\boldsymbol{r}}) Y^*_{lm}(\widehat{\boldsymbol{q}+\boldsymbol{G}}), \tag{D.14}$$

the APW-APW elements are found to be

$$\begin{aligned} M^{\mathrm{MT}}_{\boldsymbol{G}'\boldsymbol{G}''\boldsymbol{k}'}(\boldsymbol{G},\boldsymbol{q}) = 4\pi \sum_{\alpha} \mathrm{e}^{-\mathrm{i}(\boldsymbol{G}+\boldsymbol{q})\boldsymbol{R}_\alpha} \sum_{l'm'p'} \left(A^{\alpha}_{l'm'p'}(\boldsymbol{k}'+\boldsymbol{G}')\right)^* \\ \times \sum_{l''m''p''} A^{\alpha}_{l''m''p''}(\boldsymbol{k}''+\boldsymbol{G}'') X^{\alpha}_{l'm'p',l''m''p''}(\boldsymbol{q}+\boldsymbol{G}), \end{aligned} \tag{D.15a}$$

where X and R are auxiliary quantities defined as

$$X^{\alpha}_{l'm'p',l''m''p''}(\boldsymbol{q}+\boldsymbol{G}) = \sum_l (-\mathrm{i})^l R^{\alpha}_{l'p',l''p'',l}(\boldsymbol{q}+\boldsymbol{G}) \sum_m Y^*_{lm}(\widehat{\boldsymbol{q}+\boldsymbol{G}}) C^{l'm'}_{lm,l''m''} \tag{D.15b}$$

and

$$R^{\alpha}_{l'p',l''p'',l}(\boldsymbol{q}+\boldsymbol{G}) = \int_0^{R^{\mathrm{MT}}_{\alpha}} u^{\alpha}_{l'p'}(r) j_l(|\boldsymbol{q}+\boldsymbol{G}|r) u^{\alpha}_{l''p''}(r) r^2 \,\mathrm{d}r\,. \tag{D.15c}$$

Here, the C are the so-called Gaunt coefficients

$$C^{l'm'}_{lm,l''m''} = \iint Y^*_{l'm'}(\hat{\boldsymbol{r}}) Y_{lm}(\hat{\boldsymbol{r}}) Y_{l''m''}(\hat{\boldsymbol{r}}) \,\mathrm{d}\Omega\,. \tag{D.16}$$

The APW-LO matrix elements are given by

$$M^{\mathrm{MT}}_{\boldsymbol{G}'L''\boldsymbol{k}}(\boldsymbol{G},\boldsymbol{q}) = 4\pi \sum_{\alpha} \mathrm{e}^{-\mathrm{i}(\boldsymbol{G}+\boldsymbol{q})\boldsymbol{R}_\alpha} \sum_{l'm'p'} \left(A^{\alpha}_{l'm'p'}(\boldsymbol{k}'+\boldsymbol{G}')\right)^* X^{\alpha}_{l'm'p',L''}(\boldsymbol{q}+\boldsymbol{G}), \quad \text{(D.17a)}$$

with

$$X^{\alpha}_{l'm'p',L''}(\boldsymbol{q}+\boldsymbol{G}) = \sum_{l} (-\mathrm{i})^l R^{\alpha}_{l'p',L'',l}(\boldsymbol{q}+\boldsymbol{G}) \sum_{m} Y^*_{lm}(\widehat{\boldsymbol{q}+\boldsymbol{G}}) C^{l'm'}_{lm,l''m''} \quad \text{(D.17b)}$$

and

$$R^{\alpha}_{l'p',L'',l}(\boldsymbol{q}+\boldsymbol{G}) = \delta_{\alpha,\alpha''} \int_0^{R^{\mathrm{MT}}_\alpha} u^{\alpha}_{l'p'}(r) j_l(|\boldsymbol{q}+\boldsymbol{G}|r) v^{\alpha}_{L''}(r) r^2 \,\mathrm{d}r\,. \quad \text{(D.17c)}$$

Lastly, the LO-LO matrix elements are computed using

$$M^{\mathrm{MT}}_{L'L''\boldsymbol{k}'}(\boldsymbol{G},\boldsymbol{q}) = 4\pi \sum_{\alpha} \mathrm{e}^{-\mathrm{i}(\boldsymbol{G}+\boldsymbol{q})\boldsymbol{R}_\alpha} X^{\alpha}_{L',L''}(\boldsymbol{q}+\boldsymbol{G}), \quad \text{(D.18a)}$$

with

$$X^{\alpha}_{L',L''}(\boldsymbol{q}+\boldsymbol{G}) = \sum_{l} (-\mathrm{i})^l R^{\alpha}_{L',L'',l}(\boldsymbol{q}+\boldsymbol{G}) \sum_{m} Y^*_{lm}(\widehat{\boldsymbol{q}+\boldsymbol{G}}) C^{l'm'}_{lm,l''m''} \quad \text{(D.18b)}$$

and

$$R^{\alpha}_{L',L'',l}(\boldsymbol{q}+\boldsymbol{G}) = \delta_{\alpha,\alpha'}\delta_{\alpha,\alpha''} \int_0^{R^{\mathrm{MT}}_\alpha} v^{\alpha}_{L'}(r) j_l(|\boldsymbol{q}+\boldsymbol{G}|r) v^{\alpha}_{L''}(r) r^2 \,\mathrm{d}r\,. \quad \text{(D.18c)}$$

D.3.2. Modified plane-wave matrix elements

In order to calculate the modified plane-wave matrix elements

$$N_{nm\boldsymbol{k}'}(\boldsymbol{G},\boldsymbol{q}) = \left\langle \phi_{n\boldsymbol{k}'} \middle| \mathrm{e}^{-\mathrm{i}(\boldsymbol{G}+\boldsymbol{q})\boldsymbol{r}} \middle| \left(\phi_{m\boldsymbol{k}''}\right)^* \right\rangle \delta_{\lfloor \boldsymbol{k}'+\boldsymbol{k}''+\boldsymbol{q} \rfloor_{1^{\mathrm{st}}\,\mathrm{BZ}},0} \quad \text{(D.19)}$$

we need first to express the complex conjugate of the basis functions. Using the property of the spherical harmonics $Y^*_{lm}(\varphi,\theta) = (-1)^m Y_{l-m}(\varphi,\theta)$, we get

$$\phi^{\mathrm{apw}*}_{\boldsymbol{k}+\boldsymbol{G}}(\boldsymbol{r}) = \begin{cases} \dfrac{1}{\sqrt{V}} \mathrm{e}^{-\mathrm{i}(\boldsymbol{k}+\boldsymbol{G})\boldsymbol{r}} & , \boldsymbol{r} \in \text{interstitial} \\ \displaystyle\sum_{\alpha,l,m} \sum_{p=0}^{p_{\max}} A^{\alpha *}_{lmp}(\boldsymbol{k}+\boldsymbol{G}) u^{\alpha}_{lp}(r_\alpha, E_l)(-1)^m Y_{l-m}(\hat{\boldsymbol{r}}_\alpha) & , \boldsymbol{r} \in \text{muffin-tin} \end{cases} \quad \text{(D.20)}$$

for the APW basis functions, and

$$\phi^{\mathrm{lo}*}_{L}(\boldsymbol{r}) = \begin{cases} 0 & , \boldsymbol{r} \in \text{interstitial} \\ v^{\alpha}_{L}(r_\alpha)(-1)^m Y_{l-m}(\hat{\boldsymbol{r}}_\alpha) & \boldsymbol{r} \in \text{muffin-tin of atom } \alpha. \end{cases} \quad \text{(D.21)}$$

for the local orbitals. In analogy to eq. (D.9) it is

$$N_{nm\boldsymbol{k}'}(\boldsymbol{G},\boldsymbol{q})/N_{\boldsymbol{k}} = \sum_{a\neq b} c^*_{n,a} c^*_{m,b} N_{ab\boldsymbol{k}'}(\boldsymbol{G},\boldsymbol{q}), \tag{D.22}$$

where again $a, b \in \left\{\boldsymbol{G}', \boldsymbol{G}'', L', L''\right\}$. The interstitial part (D.13) simply changes to

$$N^{\mathrm{I}}_{\boldsymbol{G}'\boldsymbol{G}''\boldsymbol{k}'}(\boldsymbol{G},\boldsymbol{q}) = \tilde{\Theta}_{\mathrm{I}}(\boldsymbol{G}' + \boldsymbol{G}'' + \boldsymbol{G}), \tag{D.23}$$

while the muffin-tin contributions (D.15a), (D.17a) and (D.18a) change according to

$$\begin{aligned} N^{\mathrm{MT}}_{\boldsymbol{G}'\boldsymbol{G}''\boldsymbol{k}'}(\boldsymbol{G},\boldsymbol{q}) = 4\pi \sum_{\alpha} \mathrm{e}^{-\mathrm{i}(\boldsymbol{G}+\boldsymbol{q})\boldsymbol{R}_\alpha} \sum_{l'm'p'} \left(A^\alpha_{l'm'p'}(\boldsymbol{k}' + \boldsymbol{G}')\right)^* \\ \times \sum_{l''m''p''} \left(A^\alpha_{l''m''p''}(\boldsymbol{k}'' + \boldsymbol{G}'')\right)^* (-1)^{m''} X^\alpha_{l'm'p',l''-m''p''}(\boldsymbol{q}+\boldsymbol{G}), \end{aligned} \tag{D.24a}$$

$$\begin{aligned} N^{\mathrm{MT}}_{\boldsymbol{G}'L''\boldsymbol{k}}(\boldsymbol{G},\boldsymbol{q}) = 4\pi \sum_{\alpha} \mathrm{e}^{-\mathrm{i}(\boldsymbol{G}+\boldsymbol{q})\boldsymbol{R}_\alpha} \sum_{l'm'p'} \left(A^\alpha_{l'm'p'}(\boldsymbol{k}' + \boldsymbol{G}')\right)^* \\ (-1)^{m''} X^\alpha_{l'm'p',L''(-m'')}(\boldsymbol{q}+\boldsymbol{G}), \end{aligned} \tag{D.24b}$$

and

$$N^{\mathrm{MT}}_{L'L''\boldsymbol{k}'}(\boldsymbol{G},\boldsymbol{q}) = 4\pi \sum_{\alpha} \mathrm{e}^{-\mathrm{i}(\boldsymbol{G}+\boldsymbol{q})\boldsymbol{R}_\alpha} (-1)^{m''} X^\alpha_{L',L''(-m'')}(\boldsymbol{q}+\boldsymbol{G}) \tag{D.24c}$$

respectively.

E. Dielectric response of a Kohn-Sham system

In this chapter we describe the dielectric response of a Kohn-Sham system. An expression for the dielectric matrix is derived which serves as a starting point for the BSE formalism.

E.1. Linearization of the Liouville-von-Neumann equation

For a system of independent particles, as described by the Kohn-Sham equations (3.7), the longitudinal dielectric function can be derived using the equation of motion for the density matrix operator $\hat{\rho}$ (see [12, 64]) and the procedure is sketched in the following. The time-dependent Kohn-Sham Hamiltonian including the perturbing potential can be written in terms of the unperturbed Hamiltonian plus the total perturbing effective potential as

$$\hat{\mathrm{h}}_{\mathrm{KS}}(t) = \hat{\mathrm{h}}^{(0)}_{\mathrm{KS}} + \delta V_{\mathrm{eff}}(t) = \hat{\mathrm{h}}^{(0)}_{\mathrm{KS}} + V_{\mathrm{ext}}(t) + \delta V_{\mathrm{H}}(t) + \delta V_{\mathrm{xc}}(t) \tag{E.1}$$

and the corresponding Schrödinger equation reads

$$\mathrm{i}\frac{\mathrm{d}}{\mathrm{d}t}\,|\alpha(t)\rangle = \hat{\mathrm{h}}_{\mathrm{KS}}(t)\,|\alpha(t)\rangle\,. \tag{E.2}$$

The time evolution of the density matrix operator

$$\hat{\rho}(t) = \sum_{\alpha}^{\mathrm{occ}} |\alpha(t)\rangle\langle\alpha(t)| \tag{E.3}$$

is given by the Liouville-von-Neumann equation

$$\mathrm{i}\frac{\mathrm{d}}{\mathrm{d}t}\hat{\rho(\mathrm{t})} = \left[\hat{\mathrm{h}}_{\mathrm{KS}}(t), \hat{\rho}(t)\right]. \tag{E.4}$$

Splitting also the density matrix operator into a unperturbed and a perturbed part

$$\hat{\rho}(t) = \hat{\rho}^{(0)} + \hat{\rho}^{(1)}(t) \tag{E.5}$$

allows for a linearization of (E.4) by omitting the commutator $\left[\delta V_{\mathrm{eff}}(t), \hat{\rho}^{(1)}(t)\right]$

$$\mathrm{i}\frac{\mathrm{d}}{\mathrm{d}t}\hat{\rho}^{(1)}(t) = \left[\hat{\mathrm{h}}^{(0)}_{\mathrm{KS}}, \hat{\rho}^{(1)}(t)\right] + \left[\delta V_{\mathrm{eff}}(t), \hat{\rho}^{(0)}(t)\right]. \tag{E.6}$$

Taking the matrix element of (E.6) between two eigenstates $\langle m|$ and $|n\rangle$ of the unperturbed system yields

$$\mathrm{i}\frac{\mathrm{d}}{\mathrm{d}t}\rho^{(1)}_{mn}(t) = (\varepsilon_m - \varepsilon_n)\rho^{(1)}_{mn}(t) + (f_n - f_m)\delta V_{\mathrm{eff},mn}(t). \tag{E.7}$$

Inserting the Fourier transforms of the total perturbing potential and the density matrix variation

$$\delta V_{\mathrm{eff},mn}(t) = \int \frac{\mathrm{d}\omega}{2\pi} \delta V_{\mathrm{eff},mn}(\omega) \mathrm{e}^{-\mathrm{i}(\omega+\mathrm{i}\eta)t} \tag{E.8a}$$

$$\rho^{(1)}_{mn}(t) = \int \frac{\mathrm{d}\omega}{2\pi} \rho^{(1)}_{mn}(\omega) \mathrm{e}^{-\mathrm{i}(\omega+\mathrm{i}\eta)t} \tag{E.8b}$$

results in

$$\rho^{(1)}_{mn}(\omega) = \frac{f_m - f_n}{\varepsilon_n - \varepsilon_m - \omega - \mathrm{i}\eta} \delta V_{\mathrm{eff},mn}(\omega), \tag{E.9}$$

where the $\eta > 0$ factor accounts for the adiabatically switching on of the perturbation in the past. Now, a new response function $R(\boldsymbol{r}, \boldsymbol{r}', t)$ can be introduced that relates the induced charge density linearly with the total effective perturbing potential (the factor of 2 accounts for the assumed spin degeneracy)

$$n_{\mathrm{ind}}(\boldsymbol{r}, \omega) = 2\rho^{(1)}(\boldsymbol{r}, \boldsymbol{r}, \omega) \equiv \int R(\boldsymbol{r}, \boldsymbol{r}', \omega) \delta V_{\mathrm{eff}}(\boldsymbol{r}', \omega) \, \mathrm{d}^3 r' \, . \tag{E.10}$$

This response function is directly found using (E.9),

$$\rho^{(1)}(\boldsymbol{r}, \boldsymbol{r}, \omega) = \sum_{m,n} \phi_m(\boldsymbol{r}) \rho^{(1)}_{mn}(\omega) \phi^*_n(\boldsymbol{r}) \tag{E.11}$$

and

$$\delta V_{\mathrm{eff},mn}(\omega) = \int \phi^*_m(\boldsymbol{r}) \delta V_{\mathrm{eff}}(\boldsymbol{r}, \omega) \phi_n(\boldsymbol{r}) \, \mathrm{d}^3 r \tag{E.12}$$

to be

$$R(\boldsymbol{r}, \boldsymbol{r}', \omega) = 2 \sum_{m,n} \frac{f_n - f_m}{\varepsilon_n - \varepsilon_m + \omega + \mathrm{i}\eta} \phi^*_n(\boldsymbol{r}) \phi_m(\boldsymbol{r}) \left(\phi^*_n(\boldsymbol{r}') \phi_m(\boldsymbol{r}') \right)^* . \tag{E.13}$$

In order to relate the response R to the dielectric function (2.12) we express it in terms of the response functions used in (2.16). For the susceptibility we find

$$\chi = \frac{\delta n^{\mathrm{ind}}}{\delta V^{\mathrm{ext}}} = \frac{\delta n^{\mathrm{ind}}}{\delta V^{\mathrm{eff}}} \left(1 + \frac{\delta V_{\mathrm{H}}}{\delta n^{\mathrm{ind}}} \frac{\delta n^{\mathrm{ind}}}{\delta V_{\mathrm{ext}}} + \frac{\delta V_{\mathrm{xc}}}{\delta n^{\mathrm{ind}}} \frac{\delta n^{\mathrm{ind}}}{\delta V_{\mathrm{ext}}} \right) = R + R(v + f_{\mathrm{xc}})\chi, \tag{E.14}$$

where

$$f_{\mathrm{xc}}(\boldsymbol{r}, t; \boldsymbol{r}', t') \coloneqq \frac{\delta V_{\mathrm{xc}}(\boldsymbol{r}, t)}{\delta n^{\mathrm{ind}}(\boldsymbol{r}', t')} \tag{E.15}$$

is the *exchange-correlation kernel*. A similar procedure relates R to the polarizability P according to

$$P = R + R f_{\mathrm{xc}} P. \tag{E.16}$$

Neglecting the exchange-correlation effects, i.e. setting $f_{\mathrm{xc}} = 0$ yields P and χ in the so called *Random-Phase-approximation* (RPA).

E.2. Dielectic matrix in RPA

In the RPA we neglect f_{xc} in eq. (E.16), so that $P^0 = R$ and write for the lattice Fourier transform of ε^0:

$$\varepsilon^0_{\boldsymbol{G}\boldsymbol{G}'}(\boldsymbol{q},\omega) = \delta_{\boldsymbol{G}\boldsymbol{G}'} - v_{\boldsymbol{G}}(\boldsymbol{q}) P^0_{\boldsymbol{G}\boldsymbol{G}'}(\boldsymbol{q},\omega), \tag{E.17}$$

where the lattice Fourier transform of P^0 can be expressed using the plane wave matrix elements eq. (4.30) as

$$\begin{aligned} P^0_{\boldsymbol{G}\boldsymbol{G}'}(\boldsymbol{q},\omega) = \frac{1}{V}\sum_{o u \boldsymbol{k}} \big(& w_{o u \boldsymbol{k}}(\boldsymbol{q},\omega) M_{o u \boldsymbol{k}}(\boldsymbol{G},\boldsymbol{q}) M^*_{o u \boldsymbol{k}}(\boldsymbol{G}',\boldsymbol{q}) \\ & + w_{u o \boldsymbol{k}}(\boldsymbol{q},\omega) M_{u o \boldsymbol{k}}(\boldsymbol{G},\boldsymbol{q}) M^*_{u o \boldsymbol{k}}(\boldsymbol{G}',\boldsymbol{q}) \big) \\ =: P^{0,\mathrm{R}}_{\boldsymbol{G}\boldsymbol{G}'}(\boldsymbol{q},\omega) & + P^{0,\mathrm{AR}}_{\boldsymbol{G}\boldsymbol{G}'}(\boldsymbol{q},\omega), \end{aligned} \tag{E.18}$$

where o (u) denotes occupied (unoccupied) states. The resonant and anti-resonant weights are defined as

$$w_{o u \boldsymbol{k}}(\boldsymbol{q},\omega) = \frac{f_{o\boldsymbol{k}} - f_{u\boldsymbol{k}+\boldsymbol{q}}}{\omega - \left(\varepsilon_{u\boldsymbol{k}+\boldsymbol{q}} - \varepsilon_{o\boldsymbol{k}}\right) + \mathrm{i}\delta} \quad w_{u o \boldsymbol{k}}(\boldsymbol{q},\omega) = \frac{f_{o\boldsymbol{k}+\boldsymbol{q}} - f_{u\boldsymbol{k}}}{-\omega - \left(\varepsilon_{u\boldsymbol{k}} - \varepsilon_{o\boldsymbol{k}+\boldsymbol{q}}\right) - \mathrm{i}\delta}. \tag{E.19}$$

The resonant and anti-resonant contributions are related by the symmetry properties of the plane-wave matrix elements as

$$P^{0,\mathrm{AR}}_{\boldsymbol{G}\boldsymbol{G}'}(\boldsymbol{q},\omega) = P^{0,\mathrm{R}*}_{-\boldsymbol{G}-\boldsymbol{G}'}(-\boldsymbol{q},-\omega). \tag{E.20}$$

Employing the time reversal symmetry yields another relation, namely

$$P^{0,\mathrm{AR}}_{\boldsymbol{G}\boldsymbol{G}'}(\boldsymbol{q},\omega) = P^{0,\mathrm{R}*}_{\boldsymbol{G}'\boldsymbol{G}}(\boldsymbol{q},-\omega). \tag{E.21}$$

Comparing eq. (E.13) and eq. (4.3) and neglecting the different time-ordering, one finds

$$\chi_0(\boldsymbol{r},\boldsymbol{r}',\boldsymbol{r},\boldsymbol{r}',\omega) = P^0(\boldsymbol{r},\boldsymbol{r}',-\omega) \tag{E.22}$$

if the quasi-particle wave-functions are replaced with the Kohn-Sham orbitals. The differing sign in the frequency stems from the choice to do the Fourier transform of the BSE eq. (3.24) in $t_2 - t_1$ instead of $t_1 - t_2$ in order to comply with [3].

We are interested in the case of static screening, i.e. $\omega = 0$, and we construct ε^0 without broadening, i.e. $\delta = 0$. In this case, it is

$$P^{0,\mathrm{AR}}_{\boldsymbol{G}\boldsymbol{G}'}(\boldsymbol{q},0) \overset{\text{t.r.}}{=} P^{0,\mathrm{R}*}_{\boldsymbol{G}'\boldsymbol{G}}(\boldsymbol{q},0) \overset{\delta=0}{=} P^{0,\mathrm{R}}_{\boldsymbol{G}\boldsymbol{G}'}(\boldsymbol{q},0). \tag{E.23}$$

from which follows that eq. (E.18) reduces to

$$P^0_{\boldsymbol{G}\boldsymbol{G}'}(\boldsymbol{q},0) = 2P^{0,\mathrm{R}}_{\boldsymbol{G}\boldsymbol{G}'}(\boldsymbol{q},0). \tag{E.24}$$

F. Fourier Transform of L_0

In the construction of the matrix form of the Bethe-Salpeter equation the Fourier transform of the independent part L_0 of the two-particle correlation function L from the time to the frequency domain is needed. Since only electron-hole propagation is considered, L_0 only depends on one time difference $t = t_2 - t_1$, see section 3.3.4.

With the the definition of L_0 eq. (3.25) it is

$$L_0(\boldsymbol{r}_1, \boldsymbol{r}_2, \boldsymbol{r}_1', \boldsymbol{r}_2', t) = G_1(\boldsymbol{r}_1, \boldsymbol{r}_2', -t) G_1(\boldsymbol{r}_2, \boldsymbol{r}_1', t) \tag{F.1}$$

and using the independent quasiparticle approximation of G_1 eq. (3.20) we can write

$$\begin{aligned} L_0(\boldsymbol{r}_1, \boldsymbol{r}_2, \boldsymbol{r}_1', \boldsymbol{r}_2', \omega) &= \int \mathrm{d}t \iint \frac{\mathrm{d}\omega'}{2\pi} \frac{\mathrm{d}\omega''}{2\pi} G_1(\boldsymbol{r}_1, \boldsymbol{r}_2', \omega') G_1(\boldsymbol{r}_2, \boldsymbol{r}_1', \omega'') \mathrm{e}^{\mathrm{i}(\omega + \omega' - \omega'')t} \\ &= \int \frac{\mathrm{d}\omega'}{2\pi} G_1(\boldsymbol{r}_1, \boldsymbol{r}_2', \omega') G_1(\boldsymbol{r}_2, \boldsymbol{r}_1', \omega' + \omega) \\ &= \sum_{k,l} \int \frac{\mathrm{d}\omega'}{2\pi} \frac{\psi_k(\boldsymbol{r}_1) \psi_k^*(\boldsymbol{r}_2') \psi_l(\boldsymbol{r}_2) \psi_l^*(\boldsymbol{r}_1')}{\left(\omega' - \varepsilon_k + \mathrm{i}\delta \operatorname{sgn}(\varepsilon_k - E_\mathrm{f})\right) \left(\omega' + \omega - \varepsilon_l + \mathrm{i}\delta \operatorname{sgn}(\varepsilon_l - E_\mathrm{f})\right)}. \end{aligned} \tag{F.2}$$

Closing the contour in the upper half in the complex plane, the integral (F.2) is non-zero only if $\varepsilon_k > E_\mathrm{f} \wedge \varepsilon_l < E_\mathrm{f}$ or $\varepsilon_k < E_\mathrm{f} \wedge \varepsilon_l > E_\mathrm{f}$ and we get

$$\begin{aligned} L_0(\boldsymbol{r}_1, \boldsymbol{r}_2, \boldsymbol{r}_1', \boldsymbol{r}_2', \omega) = \mathrm{i} \sum_{k,l} &\psi_k(\boldsymbol{r}_1) \psi_k^*(\boldsymbol{r}_2') \psi_l(\boldsymbol{r}_2) \psi_l^*(\boldsymbol{r}_1') \\ &\times \left[-\frac{\Theta(\varepsilon_k - E_\mathrm{f}) \Theta(E_\mathrm{f} - \varepsilon_l)}{\varepsilon_k - \varepsilon_l + \omega - \mathrm{i}\delta} + \frac{\Theta(E_\mathrm{f} - \varepsilon_k) \Theta(\varepsilon_l - E_\mathrm{f})}{\varepsilon_k - \varepsilon_l + \omega + \mathrm{i}\delta} \right]. \end{aligned} \tag{F.3}$$

For an insulator without partial occupations we find in terms of the occupied (o) and unoccupied (u) states

$$\begin{aligned} L_0(\boldsymbol{r}_1, \boldsymbol{r}_2, \boldsymbol{r}_1', \boldsymbol{r}_2', \omega) &= -\mathrm{i} \sum_{o,u} \frac{\psi_u(\boldsymbol{r}_1) \psi_u^*(\boldsymbol{r}_2') \psi_o(\boldsymbol{r}_2) \psi_o^*(\boldsymbol{r}_1')}{\varepsilon_u - \varepsilon_o + \omega - \mathrm{i}\delta} + \frac{\psi_o(\boldsymbol{r}_1) \psi_o^*(\boldsymbol{r}_2') \psi_u(\boldsymbol{r}_2) \psi_u^*(\boldsymbol{r}_1')}{\varepsilon_u - \varepsilon_o - \omega - \mathrm{i}\delta} \\ &= -\mathrm{i} \sum_{o,u} \frac{\psi_o(\boldsymbol{r}_1) \psi_u^*(\boldsymbol{r}_1') \psi_o^*(\boldsymbol{r}_2') \psi_u(\boldsymbol{r}_2)}{\varepsilon_u - \varepsilon_o - \omega - \mathrm{i}\delta} + \frac{\psi_u(\boldsymbol{r}_1) \psi_o^*(\boldsymbol{r}_1') \psi_u^*(\boldsymbol{r}_2') \psi_o(\boldsymbol{r}_2)}{\varepsilon_u - \varepsilon_o + \omega - \mathrm{i}\delta} \\ &= \mathrm{i} \sum_{o,u} \frac{\psi_o(\boldsymbol{r}_1) \psi_u^*(\boldsymbol{r}_1') \psi_o^*(\boldsymbol{r}_2') \psi_u(\boldsymbol{r}_2)}{\omega - (\varepsilon_u - \varepsilon_o) + \mathrm{i}\delta} + \frac{\psi_u(\boldsymbol{r}_1) \psi_o^*(\boldsymbol{r}_1') \psi_u^*(\boldsymbol{r}_2') \psi_o(\boldsymbol{r}_2)}{-\omega - (\varepsilon_u - \varepsilon_o) + \mathrm{i}\delta}. \end{aligned} \tag{F.4}$$

Alternativley we can write eq. (F.3) for the insulator case equivalently as

$$\begin{aligned} L_0(\boldsymbol{r}_1, \boldsymbol{r}_2, \boldsymbol{r}_1', \boldsymbol{r}_2', \omega) &= -\mathrm{i} \sum_{k,l} \psi_k(\boldsymbol{r}_1)\psi_l^*(\boldsymbol{r}_1')\psi_k^*(\boldsymbol{r}_2')\psi_l(\boldsymbol{r}_2) \frac{\left|f_k - f_l\right|}{\left|\varepsilon_k - \varepsilon_l\right| + \omega\,\mathrm{sgn}(\varepsilon_k - \varepsilon_l) - \mathrm{i}\delta} \\ &= \mathrm{i} \sum_{k,l} \psi_k(\boldsymbol{r}_1)\psi_l^*(\boldsymbol{r}_1')\psi_k^*(\boldsymbol{r}_2')\psi_l(\boldsymbol{r}_2) \frac{\left|f_k - f_l\right|}{\omega\,\mathrm{sgn}(\varepsilon_l - \varepsilon_k) - \left|\varepsilon_k - \varepsilon_l\right| + \mathrm{i}\delta} \end{aligned} \tag{F.5}$$

which can be used to treat partial occupancies in semiconductors. A factor of 2 can be introduced here to account for the spin degeneracy of the occupation factors.

G. Task input/output files

In table G.1 we list, for each BSE-task, the files that are needed as input and the generated output files, and give a short description their contents.

Table G.1.: Required input files and generated output files for each BSE-task.

Main BSE-tasks	
xsgeneigvec	
Generates the KS eigenvectors and eigenenergies for the reference k-grid $\{\boldsymbol{k}\}$ and the symmetrically shifted k-grids $\left\{\boldsymbol{k}_- = \boldsymbol{k} - \boldsymbol{q}_{\mathrm{mt}}/2\right\}$ and $\left\{\boldsymbol{k}_+ = \boldsymbol{k} + \boldsymbol{q}_{\mathrm{mt}}/2\right\}$ needed for the q-depended BSE setup.	
Input files	
`STATE.OUT`[b]	Density and Kohn-Sham potential of a previous ground state calculation.
Output files	
`EVECFV`[a,b]	First variational KS eigenvectors.
`EVECSV`[a,b]	Second variational KS eigenvectors. Contain the first variatonal one, if no spin was considered.
`EVALSV`[a,b]	Second (or first) variational KS eigenvalues.
`EIGVAL`[a,c]	Second (or first) variational KS eigenvalues.
`OCCSV`[a,b]	Second (or first) variational KS occupation numbers.
`EFERMI`[a,c]	Fermi energy.
`APWCMT`[a,b]	Combination of basis matching coefficients and eigenvector coefficients of the APW basis functions. Needed for the PWE generation.
`LOCMT`[a,b,d]	Combination of basis matching coefficients and eigenvector coefficients of the LO basis functions.
`BONDLENGTH`[a,c,e]	Bond lengths.
`QMTPOINTS.OUT`[c,e]	List of momentum transfer vectors $\boldsymbol{Q}_{\mathrm{mt}}$ specified in the `exciting` input.
`GQPOINTS`[a,c,e]	List of $\boldsymbol{G} + \boldsymbol{q}_{\mathrm{mt}}$ vectors for each specified $\boldsymbol{Q}_{\mathrm{mt}}$.
`KPOINTS`[a,c,e]	List of $\boldsymbol{k}$-vectors used.
`XSGRIDS/*`[c,e,f]	Folder containing detailed information about the k-grids generated by `mod_xsgrids`. Is produced when `xs%writexsgrids` is set to `true`.
continued	

Required input files and generated output files for each BSE-task.

INFO[a,c,e]	Information about the SCF procedure.
scrgeneigvec	
Generates the KS eigenvectors and eigenenergies for the reference k-grid $\{\boldsymbol{k}\}$ needed for the setup of the KS dielectric response in RPA. Uses (generally) different ground state parameter then xsgeneigvec, e.g. a higher number of considered empty states.	
Same as xsgeneigvec, but replace the superscript a with g	
writepmatxs	
Generates the momentum operator matrix elements from the KS solution generated in xsgeneigvec.	
Input files	
STATE.OUT[b]	Density and Kohn-Sham potential of a previous ground state calculation.
EVECFV[h,b]	First variational KS eigenvectors for the reference k-grid.
EVECSV[h,b]	Second variational KS eigenvectors for the reference k-grid.
Output files	
PMAT_XS.OUT[b]	Momentum operator matrix elements.
scrwritepmat	
Generates the momentum operator matrix elements from the KS solution generated in scrgeneigvec.	
Input files	
STATE.OUT[b]	Density and Kohn-Sham potential of a previous ground state calculation.
EVECFV[g,b]	First variational KS eigenvectors for the reference k-grid and screening input parameters.
EVECSV[g,b]	Second variational KS eigenvectors for the reference k-grid and screening input parameters.
Output files	
PMAT[g,b]	Momentum operator matrix elements.
screen	
Generates the lattice Fourier coefficients of the KS microscopic dielectric function (tensor) in the RPA. It uses the KS eigen-solutions generated from scrgeneigvec.	
Input files	
STATE.OUT[b]	Density and Kohn-Sham potential of a previous ground state calculation.
EVECFV[b,g]	First variational KS eigenvectors.

continued

Required input files and generated output files for each BSE-task.

EVECSV[b,g]	Second variational KS eigenvectors.
APWCMT[b,g]	Combination of basis matching coefficients and eigenvector coefficients of the APW basis functions.
EFERMI[c,g]	Fermi energy.
OCCSV[b,g]	Second (or first) variational KS occupation numbers.
PMAT[g]	Momentum operator matrix elements.
	Output files
DIELTENSO_NOSYM[g,c,e]	The KS microscopic dielectric tensor in the RPA before symmetrization w.r.t. the lattice symmetry.
DIELTENSO[g,c,e]	The lattice-symmetrized KS microscopic dielectric tensor in the RPA.
EPSO/EPSO[i,b]	Lattice Fourier components of the KS microscopic dielectric function $\varepsilon^0_{\boldsymbol{GG'}}(\boldsymbol{q})$.
SCREEN/SCREEN[i,c,e]	Lattice Fourier components of the KS microscopic dielectric function $\varepsilon^0_{\boldsymbol{GG'}}(\boldsymbol{q})$.
QPOINTS[g]	List of $\boldsymbol{q}$ vectors used.
GQPOINTS/GQPOINTS[i,c,e]	List of $\boldsymbol{G}+\boldsymbol{q}$ vectors used.
TIMINGS/*[c,d]	Various timing variables.
	exccoulint
Generates exchange interaction matrix elements needed for the BSE Hamiltonian.	
	Input files
STATE.OUT[b]	Density and Kohn-Sham potential of a previous ground state calculation.
EVECFV[a,b]	First variational KS eigenvectors.
EVECSV[a,b]	Second variational KS eigenvectors.
APWCMT[a,b]	Combination of basis matching coefficients and eigenvector coefficients of the APW basis functions.
EFERMI[a,c]	Fermi energy.
OCCSV[a,b]	Second (or first) variational KS occupation numbers.
	Output files
EXCLI[a,b]	The resonant-resonant part of the exchange interaction part of the BSE matrix.
BSEINFO_EXCLI[a,b]	Auxiliary info file used to store information about what is stored in EXCLI.

continued

Required input files and generated output files for each BSE-task.

scrcoulint	
Generates screened Coulomb interaction matrix elements needed for the BSE Hamiltonian.	
Input files	
STATE.OUT[b]	Density and Kohn-Sham potential of a previous ground state calculation.
EVECFV[a,b]	First variational KS eigenvectors.
EVECSV[a,b]	Second variational KS eigenvectors.
APWCMT[a,b]	Combination of basis matching coefficients and eigenvector coefficients of the APW basis functions.
EVALSV[a,b]	Second (or first) variational KS eigenvalues.
EFERMI[a,c]	Fermi energy.
OCCSV[a,b]	Second (or first) variational KS occupation numbers.
EPS0/EPS0[i,b]	Lattice Fourier components of the KS microscopic dielectric function $\varepsilon^0_{\boldsymbol{GG'}}(\boldsymbol{q})$.
Output files	
SCCLI[a,b]	The resonant-resonant part of the screened Coulomb interaction part of the BSE matrix.
SCCLIC[a,b]	The resonant-anti-resonant part of the screened Coulomb interaction part of the BSE matrix.
BSEINFO_SCCLI[a,b]	Auxiliary info file used to store information about what is stored in SCCLI.
BSEINFO_SCCLIC[a,b]	Auxiliary info file used to store information about what is stored in SCCLIC.
EMATRAD/EMATRAD[a,i,b,j]	Radial integrals used in the construction of the PWEs.
bse	
Sets up the BSE matrix and diagonalizes it. From the eigen-solution the dielectric function (tensor) and derived quantities are computed.	
Input files	
STATE.OUT[b]	Density and Kohn-Sham potential of a previous ground state calculation.
EVECFV[a,b]	First variational KS eigenvectors.
APWCMT[a,b]	Combination of basis matching coefficients and eigenvector coefficients of the APW basis functions.
EFERMI[a,c]	Fermi energy.
EVALSV[a,b]	Second (or first) variational KS eigenvalues.
OCCSV[a,b]	Second (or first) variational KS occupation numbers.
PMAT_XS.OUT[b]	Momentum operator matrix elements.

continued

Required input files and generated output files for each BSE-task.

EXCLI[a,b]	The resonant-resonant part of the exchange interaction part of the BSE matrix.
BSEINFO_EXCLI[a,b]	Auxiliary info file used to store information about what is stored in EXCLI.
SCCLI[a,b]	The resonant-resonant part of the screened Coulomb interaction part of the BSE matrix.
SCCLIC[a,b]	The resonant-anti-resonant part of the screened Coulomb interaction part of the BSE matrix.
BSEINFO_SCCLI[a,b]	Auxiliary info file used to store information about what is stored in SCCLI.
BSEINFO_SCCLIC[a,b]	Auxiliary info file used to store information about what is stored in SCCLIC.
	Output files
EXCITON/EXCITON[k,l,c]	The eigenvalues of the BSE matrix (exciton energies) E_λ and the transitions coefficients t_λ.
EPSILON/EPSILON[k,l,c]	The macroscopic dielectric tensor $\varepsilon^{ij}(\omega)$ or the (generalized) macroscopic dielectric function for finite momentum transfer $\varepsilon_{\mathrm{M}}(\boldsymbol{Q},\omega)$.
LOSS/LOSS[k,l,c]	The dynamical structure factor $S(\boldsymbol{Q},\omega)$ and the loss function $L(\boldsymbol{Q},\omega)$ for finite momentum transfer.
SIGMA/SIGMA[k,l,c,d]	The optical conductivity.
EXCCOEFF[k,l,b]	Exciton eigen-coefficients. Optional output, can be very large.
MEASURE/*[c,i]	Folder containing the coupling measures.
Pre- and post-processing BSE-tasks	
	bsesurvey
Based on the KS eigen-solution of xsgeneigvec, the task only creates the combined BSE-index and writes out information of the considered ip-transition. When the transitions are selected by energy, it is advisable to use this task to first check the size of the resulting BSE matrix.	
	Input files
STATE.OUT[b]	Density and Kohn-Sham potential of a previous ground state calculation.
EFERMI[h,c]	Fermi energy.
EVALSV[a,b]	Second (or first) variational KS eigenvalues.
OCCSV[a,b]	Second (or first) variational KS occupation numbers.
	Output files

continued

Required input files and generated output files for each BSE-task.

`BSESURVEY/*`[a,c]	Files containing information about the used ip-transitions and various index maps.
writebevec	
When the exciton eigenvectors are saved to file in `bse`, this task can be used to write out the eigen-coefficients to human-readable text files.	
Input files	
`EXCCOEFF`[k,l,b]	Exciton eigen-coefficients.
Output files	
`EXCITON_EVEC/*`[a,c,m]	Resonant (anti-resonant) exciton eigen-coefficients.
`BEVEC/*`[a,c,m]	Resonant (anti-resonant) exciton eigen-coefficients (old format).
`BEVEC_KSUM/*`[a,c,m]	Exciton coefficients summed over k-points for each band combination.
writekpathweights	
Interpolates the resonant (anti-resonant) conduction and valence excitonic weights linearly onto a previously calculated band structure k-path.	
Input files	
`bandstructure.dat`[c]	Band structure data generated by `exciting`'s property launcher.
`EXCCOEFF`[k,l,b]	Exciton eigen-coefficients.
Output files	
`KPATHEXC/KPATH`[a,c,m]	Band structure data with excitonic weights
`KPATHEXC/WEIGHTS`[a,c,m]	Excitonic weights on the k-grids used in the BSE (basis of the interpolation)
bsegenspec	
Reads the excitonic energies and the BSE transition coefficients from file and recalculates the dielectric function, loss function, dynamical structure factor and optical conductivity for the `energywindow` and `broadening` specified in the input file.	
Input files	
`STATE.OUT`[b]	Density and Kohn-Sham potential of a previous ground state calculation.
`EXCITON/EXCITON`[k,l,c]	The eigenvalues of the BSE matrix (exciton energies) E_λ and the transitions coefficients t_λ.
Output files	
`EPSILON/EPSILON`[k,l,c]	The macroscopic dielectric tensor $\varepsilon^{ij}(\omega)$ or the (generalized) macroscopic dielectric function for finite momentum transfer $\varepsilon_{\mathrm{M}}(\boldsymbol{Q},\omega)$.

continued

Required input files and generated output files for each BSE-task.

`LOSS/LOSS`[k,l,c]	The dynamical structure factor $S(\boldsymbol{Q},\omega)$ and the loss function $L(\boldsymbol{Q},\omega)$ for finite momentum transfer.
`SIGMA/SIGMA`[k,l,c,d]	The optical conductivity.

[a] File extension specifying the momentum transfer vector `_QMTxyz[_m].OUT`, where `xyz` stands for the $\boldsymbol{q}_{\mathrm{mt}}$-point index and the ending `_m` signals the whether the negative shift $-\boldsymbol{q}_{\mathrm{mt}}/2$ was used instead of the positive one.
[b] Binary file
[c] Human readable file
[d] Not used legacy output
[e] Info file, not needed as input
[f] Optional output
[g] File extension `_SCR.OUT`
[h] File extension `_QMT001.OUT`
[i] File extension `_Qxyz[_m].OUT` specifying the q-point associated to a k-point difference $\boldsymbol{q} = \boldsymbol{k}' - \boldsymbol{k}$ or to a k-point sum $\boldsymbol{q} = -\boldsymbol{k}' - \boldsymbol{k}$ (if `_m` is present).
[j] Can be deleted after task completion
[k] File extension specifying which type of BSE calculation was used `_BSE[_-singlet,-triplet,-ip][_-TDA]_SCR-full`.
[l] File extension specifying either which non-zero Q-point was used `_QMTxyz.OUT` or which optical component was calculated `_OCxy`.
[m] File extension contains the exciton index `LAMBDAxyz`.

H. Source files

In the following we list the most important source code files for the BSE part of `exciting`. In table H.1 the main files unique to each BSE-task are listed and described, whereas in table H.2 the main newly introduced support modules used in multiple BSE-tasks are described. A more detailed description can be found in the in-code documentation and the `excitingsubroutines.pdf` document that can be generated using the make system of `exciting`.

Table H.1.: Most important source code files associated with each BSE-task.

Main BSE-tasks	
	xsgeneigvec
`b_xsgeneigveclauncher.f90`	Wrapper routine for `b_xsgeneigvec`. Launches one-shot ground state calculations needed for q-dependent BSE.
`b_xsgeneigvec.f90`	Fork of `xsgeneigvec.f90`. Executes one-shot ground state using `writeevec.F90` for a list of passed k-grid offsets.
	scrgeneigvec
Same files as for `xsgeneigvec`	
	writepmatxs
`writepmatxs.F90`	Calculates the momentum operator matrix elements.
	scrwritepmat
`scrwritepmat.F90`	Wrapper for `writepmatxs.F90` to launch it with the `screening` parameters instead of the `xs` ones.
`writepmatxs.F90`	Calculates the momentum operator matrix elements.
	screen
`b_screenlauncher.f90`	Wrapper routine for `dfq.f90`. It starts the calculation of the KS dielectric matrix (in RPA) for the q-points $\vec{q} = \vec{k}' - \vec{k}$. If the BSE coupling blocks are included, it does the same for a shifted set of q-point $q = -\vec{k}' - \vec{k}$.
	continued

Most important source code files associated with each BSE-task.

`dfq.f90`	When called in this task, it calculates the KS dielectric matrix in RPA for a given q-point grid.
	exccoulint
`b_exccoulintlauncher.f90`	Wrapper routine for `b_exccoulint.f90` that starts the calculation of the exchange term of the Bethe-Salpeter Hamiltonian for the specified momentum transfer vectors $\vec{q}_{\mathrm{mt}}$.
`b_exccoulint.f90`	Calculates the exchange term of the Bethe-Salpeter Hamiltonian for a given momentum transfer.
	scrcoulint
`b_scrcoulintlauncher.f90`	Wrapper routine for `b_scrcoulint.f90` that starts the calculation of the rr- and ra-block of the screened Coulomb interaction term of the Bethe-Salpeter Hamiltonian for the specified momentum transfer vectors $\vec{q}_{\mathrm{mt}}$.
`b_scrcoulint.f90`	Calculates the screened Coulomb interaction term of the Bethe-Salpeter Hamiltonian for a given momentum transfer.
	bse
`b_bselauncher.f90`	Wrapper routine for `b_bse.f90` that starts the setup and diagonalization of the BSE Hamiltonian for each specified momentum transfer vectors $\vec{q}_{\mathrm{mt}}$.
`b_bse.f90`	Manages the setup and diagonalization of the BSE Hamiltonian for a given momentum transfer.
`m_setup_bse.f90`	Module handling the setup of the BSE Hamiltonian.
`m_makeoscistr.f90`	Module handling the generation of the transition coefficients from the eigen-solutions of the BSE.
`m_makespectrum.f90`	Module handling the generation of $\varepsilon_{\mathrm{M}}^{ij}(\omega)$ or $\varepsilon_{\mathrm{M}}(\boldsymbol{Q},\omega)$ from the BSE eigen-energies and the transition coefficients.
`m_writeoscillator.f90`	Module handling the write out of the BSE eigen-energies and the transition coefficients.
`writederived.f90`	Writes out the dielectric function, the loss function and the dynamical structure factor.
Pre- and post-processing BSE-tasks	
	bsesurvey
	continued

Most important source code files associated with each BSE-task.

`b_bsesurvey.f90`	Calls `setranges_modxs` and `select_transitions` to construct the combined BSE-index. Writes relevant index maps to text files.
	writebevec
`b_writeexcvec.f90`	Reads the binary BSE output and writes the excitonic eigen-coefficients to text files.
	writekpathweights
`b_writekpathweights.f90`	Uses excitonic eigen-coefficients to generate the excitonic weights. The weights are then interpolated onto a band structure k-path.
	bsegenspec
`b_bsegenspec.f90`	Reads the exciton energies and the BSE transition coefficients and recalculates the BSE spectra.

Table H.2.: New support modules and their main routines.

mod_xsgrids.f90	
Module for the generation and storage of the different k-grids needed for the q-dependent BSE. The module is used by the tasks `xsgeneigvec`, `scrgeneigvec`, `screen`, `scrcoulint`, `exccoulint` and `bse`.	
`xsgrids_init`	Given a momentum transfer vector $\boldsymbol{Q}_{\mathrm{mt}} = \boldsymbol{G}_{\mathrm{mt}} + \boldsymbol{q}_{\mathrm{mt}}$, the routine sets up the associated k-grids $\{\boldsymbol{k}\}$, $\{\boldsymbol{k}_+ = \boldsymbol{k} + \boldsymbol{q}_{\mathrm{mt}}/2\}$ and $\{\boldsymbol{k}_- = \boldsymbol{k} - \boldsymbol{q}_{\mathrm{mt}}/2\}$. Additionally, the q-grids formed from $\{\boldsymbol{q} = \boldsymbol{k}' - \boldsymbol{k}\}$ and $\{\boldsymbol{q} = -\boldsymbol{k}'_+ - \boldsymbol{k}_-\}$ are set up. Various index maps are created relating the points of the different grids. If requested also the corresponding $\boldsymbol{G} + \boldsymbol{k}$ and $\boldsymbol{G} + \boldsymbol{q}$ are created.
`xsgrids_finalize`	Clears all module variables.
`xsgrids_write_grids`	Writes information about the grids to the folder `XSGRIDS`.
modbse.f90	
The module is used by the tasks `exccoulint`, `scrcoulint` and `bse` and contains shared variables and routines handling the storage and setup of the combined BSE index $\alpha \in \{u, o, \boldsymbol{k}\}$.	
`setranges_modxs`	Wrapper routine for `findocclims`. Used to initialize `modxs` module variables for occupation limits based on the k-grid $\boldsymbol{k}$, $\boldsymbol{k} + \boldsymbol{q}/2$ and $\boldsymbol{k} - \boldsymbol{q}/2$.
`select_transitions`	The routine creates the combined index map α. It support two types of selection methods: (a) IP transitions in a specified energy range are considered. (b) All IP transitions between a set of bands are considered. In both methods the occupation difference of each transition is inspected and only those with positive $f_{o_\alpha \boldsymbol{k}_\alpha} - f_{u_\alpha \boldsymbol{k}'_\alpha}$ are kept to guarantee the hermiticity of the Hamiltonian.
`hamidx, hamidx_back, subhamidx, subhamidx_back`	Helper functions to map between combined and individual indices.
modmpi.f90	
Preexisting general purpose module to simplify the use of `MPI` in `exciting` . Extensions were made to allow for the use of multiple `MPI` communicators. See `excitingsubroutines.pfd` and the in-code documentation.	
modscl.f90	
continued	

New support modules and their main routines.

General purpose module to simplify the use of ScaLapack in exciting . It contains helper types and routines to: (a) setup BLACS process grids needed by ScaLapack and (b) to easily handle distributed complex matrices. The module is used by the task bse.	
setupblacs	Creates a BLACS process grid of dimension 2, 1 or 0 on top of a MPI-communicator.
blacsbarrier	Wrapper for blacs_barrier.
exitblacs	Wrapper for blacs_gridexit.
new_dzmat	Initializes a block cyclic distributed global matrix for a given BLACS process grid. It sets up descriptor arrays, builds index maps and allocates the local matrix. In the case of compilation without ScaLAPACK the global matrix is identical to the local matrix.
del_dzmat	Deallocates a distributed complex matrix.
dzmat_send2global_root, dzmat_send2global_all, dzmat_copy_global2local, dzmat_copy	Routines for collecting (distributing) a distributed matrix. dzmat_copy is the most general version that allows for inter-context copying.
Modules containing auxilliary routines for handling distributed matrices	
m_dzmatmult.f90	Wrapper routines for easy use of Lapack or ScaLapack for matrix-matrix multiplication of a (optionally) distributed complex matrix.
m_dhesolver.f90	Wrapper routines for easy use of Lapack or ScaLapack to diagonalize a (optionally) distributed hermitian matrix.
m_invertzmat.f90	Wrapper routines for easy use of Lapack or ScaLapack to invert a (optionally) distributed hermitian positive definite matrix.

I. Exciting input

In table I.1 we list and describe the new input elements for the exciting xml input file input.xml. Except for the new xml-*element* xs%writekpathweights, only new xml-*attributes* were added to existing elements.

Table I.1.: Changes to the exciting input.

Element	*Attribute*	*Values [Default]*	*Description*
xs	writexsgrids	true, [false]	Write out detailed information about the used k-grids.
xs%BSE	beyond	true, [false]	Set to true to enable the extended BSE code described in this work.
	coupling	true, [false]	Set to true to disable the TDA.
	blocks	rr, ra, [both]	Calculate resonant-resonant, resonant-anti-resonant or both blocks of the BSE matrix.
	measure	true, [false]	Write out coupling measures.
	checkposdef	true, [false]	Explicitly check positive definiteness of BSE matrices before inversion (generally not needed).
	intraband	[true], false	In the construction of the RPA dielectric function, consider also transitions within one band for finite momentum transfer.
	distribute	true, [false]	Use distributed matrices and the ScaLapack eigensolver.
	eecs	integer [3]	May be increased if the ScaLapack eigensolver is used (generally not necessary).
	efind	true, [false]	Only search for BSE eigen-solution that fall into the requested energywindow.

continued

Changes to the `exciting` input.

Element	*Attribute*	*Values [Default]*	*Description*
	econv	doublepair [0.0 0.0]	Alternative to `nstlbse`, triggers the transition selection according to the requested `energywindow`. The energy window w is modified with the specified convergence energy $[\omega(1) + \text{econf}(1), \omega(2) + \text{econf}(2)]$.
	cuttype	1d, 2d [none]	Type of the truncation of the Coulomb potential (Still in development).
	iqmtrange	integerpair [1 1]	Specifies for which momentum transfer vectors listed in `xs%qpointlist` the BSE is to be solved.
xs%screening	tr	[true], false	Use time-reversal symmetry and avoid the explicit calculation of the anti-resonant part of the RPA KS dielectric response.
xs%storeexcitons	selectenergy	true, [false]	Select BSE eigenvectors to store by energy instead of index.
	useev	[true], false	Specified energy is in eV/Hartree.
	MinEnergyExcitons	double [0.0]	Lower bound of energy interval.
	MaxEnergyExcitons	double [100.0]	Upper bound of energy interval.
xs%writeexcitons	selectenergy	true, [false]	Select BSE eigenvectors to store by energy instead of index.
	useev	[true], false	Specified energy is in eV/Hartree.
	abscutres	doublepair [0.0 1d10]	Write out resonant exciton eigencoefficients of a modulus within this range.
	abscutares	doublepair [0.0 1d10]	Write out anti-resonant exciton eigencoefficients of a modulus within this range.
	MinEnergyExcitons	double [0.0]	Lower bound of energy interval.
	MaxEnergyExcitons	double [100.0]	Upper bound of energy interval.
xs%writekpathweights	selectenergy	true, [false]	Select BSE eigenvectors to store by energy instead of index.
	useev	[true], false	Specified energy is in eV/Hartree.

continued

Changes to the `exciting` input.

Element	*Attribute*	*Values [Default]*	*Description*
	printgridweights	[true], false	Write out the excitonic weights on which the interpolation is based upon.
	intorder	integer [2]	Spline order for the interpolation.
	MinEnergyExcitons	double [0.0]	Lower bound of energy interval.
	MaxEnergyExcitons	double [100.0]	Upper bound of energy interval.
	MinNumberExcitons	integer [1]	Lower bound of index interval.
	MaxNumberExcitons	integer [10]	Upper bound of index interval.

[a] All elements are children of `input`.
[b] The listed attributes are only available if `xs%BSE%beyond` is true.

Bibliography

1. Frenkel, J. On the Transformation of light into Heat in Solids. I. *Physical Review* **37,** 17–44 (Jan. 1931).
2. Wannier, G. H. The Structure of Electronic Excitation Levels in Insulating Crystals. *Physical Review* **52,** 191–197 (Aug. 1937).
3. Strinati, G. Application of the Green's functions method to the study of the optical properties of semiconductors. *La Rivista del Nuovo Cimento* **11,** 1–86 (Dec. 1988).
4. Hanke, W. & Sham, L. J. Many-Particle Effects in the Optical Excitations of a Semiconductor. *Physical Review Letters* **43,** 387–390 (July 1979).
5. Onida, G., Reining, L. & Rubio, A. Electronic excitations: density-functional versus many-body Green's-function approaches. *Reviews of Modern Physics* **74,** 601–659 (June 2002).
6. Olevano, V. & Reining, L. Excitonic Effects on the Silicon Plasmon Resonance. *Physical Review Letters* **86,** 5962–5965 (June 2001).
7. Grüning, M., Marini, A. & Gonze, X. Exciton-Plasmon States in Nanoscale Materials: Breakdown of the Tamm-Dancoff Approximation. *Nano Letters* **9,** 2820–2824 (Aug. 2009).
8. Gatti, M. & Sottile, F. Exciton dispersion from first principles. *Physical Review B* **88.** doi:10.1103/physrevb.88.155113 (Oct. 2013).
9. Sander, T., Maggio, E. & Kresse, G. Beyond the Tamm-Dancoff approximation for extended systems using exact diagonalization. *Physical Review B* **92.** doi:10.1103/physrevb.92.045209 (July 2015).
10. Gulans, A. *et al.* exciting: a full-potential all-electron package implementing density-functional theory and many-body perturbation theory. *Journal of Physics: Condensed Matter* **26,** 363202 (Aug. 2014).
11. Hambach, R. *Theory and ab-initio calculations of collective excitations in nanostructures: towards spatially-resolved EELS* Theses (Ecole Polytechnique X, Nov. 2010).
12. Hedin, L. & Lundqvist, S. in *Solid State Physics* (eds Seitz, F., Turnbull, D. & Ehrenreich, H.) (Elsevier Science, 1969). ISBN: 9780080864877.
13. Ambegaokar, V. & Kohn, W. Electromagnetic Properties of Insulators. I. *Physical Review* **117,** 423–431 (Jan. 1960).
14. Sole, R. D. & Fiorino, E. Macroscopic dielectric tensor at crystal surfaces. *Physical Review B* **29,** 4631–4645 (Apr. 1984).

15. Fetter, A. L. & Walecka, J. D. *Quantum Theory of Many-Particle Systems* 640 pp. ISBN: 0486428273 (Dover Publications Inc., 2003).

16. Adler, S. L. Quantum Theory of the Dielectric Constant in Real Solids. *Physical Review* **126,** 413–420 (Apr. 1962).

17. Wiser, N. Dielectric Constant with Local Field Effects Included. *Physical Review* **129,** 62–69 (Jan. 1963).

18. Grosso, G. & Parravicini, G. P. *Solid State Physics* ISBN: 0-12-304460-X (Academic Press, 2000).

19. Pusching, P. *Excitonic Effects in Organic Semi-conductors* (2002).

20. Sagmeister, S. *Excitonic Effects in Solids* (2009).

21. Thomas, L. H. The calculation of atomic fields. *Mathematical Proceedings of the Cambridge Philosophical Society* **23,** 542 (Jan. 1927).

22. Fermi, E. Eine statistische Methode zur Bestimmung einiger Eigenschaften des Atoms und ihre Anwendung auf die Theorie des periodischen Systems der Elemente. *Zeitschrift für Physik* **48,** 73–79 (Jan. 1928).

23. Hohenberg, P. & Kohn, W. Inhomogeneous Electron Gas. *Physical Review* **136,** B864–B871 (Nov. 1964).

24. Kohn, W. & Sham, L. J. Self-Consistent Equations Including Exchange and Correlation Effects. 1. *Physical Review* **140,** A1133–A1138 (Nov. 1965).

25. Roedl, C. *Elektronische und excitonische Anregungen in magnetischen Isolatoren* (2009).

26. Schwinger, J. The Theory of Quantized Fields. I. *Physical Review* **82,** 914–927 (June 1951).

27. Baym, G. & Kadanoff, L. P. Conservation Laws and Correlation Functions. *Physical Review* **124,** 287–299 (Oct. 1961).

28. Baym, G. Self-Consistent Approximations in Many-Body Systems. *Physical Review* **127,** 1391–1401 (Aug. 1962).

29. Hedin, L. New Method for Calculating the One-Particle Green's Function with Application to the Electron-Gas Problem. *Physical Review* **139,** A796–A823 (Aug. 1965).

30. Hybertsen, M. S. & Louie, S. G. First-Principles Theory of Quasiparticles: Calculation of Band Gaps in Semiconductors and Insulators. *Physical Review Letters* **55,** 1418–1421 (Sept. 1985).

31. Hybertsen, M. S. & Louie, S. G. Electron correlation in semiconductors and insulators: Band gaps and quasiparticle energies. *Physical Review B* **34,** 5390–5413 (Oct. 1986).

32. Strinati, G. Dynamical Shift and Broadening of Core Excitons in Semiconductors. *Physical Review Letters* **49,** 1519–1522 (Nov. 1982).

33. Mattuck, R. D. *A Guide to Feynman Diagrams in the Many-Body Problem* 429 pp. ISBN: 0486670473 (Dover Publications Inc., Nov. 1, 1992).

34. Furche, F. On the density matrix based approach to time-dependent density functional response theory. *The Journal of Chemical Physics* **114,** 5982–5992 (Apr. 2001).

35. Rosenfeld, L. *Theory of Electrons* 68 ff (New York: Dover Publications, 1965).

36. Runge, E. & Gross, E. K. U. Density-Functional Theory for Time-Dependent Systems. *Physical Review Letters* **52,** 997–1000 (Mar. 1984).

37. Anderson, E. *et al. LAPACK Users' Guide (Software, Environments and Tools)* ISBN: 0-89871-447-8 (Society for Industrial and Applied Mathematics, 1987).

38. Blackford, L. S. *et al. ScaLAPACK Users' Guide (Software, Environments and Tools)* ISBN: 0-89871-397-8 (Society for Industrial and Applied Mathematics, 1987).

39. Dongarra, J. & Whaley, R. C. *A User's Guid to the BLACS v1.1. Technical Report UT-CS-95-281. LAPACK Working Note 94.* tech. rep. (1997).

40. Williams, J. *BSPLINE-FORTRAN – Multidimensional B-Spline Interpolation of Data on a Regular Grid* <http://jacobwilliams.github.io/bspline-fortran/>.

41. Puschnig, P., Meisenbichler, C. & Draxl, C. Excited State Properties of Organic Semiconductors: Breakdown of the Tamm-Dancoff Approximation.

42. Tran, F. & Blaha, P. Accurate Band Gaps of Semiconductors and Insulators with a Semilocal Exchange-Correlation Potential. *Physical Review Letters* **102.** doi:10.1103/physrevlett.102.226401 (June 2009).

43. Stiebling, J. Optische Eigenschaften des einkristallinen Siliziums aus Elektronenenergieverlustmessungen. *Zeitschrift für Physik B Condensed Matter and Quanta* **31,** 355–357 (Dec. 1978).

44. Weissker, H.-C. *et al.* Dynamic structure factor and dielectric function of silicon for finite momentum transfer: Inelastic x-ray scattering experiments andab initiocalculations. *Physical Review B* **81.** doi:10.1103/physrevb.81.085104 (Feb. 2010).

45. Abbamonte, P. *et al.* Dynamical reconstruction of the exciton in LiF with inelastic x-ray scattering. *Proceedings of the National Academy of Sciences* **105,** 12159–12163 (Aug. 2008).

46. Perdew, J. P. & Wang, Y. Accurate and simple analytic representation of the electron-gas correlation energy. *Physical Review B* **45,** 13244–13249 (June 1992).

47. Hellenbrandt, M. The Inorganic Crystal Structure Database (ICSD)—Present and Future. *Crystallography Reviews* **10,** 17–22 (Jan. 2004).

48. Többens, D., Stüßer, N., Knorr, K., Mayer, H. & Lampert, G. E9: The New High-Resolution Neutron Powder Diffractometer at the Berlin Neutron Scattering Center. *Materials Science Forum* **378-381,** 288–293 (2001).

49. Ott, H. Die Strukturen von Mn O, Mn S, Ag F, Ni S, Sn I4, Sr Cl2, Ba F2, Praezisionsmessungen einiger Alkalihalogenide. *Zeitschrift für Kristallographie, Kristallgeometrie, Kristallphysik, Kristallchemie,* 222–230 (63 1926).

50. Blaha, P., Schwarz, K., Madsen, G., Kvasnicka, D. & Luitz, J. *WIEN2k, An Augmented Plane Wave + Local Orbitals Program for Calculating Crystal Properties* (Karlheinz Schwarz, Techn. Universität Wien, Austria, 2001). ISBN: 3-9501031-1-2.

51. Merkys, A. *et al.* COD::CIF::Parser: an error-correcting CIF parser for the Perl language. *Journal of Applied Crystallography* **49,** 292–301 (Feb. 2016).

52. Gražulis, S., Merkys, A., Vaitkus, A. & Okulič-Kazarinas, M. Computing stoichiometric molecular composition from crystal structures. *Journal of Applied Crystallography* **48,** 85–91 (Jan. 2015).

53. Gražulis, S. *et al.* Crystallography Open Database (COD): an open-access collection of crystal structures and platform for world-wide collaboration. *Nucleic Acids Research* **40,** D420–D427 (Nov. 2011).

54. Gražulis, S. *et al.* Crystallography Open Database – an open-access collection of crystal structures. *Journal of Applied Crystallography* **42,** 726–729 (Mar. 2009).

55. American mineralogist crystal structure database. *Choice Reviews Online* **41,** 41Sup–0262–41Sup–0262 (Aug. 2004).

56. Hoser, A. A. & Madsen, A. Ø. Dynamic quantum crystallography: lattice-dynamical models refined against diffraction data. II. Applications toL-alanine, naphthalene and xylitol. *Acta Crystallographica Section A Foundations and Advances* **73,** 102–114 (Jan. 2017).

57. Pelletier, M. & Brisse, F. Bithiophene at 133 K. *Acta Crystallographica Section C Crystal Structure Communications* **50,** 1942–1945 (Dec. 1994).

58. Puschnig, P. *et al.* Electronic, optical, and structural properties of oligophenylene molecular crystals under high pressure: Anab initioinvestigation. *Physical Review B* **67.** doi:10.1103/physrevb.67.235321 (June 2003).

59. Ong, S. P. *et al.* Python Materials Genomics (pymatgen): A robust, open-source python library for materials analysis. *Computational Materials Science* **68,** 314–319 (Feb. 2013).

60. Setyawan, W. & Curtarolo, S. High-throughput electronic band structure calculations: Challenges and tools. *Computational Materials Science* **49,** 299–312 (Aug. 2010).

61. Neil W. Ashcroft, N. M. *Solid State Physics* 848 pp. ISBN: 0030839939 (Cengage Learning, Inc, 1976).

62. Schwabl, F. *Quantenmechanik für Fortgeschrittene (QM II)* 432 pp. ISBN: 3540850759 (Springer, 2008).

63. Koelling, D. D. & Harmon, B. N. A technique for relativistic spin-polarised calculations. *Journal of Physics C: Solid State Physics* **10,** 3107–3114 (Aug. 1977).

64. Ehrenreich, H. & Cohen, M. H. Self-Consistent Field Approach to the Many-Electron Problem. *Physical Review* **115,** 786–790 (Aug. 1959).

Selbstständigkeitserklärung

Ich erkläre hiermit, dass ich die vorliegende Arbeit selbstständig verfasst und noch nicht für andere Prüfungen eingereicht habe. Sämtliche Quellen einschließlich Internetquellen, die unverändert oder abgewandelt wiedergegeben werden, insbesondere Quellen für Texte, Grafiken, Tabellen und Bilder, sind als solche kenntlich gemacht. Mir ist bekannt, dass bei Verstößen gegen diese Grundsätze ein Verfahren wegen Täuschungsversuchs bzw. Täuschung eingeleitet wird.

Berlin, 10. September 2017

Benjamin Aurich